eman ta zabal zazu

Universidad del País Vasco
Euskal Herriko Unibertsitatea

Spin-phonon interaction on magnetic adatoms

A thesis submitted to the
University of the Basque Country UPV/EHU
to obtain the degree of Doctor in Physics by

Haritz Garai Marin

Supervised by
Dr. Asier Eiguren Goienetxea
and
Dr. Julen Ibañez Azpiroz

December 2022

Contents

Introduction

An increasingly technological society has motivated fundamental research in the chase of shrinking the actual data storing and processing technology. This quest has achieved the nanometric scale during the last decades due to the advances of fabrication techniques. However, due to the physical limits of the current technology, the scaling predicted by Moore's law has been slowed down in recent years. Meanwhile, the crucial role of scientific research is being the study of alternatives, different from the currently established semiconductor technology, which are believed to offer a new paradigm in the field of data processing. In this context, atomic scale structures represent the smallest unit of matter for storing and processing information. However, while promising technologies such as quantum computing rely on the principles of quantum mechanics, the emergence of quantum phenomena represents a big challenge towards the control and manipulation of atomic scale structures.

Atomic size structures such as atomic clusters and chains, or even single magnetic adatoms are promising candidates for making data storage devices and quantum bits due to their long living magnetic quantum states [1–12]. In this aspect, magnetic adatoms offer an exceptional scenario to explore many interesting phenomena such as magnetic excitations [13–16], magnetic interactions [17–19] or spin relaxation and decoherence [6, 8, 12]. In this line, outstanding progress has been achieved thanks to the development of cutting-edge experimental techniques for manipulating and probing nano-structures. In particular, the upsurge of spin-polarized scanning tunneling microscope and spectroscopy [6, 8, 13, 16, 18, 20–30], X-ray magnetic circular dichroism [4, 9, 27, 31–33] and electron paramagnetic resonance [3, 7, 10, 30, 34–41] has enabled/spurred/fueled pioneer research works. Additionally, the development of new theoretical methods and the improvement of computational power has also allowed to carry out detailed studies in this field [5, 42–55].

The state-of-the-art research of the field is focused on characterizing magnetic adatom systems and understanding the physical mechanisms involved on the spin dynamics, with the ultimate goal of achieving the control and stability of single adatoms. The magnetic stability is basically determined by the magnetic structure of the adatom together with the interactions interactions with the environment [12]. The high energy barrier separating the ground state and the excited magnetic states on adatom systems, called magnetic anisotropy energy, protects the magnetization reversal from thermal fluctuations [21, 26, 27, 56, 57]. However, the quantum nature of these nano-structures introduces intrinsic quantum fluctuations [50] and enables quantum tunneling of magnetization [58, 59], which tend to destabilize the magnetic states and cause spin relaxation.

Due to the small magnetic moments of adatom systems, interactions with their environment also play a crucial role in their spin dynamics. Electronic interactions with substrate conduction electrons can screen the localized magnetic moment and affect it's stability, which is known as the Kondo effect [17, 60, 61]. In order to reduce the effect of substrate electrons, insulating decoupling layers such as Cu_2N, MgO or graphene have been used successfully, stabilizing the adatom states and achieving long spin-flip relaxation times [4, 11, 14]. Even the coupling between tunneling electrons and the adatom, which makes scanning tunneling spectroscopy possible, affects the spin dynamics of the adatom. This aspect has been studied experimentally [6] and the physical origin of the coupling has been theoretically explored [43, 44]. In the case of electron paramagnetic resonance, many theoretical models have been proposed to capture the essential physics behind the resonant transitions [38, 53], but the origin of the spin transitions is still an open question [41]. On the other hand, while the effect of electronic interactions on adatom properties has been widely studied, the role of substrate phonons has received far less attention so far. Nonetheless, it has been speculated many times about the crucial role of the electron-phonon interaction as a spin relaxation mechanism, and in fact, clear indications of their importance in the relaxation mechanism have been found [62].

The so called electron-phonon interaction is essentially the effect of phonons on the electronic structure. It plays a crucial role in a wide variety of observable phenomena, such as electrical conductivity and resistivity of metals, temperature dependence of carrier mobility, optical properties of semiconductors, or even in conventional superconductivity.

In consequence, it represents one of the classic topics of solid state physics and has been extensively studied from the earliest days of the quantum theory [63–68]. However, due to the high computational costs needed to accurately model this coupling, quantitative first principles calculations of the electron-phonon interaction were only accessible very recently [69].

In this regard, the difficulty of performing first principles calculations of spin lifetimes and transitions rates of magnetic adatoms complicates verifying the origin of the physical mechanisms involved on experimental measurements. Indeed, a convincing theoretical approach to study the contribution of electron-phonon coupling from first principles has been so far inaccessible due to the computational challenge that represents the many-body character of the problem and the huge number of atoms in a surface simulation. In the related field of molecular magnets, *ab-initio* calculations of the spin-phonon coupling have been widely performed using complex electronic structure methods developed on quantum chemistry [70–77]. These methods allow an accurate description of the many-body character of the non-periodic magnetic molecules, however, due to their computational costs, their application on super-cell adatom systems is not feasible.

In this thesis, we develop and apply several numerical methods to account the effects of electron-phonon interaction on magnetic adatoms from first principles. In particular, we analyze the effect of vibrations on the Fe adatom deposited on MgO/Ag(100). Our calculations allow to gain insight into existing experimental results and even to open new possibilities in the study of spin lifetimes of magnetic adatoms. To this end, the thesis is organized as follows. Chapter 1 collects the general theoretical framework on which the thesis is based, namely, obtaining the electronic and vibrational structures from first principles, the crystal field Hamiltonians used to describe the electronic structure of adatom by means of Stevens operators, and the theory of open quantum systems to describe the dynamics of the adatom coupled to the vibrations. Thereafter, in Chapter 2 we make use of the successful theory of electron-phonon interactions developed to study metals, adapted to the special features of adatom systems. By applying the formalism to the Fe adatom on MgO/Ag(100) we characterize the impact of electron-phonon interaction on the electronic states of the adatom, revealing the important features of the electronic and vibrational structures for the electron-phonon coupling. Next, in order to get a better insight into the role of the electron-phonon coupling on spin relaxation, in Chapter 3 we present a

method that combines first principles density functional theory calculations with an atomic multiplet model to access spin lifetimes. We test the method with the Fe adatom on MgO/Ag(100), successfully accounting for the millisecond spin lifetime measured experimentally [6]. Finally, on Chapter 4 we review the most important results obtained and collect the main conclusions of the thesis.

Chapter 1

Theoretical background

In order to study the influence of vibrations on the magnetic moment of an adatom, one needs to consider several theoretical methodologies for a proper description of the problem. Among other features, a good knowledge of the electronic structure of the adatom and the substrate, together with the vibrational structure of the system, are needed. Due to the difficulty of each of all these different aspects, several theoretical frameworks have been developed to study each of them. The aim of this first chapter is to introduce the main points of the different theoretical methods used throughout the next chapters. References cited along the chapter can be checked for more detailed derivations and discussions.

First, in Sec. 1.1 we will introduce the general formalism to solve the problem of a system of interacting electrons and nuclei. We will review some common approximations, such as the adiabatic approximation or the harmonic approximation, that are used in order to arrive to computationally tractable expressions. And we will briefly present the density functional theory (DFT) formalism, one of the most popular methods available in computational physics to compute fundamental material properties from first principles. Next, Sec. 1.1.5 provides a basic derivation of the electron-phonon interaction Hamiltonian up to the first-order in the atomic displacements. Later, Sec. 1.2 will include the theoretical basis for crystal field Hamiltonians, introducing the Stevens equivalent operators. And finally, Sec. 1.3 introduces the concept of the density matrix in quantum mechanics, which is then used to study the dynamics of an open quantum system by deriving a master equation.

1.1 | ELECTRONIC AND VIBRATIONAL STRUCTURES FROM FIRST PRINCIPLES

At the microscopic level, matter is composed by negatively charged electrons interacting with positively charged atomic nuclei or ions. The physical theory governing at this atomic level is quantum mechanics, and the specific properties of materials can be formally derived by solving the corresponding Schrödinger equation. The underlying problem is studied by solid state physics and the theory is well established [66].

1.1.1 | MANY-BODY HAMILTONIAN

The most general Hamiltonian for a non-relativistic system of interacting electrons and nuclei can be written as[1]:

$$\begin{aligned}\hat{H} &= \hat{T}_n + \hat{T}_e + \hat{V}_{nn} + \hat{V}_{ee} + \hat{V}_{en} \\ &= -\sum_I \frac{1}{2M_I}\nabla_I^2 - \sum_i \frac{1}{2}\nabla_i^2 + \frac{1}{2}\sum_I \sum_{J\neq I} \frac{Z_I Z_J}{|\mathbf{R}_I - \mathbf{R}_J|} \\ &\quad + \frac{1}{2}\sum_i \sum_{j\neq i} \frac{1}{|\mathbf{r}_i - \mathbf{r}_j|} - \frac{1}{2}\sum_I \sum_i \frac{Z_I}{|\mathbf{R}_I - \mathbf{r}_i|}\end{aligned} \tag{1.1}$$

With the corresponding many-body Schrödinger equation

$$i\frac{\partial|\Psi(\mathbf{r},\mathbf{R},t)\rangle}{\partial t} = H|\Psi(\mathbf{r},\mathbf{R},t)\rangle. \tag{1.2}$$

Where $\mathbf{R}_I$ is the position vector of a nuclei with mass M_I and atomic number Z_I, and $\mathbf{r}$ represents the set of electron's position vectors $\{\mathbf{r}_i\}$. The first two terms are the kinetic energy of the nuclei and electrons, respectively. The last three terms are the nucleus-nucleus, electron-electron and electron-nucleus Coulomb interactions, respectively.

The Coulomb interaction couples the many constituents of the system, making impossible to get neither analytical nor numeric solutions for

[1] Hartree atomic atomic units will be used through the thesis, i.e. $\hbar = e = m_e = 4\pi\epsilon_0 = 1$

real materials, except for few academic examples. Therefore, the use of approximations is required in order to simplify the problem.

The first approximation is understood by comparing typical velocities of electrons and nuclei within a solid. Electrons move at a much larger speed ($v_e \sim 10^6$ m/s) than atomic nuclei ($v_n \sim 10^3$ m/s) [66]. Consequently, electrons can respond almost immediately to the motion of nuclei, and thus, the electronic state at each moment will be determined by the static position of the ions at that time. This approximation, known as the Born-Oppenheimer approximation, makes possible dividing the wave function of electrons and nuclei by expanding the total wave function in the basis of electronic wave functions as

$$\Psi_i(\mathbf{r},\mathbf{R}) = \sum_{\alpha'} \Phi^{ion}_{i\alpha'}(\mathbf{R})\Psi^{el.}_{\alpha'}(\mathbf{r};\mathbf{R}), \tag{1.3}$$

where $\Psi_i(\mathbf{r},\mathbf{R})$ are the eigenstates of the total system

$$\hat{H}\Psi_i(\mathbf{r},\mathbf{R}) = E_i\Psi_i(\mathbf{r},\mathbf{R}). \tag{1.4}$$

As a consequence, the electronic Hamiltonian will depend parametrically on the set of ionic positions $\mathbf{R}$ and will be time independent. In this case we can introduce the time-independent Schrödinger equation as

$$\begin{aligned}\hat{H}^{el.}\,\Psi^{el.}_{\alpha}(\mathbf{r};\mathbf{R}) &= \left[\hat{T}_e + \hat{V}_{ee} + \hat{V}_{en}(\mathbf{R}) + E_{nn}(\mathbf{R})\right]\Psi^{el.}_{\alpha}(\mathbf{r};\mathbf{R}) \\ &= E^{el.}_{\alpha}(\mathbf{R})\Psi^{el.}_{\alpha}(\mathbf{r};\mathbf{R}).\end{aligned} \tag{1.5}$$

Where $\hat{V}_{nn}(\mathbf{R})$ is now a constant energy $E_{nn}(\mathbf{R})$ and $E^{el.}_{\alpha}(\mathbf{R})$ is the *Born-Oppenheimer energy surface*, where α is the electronic quantum number.

Inserting the expansion (1.3) on Eq. (1.4) and projecting onto the electronic state $\Psi^{el.}_{\alpha}$ we obtain the Schrödinger equation for the nuclei:

$$\begin{aligned}E_i\Phi^{ion}_{i\alpha}(\mathbf{R}) = \left[\hat{T}_n + E^{el.}_{\alpha}\right]|\Phi^{ion}_{i\alpha}(\mathbf{R}) - \sum_{\alpha',I}\frac{1}{2M_I}\langle\Psi^{el.}_{\alpha}|\boldsymbol{\nabla}^2_I|\Psi^{el.}_{\alpha'}\rangle\Phi^{ion}_{i\alpha'}(\mathbf{R}) \\ - 2\sum_{\alpha',I}\frac{1}{2M_I}\langle\Psi^{el.}_{\alpha}|\boldsymbol{\nabla}_I|\Psi^{el.}_{\alpha'}\rangle\boldsymbol{\nabla}_I\Phi^{ion}_{i\alpha'}(\mathbf{R})\end{aligned}, \tag{1.6}$$

where we have used the bra-ket notation for the electronic matrix elements. The last two terms of the equation are called the non-adiabatic terms, which describe the coupling of the electrons with the motion of the

nuclei. Within the adiabatic approximation these terms are not considered [2], giving rise to the ionic time-independent Schrödinger equation

$$\hat{H}^{ion}\Phi_i^{ion}(\mathbf{R}) = \left[\hat{T}_n + E_0^{el.}(\mathbf{R})\right]\Phi_i^{ion}(\mathbf{R}) = E_i^{ion}\Phi_i^{ion}(\mathbf{R}), \tag{1.7}$$

where, as commonly done, we have considered that the electrons are always in their ground state, and thus, we have removed the electronic index from the ionic wave function.

To summarize, the adiabatic approximation enables separating the complex electron and nuclei Schrödinger equation into the simpler electronic (1.5) and ionic (1.7) equations. This approach has proven to be very useful, becoming the standard method used for first principles calculations. On the other hand, neglecting the non-adiabtic term on (1.6) is not a valid approximation in some cases. Nevertheless, even in those cases, the usual approach is to solve the electronic and ionic equations separately and treat the coupling between electrons and atomic displacements afterwards with some perturbative/approximation method.

1.1.2 | DENSITY FUNCTIONAL THEORY

Although the Born-Oppenheimer approximation simplifies the problem of interacting electrons and nuclei, solving the electronic Hamiltonian is still not possible due to the Coulomb interaction between electrons. Different approaches have been adopted to overcome the issue, from free electron models to complex quantum chemistry methods. In this aspect, density functional theory (DFT) has shown to be one of the most extended and successful first principles electronic structure methods.

DFT is based on the work developed by Thomas and Fermi, where the many-body electronic problem was formulated in terms of electron density instead of the many-body wave function. This idea was formulated on mathematical grounds by Hohenberg and Kohn [78]. They proved that the energy of the system is a functional of the density, n, whose global minimum is the ground state energy:

$$E_0 \leqslant E[n]. \tag{1.8}$$

[2] Strictly speaking, the adiabatic approximation consists on neglecting the electronic transitions $\alpha \rightarrow \alpha'$ driven by the nuclear motion, which neglects the off-diagonal terms. Neglecting also the diagonal terms was proposed by Born and Oppenheimer, and accordingly, it is called the Born-Oppenheimer approximation. However, very often both terms are used indistinctly to refer to the Born-Oppenheimer approximation.

In addition, they demonstrated that the ground state density, n_0, uniquely determines the external potential and the many-body wave function, and thus, it also determines all the properties of the system.

The use of the electronic density, instead of the many-body wave function, to determine the properties of the system reduces the dimensionality of the problem to three spatial variables. However, the work of Hohenberg and Kohn does not provide a practical methodology to calculate the ground state electronic density. A general approach for that purpose was proposed by Kohn and Sham [79]. They considered a complementary system made of non-interacting electrons with an effective external potential that produces the same electronic density as the real system. In this way, the many-body Schrödinger equation is replaced by a one-electron Schrödinger equation:

$$\left(-\frac{1}{2}\nabla^2 + \hat{V}_{\mathrm{KS}}(\mathbf{r})\right)\psi_\alpha(\mathbf{r}) = \epsilon_\alpha \psi_\alpha(\mathbf{r}). \tag{1.9}$$

Above, ψ_α are the one electron Kohn-Sham wave functions and V_{KS} is the effective Kohn-Sham potential, which is a functional of the electronic density:

$$\hat{V}_{\mathrm{KS}}[n] = \hat{V}_{en} + \hat{V}_H[n] + \hat{V}_{xc}[n]. \tag{1.10}$$

Here $\hat{V}_{en}$ is the Coulomb interaction between electrons and the atomic nuclei, which only depends on the positions of the ions. $\hat{V}_H[n]$ is the Hartree potential, which represents the Coulomb interaction of the electron density. The last term, $\hat{V}_{xc}[n]$, is the exchange-correlation functional that accounts the quantum many-body effects that are missing in the Hartree potential. In principle, with the exact exchange-correlation functional, DFT would be an exact method. However, its exact expression is unknown and approximated forms are used in practical calculations. In the simplest approximation, the exchange-correlation functional is determined only by the value of the electronic density on each point in space, and the exchange-correlation energy at each point is related to that of an homogeneous electron gas. Accordingly, this approximation takes the name of *local density approximation* (LDA). A more general approximation is known as *general gradien approximation* (GGA), where not only the local electronic density is taken into account, but also its gradient. In all cases, the electron density is computed with the occupied Kohn-Sham states as

$$n(\mathbf{r}) = \sum_\alpha |\psi_\alpha(\mathbf{r})|^2. \tag{1.11}$$

In practice, the Kohn-Sham equation is solved by a self-consistent iterative procedure. Starting from an initial guess for the electron density the Kohn-Sham potential is obtained from its functional expression (1.10). Solving next the Kohn-Sham Schrödinger equation (1.9) a new set of Kohn-Sahm wave functions are obtained. Finally, the new electronic density is computed by (1.11). This electronic density is then used for the next iteration, until the change in the total energy is smaller than a given threshold. This procedure is represented on the flux diagram shown in Figure 1.1.

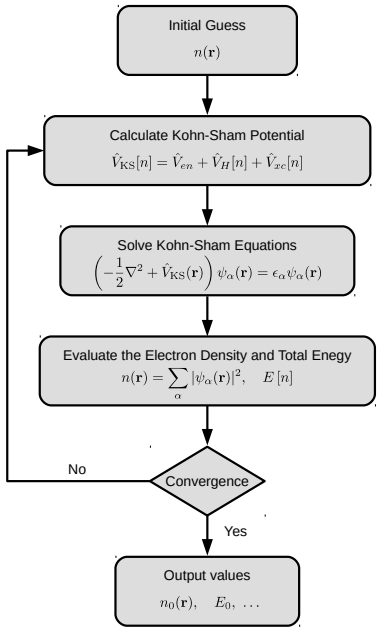

Figure 1.1: Self-consistent loop for solving the Kohn-Sham equation.

For specific details on various aspects of DFT, we refer the reader to Refs. [80, 81].

1.1.3 | HARMONIC APPROXIMATION

In this section we analyze the ionic equation of motion (1.7) within the adiabatic approximation. The Ehrenfest theorem states that the expectation values of quantum mechanical operators obey Newton's classical equations of motion

$$M_I \frac{d\langle \hat{\mathbf{R}}_I \rangle}{dt} = \langle \hat{\mathbf{P}}_I \rangle, \tag{1.12}$$

and

$$\mathbf{F}_I = \frac{d\langle\hat{\mathbf{P}}_I\rangle}{dt} = -\langle\boldsymbol{\nabla}_I V(\hat{\mathbf{R}})\rangle, \tag{1.13}$$

where from Eq. (1.7) we have $V(\mathbf{R}) = E_0^{el.}(\mathbf{R})$. When the curvature of the potential is sufficiently large so that nuclear wave functions do not overlap with each other, the nuclear motion can be treated within a classical picture, and the expectation values can be identified with the classical coordinates of a particle, $\langle\hat{\mathbf{R}}_I\rangle = \mathbf{R}_I$ and $\langle\boldsymbol{\nabla}_I V(\hat{\mathbf{R}})\rangle = \boldsymbol{\nabla}_I V(\mathbf{R})$. Combining Eqs. (1.12) and (1.13) we obtain the Newtonian equation of motion

$$M_I \frac{d^2\mathbf{R}_I}{dt^2} = -\boldsymbol{\nabla}_I E_0^{el.}(\mathbf{R}). \tag{1.14}$$

For a system that depends on a parameter λ, the Hellmann-Feynman theorem states that

$$\frac{dE_i(\lambda)}{d\lambda} = \left\langle \Psi_i(\lambda) \left| \frac{d\hat{H}(\lambda)}{d\lambda} \right| \Psi_i(\lambda) \right\rangle, \tag{1.15}$$

which makes possible to rewrite (1.14) as

$$M_I \frac{d^2\mathbf{R}_I}{dt^2} = -\langle\Psi_0^{el.}(\mathbf{r};\mathbf{R})|\boldsymbol{\nabla}_I \hat{H}^{el.}(\mathbf{r};\mathbf{R})|\Psi_0^{el.}(\mathbf{r};\mathbf{R})\rangle. \tag{1.16}$$

Integration of the above equation is generally referred to as *first principles molecular dynamics*.

In a solid, atomic nuclei oscillate around their equilibrium positions $\mathbf{R}_I^0$ given by $\mathbf{F}_I = 0$. Thus, $\mathbf{R}_I = \mathbf{R}_I^{eq.} + \mathbf{u}_I$, with $\mathbf{u}_I$ being the displacement around the equilibrium position. The Harmonic approximation consists on making a Taylor expansion of the Born-Oppenheimer energy surface around the equilibrium positions, up to the second order in atomic displacements [66]. The first order term will be 0 due to the equilibrium condition $\mathbf{F}_I(\mathbf{R}^{eq.}) = -\boldsymbol{\nabla}_I E_0^{el.}(\mathbf{R})|_{\mathbf{R}=\mathbf{R}^{eq.}} = 0$, and thus, using the κ index to denote the Cartesian directions $\{x, y, z\}$,

$$E_0^{el.}(\mathbf{R}) \approx E_0^{el.}(\mathbf{R}^{eq.}) + \frac{1}{2}\sum_{I,\kappa}\sum_{I,\kappa'} u_I^{\kappa}\, C_{II'}^{\kappa\kappa'}\, u_{I'}^{\kappa'}. \tag{1.17}$$

Above, the so-called *interatomic force constants matrix*, $\hat{\mathbf{C}}_{II'} = (C_{II'}^{\kappa\kappa'})$, is a 3×3 matrix for each pair of atoms $\{I, I'\}$ defined as

$$C_{II'}^{\kappa\kappa'} = \left.\frac{\partial^2 E_0^{el.}(\mathbf{R})}{\partial R_I^{\kappa} \partial R_{I'}^{\kappa'}}\right|_{\mathbf{R}=\mathbf{R}^{eq.}}. \tag{1.18}$$

Using this Harmonic expansion of the potential on the equation of motion (1.14) yields the common equations of coupled harmonic oscillators:

$$M_I \frac{d^2 u_I^\kappa}{dt^2} = -\sum_{I',\kappa'} C_{II'}^{\kappa\kappa'}\, u_{I'}^{\kappa'}. \tag{1.19}$$

It is well known that the solution of this type of linear equations has the form

$$\mathbf{u}(t) = \boldsymbol{\xi} e^{-i\omega t}, \tag{1.20}$$

where ω is the frequency of the oscillating mode, and $\boldsymbol{\xi}$ is the polarization vector of the mode, which determines the amplitude and the phase of each atom. Plugging this guess into the equation of motion (1.19) and making the change of variables $\xi_I^\kappa = M_I^{-1/2}\zeta_I^\kappa$, we obtain the system of coupled linear equations for the polarization vector:

$$\omega^2 \zeta_I^\kappa = \sum_{I',\kappa'} \frac{C_{II'}^{\kappa\kappa'}}{\sqrt{M_I M_{I'}}}\, \zeta_{I'}^{\kappa'}. \tag{1.21}$$

This system of equations has non-zero solutions only when the frequency ω satisfies

$$\det \left| \frac{C_{II'}^{\kappa\kappa'}}{\sqrt{M_I M_{I'}}} - \omega^2 \right| = 0. \tag{1.22}$$

This procedure is an eigenvalue problem with $3N$ different solutions for this equation system, where N is the number of atoms of the system. Each solution, $\mathbf{u}(t) = \boldsymbol{\xi}_\eta e^{-i\omega_\eta t}$, represents a normal mode of the system, where $\eta \in [1, 3N]$.

In the case of a crystal, an atomic nucleus I can be identified by an index that points to its equivalent ion in the primitive unit cell, S, and a lattice vector, $\mathbf{T}$. With this notation $\mathbf{R}_I = \mathbf{R}_{S\mathbf{T}} = \mathbf{R}_S + \mathbf{T}$, and in the same way $\mathbf{R}_{S\mathbf{T}} = \mathbf{R}_S^{eq.} + \mathbf{T} + \mathbf{u}_{S\mathbf{T}}$. Due to the translational symmetry of the lattice, the displacement vectors obey Bloch's theorem,

$$\mathbf{u}_{S\mathbf{T}} = e^{i\mathbf{k}\cdot\mathbf{T}} \mathbf{u}_{S\mathbf{k}}, \tag{1.23}$$

where $\mathbf{k}$ is a crystal momentum vector. The interatomic force constant matrix becomes

$$C_{SS'}^{\kappa\kappa'}(\mathbf{T} - \mathbf{T}') = \left. \frac{\partial^2 E_0^{el.}(\mathbf{R})}{\partial u_{S\mathbf{T}}^\kappa \partial u_{S'\mathbf{T}'}^{\kappa'}} \right|_{\mathbf{R}=\mathbf{R}^{eq.}}. \tag{1.24}$$

Due to the translational symmetry of the lattice, the interatomic force constat matrix depends only on the difference between the two lattice

vectors, $\mathbf{T} - \mathbf{T}'$. It is straightforward to show that Eq. (1.21) can be rewritten in this case as

$$\omega_{\mathbf{k}}^2 \zeta_{S\mathbf{k}}^{\kappa} = \sum_{S',\kappa'} D_{SS'}^{\kappa\kappa'}(\mathbf{k})\, \zeta_{S'\mathbf{k}}^{\kappa'}, \tag{1.25}$$

where,

$$D_{SS'}^{\kappa\kappa'}(\mathbf{k}) = \frac{C_{SS'}^{\kappa\kappa'}(\mathbf{k})}{\sqrt{M_I M_{I'}}} = \sum_{\mathbf{T}} e^{i\mathbf{k}\cdot\mathbf{T}} \frac{C_{SS'}^{\kappa\kappa'}(\mathbf{T})}{\sqrt{M_I M_{I'}}}, \tag{1.26}$$

is the *dynamical matrix*. Finally, the normal modes are obtained by solving the general eigenvalue problem as shown previously. In this case, normal modes, $\mathbf{u}(t) = \boldsymbol{\xi}_{\eta\mathbf{k}} e^{i[\mathbf{k}\cdot\mathbf{T} - \omega_{\eta\mathbf{k}} t]}$, are waves travelling through the crystal with an associated crystal momentum vector $\mathbf{k}$, and are called phonons.

The theory developed above describes the motion of the expected value of the atomic nuclear position. However, this classical picture of lattice vibrations is not adequate to explain several phenomena, such as the Dulong Petit law for the specific heat.

In order to include the quantum nature of the atomic nuclei within the harmonic approximation, it is convenient to introduce the normal coordinates

$$Q_\eta = \sum_{I\kappa} \sqrt{M_I} \zeta_\eta^{I\kappa} u_I^\kappa, \tag{1.27}$$

and the corresponding momentum operators

$$\Pi_\eta = \sum_{I\kappa} \frac{1}{\sqrt{M_I}} \zeta_\eta^{I\kappa} p_I^\kappa, \tag{1.28}$$

where we have used the momentum operator for the nuclei

$$\mathbf{p}_I = -i\boldsymbol{\nabla}_I. \tag{1.29}$$

These operators, as the position and momentum operators, satisfy the usual canonical commutation relations:

$$[Q_\eta, Q_{\eta'}] = [\Pi_\eta, \Pi_{\eta'}] = 0 \tag{1.30}$$

and

$$[Q_\eta, \Pi_{\eta'}] = i\delta_{\eta,\eta'}. \tag{1.31}$$

It can be shown that, using Eq. (1.21), the ionic Hamiltonian of Eq. (1.7) with the harmonic expansion of the Born-Oppenheimer energy surface

developed on Eq. (1.17) can be written as

$$\hat{H}^{ion} = \sum_{\eta} \left(\frac{\Pi_{\eta}^2}{2} + \frac{1}{2}\omega_{\eta}^2 Q_{\eta}^2 \right). \tag{1.32}$$

This is the Hamiltonian of $3N$ independent quantum harmonic oscillators. In analogy, it is possible to define the second quantization creation and annihilation operators, or the so-called *ladder operators*, as

$$b_{\eta}^{\dagger} = \left(\sqrt{\frac{\omega_{\eta}}{2}} Q_{\eta} - i \frac{1}{\sqrt{2\omega_{\eta}}} \Pi_{\eta} \right) \tag{1.33}$$

and

$$b_{\eta} = \left(\sqrt{\frac{\omega_{\eta}}{2}} Q_{\eta} + i \frac{1}{\sqrt{2\omega_{\eta}}} \Pi_{\eta} \right). \tag{1.34}$$

The ionic Hamiltonian can then be rewritten as

$$\hat{H}^{ion} = \sum_{\eta} \omega_{\eta} (b_{\eta}^{\dagger} b_{\eta} + \frac{1}{2}). \tag{1.35}$$

Finally, the ionic wave function can be written in the occupation number formalism as

$$|\Phi_i^{ion}\rangle = |n_1, \ldots, n_{\eta}, \ldots\rangle = \prod_{\eta} \frac{(b_{\eta}^{\dagger})^{n_{\eta}}}{\sqrt{n_{\eta}!}} |0\rangle, \tag{1.36}$$

where $|0\rangle$ represents the ground state (i.e., the state that contains no vibrations on the system) and $i = \{n_{\eta}\}$.

1.1.4 | DIRECT METHOD

Although the procedure to obtain the normal modes or vibrations of a system is clear, one has to compute the interatomic force constant matrix first. Different methods have been developed for that purpose in the literature, each one with its advantages and disadvantages. Among them, density functional perturbation theory (DFPT) has become a very popular method to compute the interatomic force constants from first principles. However, with the big super-cells needed to simulate adatom structures, the computational cost increases remarkably with the size of

the system of interest. For those situations the so-called *direct method* shows a better scalability.

In the direct method, each atom is displaced from its equilibrium position in every cartesian direction, and the interatomic force constants are obtained differentiating the Hellmann-Feynman forces, where the derivative is approximated by a finite difference formula of the type

$$C_{II'}^{\kappa\kappa'} = -\frac{F_I^\kappa(\mathbf{R} + \mathbf{u}_{I'}^{\kappa'}) - F_I^\kappa(\mathbf{R} - \mathbf{u}_{I'}^{\kappa'})}{2u_{I'}^{\kappa'}}. \tag{1.37}$$

Here $\mathbf{u}_{I'}^{\kappa'} = (0 \dots u_{I'}^{\kappa'} \dots 0)$ is the displacement vector of the atom I' along direction κ', and F_I^κ is the Hellmann-Feynman force that experiences atom I on the κ direction.

In order to compute the phonons of a periodic crystal, the primitive unit cell has to be replicated along space, creating an equivalent supper-cell. Then, the supper-cell is used to compute the interatomic force constants between atoms separated by a lattice vector $\mathbf{T}$. For that purpose one can move each atom of the original unit cell, $\mathbf{T}_0$, and compute the force that the displacement creates on all the atoms of the super-cell

$$C_{S\mathbf{T}S'}^{\kappa\kappa'}(\mathbf{T} - \mathbf{T}_0) = -\frac{F_{S\mathbf{T}}^\kappa(\mathbf{R} + \mathbf{u}_{S'\mathbf{T}_0}^{\kappa'}) - F_{S\mathbf{T}}^\kappa(\mathbf{R} - \mathbf{u}_{S'\mathbf{T}_0}^{\kappa'})}{2u_{S'\mathbf{T}_0}^{\kappa'}}. \tag{1.38}$$

Finally, the phonon frequencies and polarization vectors are obtained by computing the dynamical matrix and solving the general eigenvalue problem shown in the previous section. The procedure of obtaining the dynamical matrix on crystal momentum from a supper-cell is called unfolding.

The disadvantage of this method is that with a supper-cell of size (N_x, N_y, N_z) only the phonon structure for a crystal momentum of the form $\mathbf{k} = (\frac{i}{N_x}, \frac{j}{N_y}, \frac{k}{N_z})$ can be calculated, where $i \in [0, N_x - 1]$, $j \in [0, N_y - 1]$ and $k \in [0, N_z - 1]$. This makes the direct method computationally very expensive to compute the phonon structure for small crystal momentum.

However, the present method can be improved making an intelligent use of the symmetries of the system. In first place, if atoms $\tilde{I}$ and $\tilde{J}$ are equivalent to atoms I and J by means of the symmetry operations $\hat{\mathbf{S}}$, respectively. Then, the interatomic force constant matrix has the following property:

$$\hat{\mathbf{C}}_{\tilde{I}\tilde{J}} = \hat{\mathbf{S}}\,\hat{\mathbf{C}}_{IJ}\,\hat{\mathbf{S}}^{-1}. \tag{1.39}$$

This implies that it is not necessary to displace all the atoms of the system, but just the set of irreducible atoms. In order to take advantage of the symmetries, it is useful to use a matrix formalism. We define the displacement 3×3 matrix as

$$\hat{\mathbf{U}}_J = \begin{pmatrix} \mathbf{u}_J^x & \mathbf{u}_J^y & \mathbf{u}_J^z \end{pmatrix}, \tag{1.40}$$

where the vectors $\mathbf{u}_J^{x,y,z}$ are column vectors of the displacement of atom J along the three Cartesian directions. In the same way, we define the 3×3 force matrix as

$$\hat{\mathbf{F}}_I = \begin{pmatrix} \mathbf{F}_I^x & \mathbf{F}_I^y & \mathbf{F}_I^z \end{pmatrix}, \tag{1.41}$$

where the vectors $\mathbf{F}_I^{x,y,z}$ are force that atom I experiences due to the displacements of the atom J along each Cartesian direction. These matrices are thus related by the interatomic force constant matrix as

$$\hat{\mathbf{F}}_I = -\hat{\mathbf{C}}_{IJ}\,\hat{\mathbf{U}}_J. \tag{1.42}$$

Because the three Cartesian displacement vectors are linearly independent, it is easy to show that $|\hat{\mathbf{U}}_J| \neq 0$, and that the displacement matrix $\hat{\mathbf{U}}_J$ is invertible. Therefore, with this notation the interatomic force constant matrix can be computed straightforwardly by solving the system of linear equations above, whose solution is

$$\hat{\mathbf{C}}_{IJ} = -\hat{\mathbf{F}}_I\,\hat{\mathbf{U}}_J^{-1}. \tag{1.43}$$

This method to obtain the force constant matrix of a pair of atoms can be generalized. In fact, any number of arbitrary displacement vectors can be used instead of the three Cartesian displacement vectors. In that case the displacement matrix

$$\hat{\mathbf{U}}_J = \begin{pmatrix} \mathbf{u}_J^1 & \mathbf{u}_J^2 & \dots & \mathbf{u}_J^N \end{pmatrix}, \tag{1.44}$$

and the force matrix

$$\hat{\mathbf{F}}_I = \begin{pmatrix} \mathbf{F}_I^1 & \mathbf{F}_I^2 & \dots & \mathbf{F}_I^N \end{pmatrix}, \tag{1.45}$$

will be $3 \times N$ matrices. In this case, the linear equation (1.42) still can be solved using the so-called *Moore–Penrose inverse* or *pseudoinverse* of a matrix ($\hat{\mathbf{U}}_J^+$):

$$\hat{\mathbf{C}}_{IJ} = -\hat{\mathbf{F}}_I\,\hat{\mathbf{U}}_J^+. \tag{1.46}$$

The pseudoinverse of a $m \times n$ matrix $\hat{\mathbf{A}}$ only exists when $rank(\hat{\mathbf{A}}) = min\{m, n\}$. In the case of the displacement matrix the necessary condition for the pseudoinverse to exist is then $rank(\hat{\mathbf{U}}_J) = 3$. This means that at least three linearly independent displacement vectors and their corresponding forces must be used to compute the interatomic force constants.

Making use of the symmetries of the point group $\{\hat{\mathbf{S}}_{is}\}$ of the atom J, where $is = 1, \ldots, N_{sym}$, it is possible to define a minimal set of displacement vectors, $\{\mathbf{u}^i_J\}$, where

$$\hat{\mathbf{U}}_J = \begin{pmatrix} \ldots & \hat{\mathbf{S}}_{is}\mathbf{u}^i_J & \ldots & \hat{\mathbf{S}}_{N_{sym}}\mathbf{u}^i_J & \ldots \end{pmatrix}, \tag{1.47}$$

satisfies $rank(\hat{\mathbf{U}}_J) = 3$. For example, in the case of a system with cubic symmetry one displacement is sufficient to satisfy this condition. Then, the force matrix of the atom I can be computed applying the symmetry operation $\hat{\mathbf{S}}_{is}$ to the force felt by the atom equivalent by the symmetry operation, I_{is}:

$$\hat{\mathbf{F}}_I = \begin{pmatrix} \ldots & \hat{\mathbf{S}}_{is}\mathbf{F}^i_{I_{is}} & \ldots & \hat{\mathbf{S}}_{N_{sym}}\mathbf{F}^i_{I_{is}} & \ldots \end{pmatrix}. \tag{1.48}$$

Finally, the force constant matrix can be computed using Eq. (1.46). The advantage of using this method is that the force constants matrix satisfies the symmetries of the system by construction, satisfying the condition shown in Eq. (1.39). Additionally, the number of displacements needed to compute the vibrational structure of a system can be considerably reduced, which is of paramount importance on large systems.

1.1.5 | ELECTRON-PHONON INTERACTION

In the previous sections we have studied the separated electronic and ionic problems thanks to the adiabatic approximation. However, the presented formalism is not sufficient to describe certain experimentally observed phenomena. In those cases, the coupling of the electrons with the atomic displacements has to be included. This coupling is the so-called *electron-phonon interaction* and it is related to the last two terms neglected in Eq. (1.6). Here we limit the analysis to first order contributions with respect to the ionic positions, which is in most cases sufficient to explain many physical phenomena [67]. The state-of-the-art first principles research on this field take DFT calculations as the starting point for analyzing the electron-phonon interaction [69]. Therefore, making a

first order Taylor expansion for the Kohn-Sham potential in the atomic displacements:

$$\hat{V}_{\mathrm{KS}}(\mathbf{r};\mathbf{R}) \approx \hat{V}_{\mathrm{KS}}(\mathbf{r};\mathbf{R}_0) + \sum_{I\kappa} \partial\hat{V}_{I\kappa} u_I^\kappa, \tag{1.49}$$

where the variation of the Kohn-Sham potential

$$\partial\hat{V}_{I\kappa} = \left.\frac{d\hat{V}_{\mathrm{KS}}(\mathbf{r};\mathbf{R})}{du_I^\kappa}\right|_{\mathbf{R}=\mathbf{R}_0} \tag{1.50}$$

has to be computed self-consistently.

Equivalently, we can use the normal coordinates defined in Sec. 1.1.3, and in that case:

$$\hat{V}_{\mathrm{KS}}(\mathbf{r};\mathbf{R}) \approx \hat{V}_{\mathrm{KS}}(\mathbf{r};\mathbf{R}_0) + \sum_{\eta} \partial\hat{V}_{\eta} Q_\eta, \tag{1.51}$$

where now

$$\partial\hat{V}_{\eta} = \left.\frac{d\hat{V}_{\mathrm{KS}}(\mathbf{r};\mathbf{R})}{dQ_\eta}\right|_{\mathbf{R}=\mathbf{R}_0}. \tag{1.52}$$

As a result of the Taylor expansion, the electron-phonon Hamiltonian can be written in second quantization formalism, with creation and annihilation operators $c^\dagger$ and c for Kohn-Sham single particle electron states, and phonon creation and annihilation operators $b^\dagger$ and b as defined in Sec. 1.1.3, as

$$\hat{H}_{el.-ph.} = \sum_{\eta}\sum_{\alpha,\alpha'} g^\eta_{\alpha\alpha'} c^\dagger_\alpha c_{\alpha'} \left(b^\dagger_\eta + b_\eta\right). \tag{1.53}$$

Here, $g^\eta_{\alpha\alpha'}$ are the *electron-phonon matrix elements* defined from the self-consistent derivative of the Kohn-Sham potential in Eqs. (1.50) and (1.52) as

$$g^\eta_{\alpha\alpha'} = \frac{1}{\sqrt{2\omega_\eta}}\langle\psi_\alpha|\partial\hat{V}_\eta|\psi_{\alpha'}\rangle = \sum_{I\kappa}\frac{\zeta^{I\kappa}_\eta}{\sqrt{2M_I\omega_\eta}}\langle\psi_\alpha|\partial\hat{V}_{I\kappa}|\psi_{\alpha'}\rangle. \tag{1.54}$$

This reformulation of the electron-phonon Hamiltonian is known as the Fröhlich Hamiltonian, and it is usually the starting point of many electron-phonon studies.

1.2 | Crystal Field and Stevens operators

Studying how an adatom is influenced by the substrate where it has been deposited is of crucial importance to properly determine its magnetic properties. In this section we will study the energy splittings of the electronic states of the adatoms produced by the interaction with its surrounding environment. This can be described by the *crystal field theory*, which has been widely used to describe the magnetic properties of molecular magnets and single adatoms on surfaces [12, 82–84].

The electronic Hamiltonian for a magnetic adatom on a surface including the most relevant interactions for the problem can be written as

$$\hat{H} = \hat{T}_e + \hat{V}_{en} + \hat{V}_{ee} + \hat{V}_{es} + \hat{V}_{SO}. \tag{1.55}$$

Where $\hat{T}_e$ is the kinetic energy of electrons, $\hat{V}_{en}$ the Coulomb interaction between the electrons and the atomic nucleus, $\hat{V}_{ee}$ the electronic Coulomb interaction. These first three terms describe the Hamiltonian of a free atom as given by the more general Hamiltonian given in Eq. (1.1). The next term, $\hat{V}_{es}$ the interaction between the electrons and the surface, and finally, $\hat{V}_{SO}$ is the spin-orbit interaction.

Taking into account all the microscopic characteristics of the surface is a complicated task, i. e., the interaction of the atom electrons with the surface nuclei and electrons. In principle, different methods could be used for that, but, for example, DFT struggles with the high correlation present on d or f orbitals, and more complex quantum chemical methods struggle with the big super-cells needed to represent an atom deposited on a surface. In that context, different models have been developed in the past to study the problem. In the so-called *crystal field theory* the surface is treated like an electrostatic potential that the atomic electrons feel, where, the electron surface interaction is represented as

$$\hat{V}_{es} = \sum_i V_{CF}(\mathbf{r}_i). \tag{1.56}$$

The different interactions present on the Hamiltonian (1.55) are ordered from greater to lower strength for a d shell atom. In this way perturbation theory can be used to study each term hierarchically. In the case of f electrons, the effect of the spin-orbit interaction tends to be

stronger than the crystal field, and therefore, in a perturbative analysis the spin-orbit interaction has to be taken into account before the crystal field. As the aim of this section is to demonstrate that the effect of the crystal field can be taken into account using the so-called *Stevens operators*, the spin-orbit interaction will not be considered. In this situation the following analysis will be based on total orbital angular momentum $\mathbf{L} = \sum_i \mathbf{L}_i$ and total spin $\mathbf{S} = \sum_i \mathbf{S}_i$ operators, and the effect of the spin-orbit interaction can be added at a later stage. However, when the spin-orbit interaction is stronger than the crystal field, its effect must be added first, and the derivation shown in the following lines for the crystal field must be reformulated in therms of total angular momentum $\mathbf{J} = \mathbf{L} + \mathbf{S}$.

Starting from the Hydrogen like atom Hamiltonian

$$\hat{H} = \hat{T}_e + \hat{V}_{en}, \tag{1.57}$$

it is well known that the eigenfunctions are of the form

$$\psi_{nlm}(\mathbf{r}) = R_{nl}(r) Y_l^m(\Omega), \tag{1.58}$$

and the energy levels are the usual $1s$, $2s$, $2p$, ... states. For each atom, the electronic configuration is determined by the number of electrons in the outer shell. In this case the ground state is highly degenerate, the degeneracy being

$$\binom{N}{N_e} = \frac{N!}{(N-N_e)!\, N_e!}, \tag{1.59}$$

where N_e is the number of electrons on the outer shell and N is the number of states of the outer shell. On an atomic orbital l there are $N_l = 2(l+1)$ different m_l states, hence, taking into account the spin degree of freedom $N = 2N_l$.

When the electron-electron interaction is added,

$$\hat{H} = \hat{T}_e + \hat{V}_{en} + \hat{V}_{ee}, \tag{1.60}$$

the degeneracy is broken. As the Hamiltonian commutes with the total orbital angular momentum and the total spin operators,

$$\left[\hat{H}, \mathbf{L}\right] = \left[\hat{H}, \mathbf{S}\right] = 0, \tag{1.61}$$

then the eigenvectors can be labeled using the quantum numbers of total orbital angular momentum and spin as

$$|L, M_L, S, M_S\rangle, \tag{1.62}$$

and each set of L, S quantum numbers will form a degenerate subspace that it is labeled as ${}^{2S+1}L$ and it is called a term symbol. The degeneracy of a subspace is reduced now to $(2L+1)(2S+1)$. It is well known that Hund's rules determine the lowest energy subspace. These rules are:

1. Highest total spin, S, has lowest energy.
2. Largest total orbital angular momentum, L, has lowest energy.
3. If the shell is more than half-filled, then the highest value of total angular momentum J has lowest energy; if the orbital is half-filled or less, then the lowest total angular momentum has lowest energy.

As an example, the ground state term for an Fe atom is ${}^5D$, which has $L = 2$ and $S = 2$, and is composed of 25 degenerated states.

The effect of the crystal field on the atomic energy levels will be studied now using perturbation theory. As each subspace has $(2L + 1)(2S + 1)$ states, degenerated perturbation theory must be used, and thus

$$\langle L, M_L, S, M_S|\hat{V}_{CF}|L, M'_L, S, M'_S\rangle \tag{1.63}$$

matrix elements should be computed. Because the crystal field is an electrostatic potential, it is a one-body operator. Using second quantization formalism it can be easily shown that a one-body operator only connects multi-electronic or multiplet states $|L, M_L, S, M_S\rangle$ that differ at most on one electronic orbital state. In consequence, the matrix elements are related to the single electron matrix elements

$$\langle\psi_{nlm}|V_{CF}|\psi_{nlm'}\rangle = \int \psi^*_{nlm}(\mathbf{r})V_{CF}(\mathbf{r})\psi_{nlm'}(\mathbf{r})\, d\mathbf{r}. \tag{1.64}$$

If the crystal field potential is expanded using spherical harmonics as

$$V_{CF}(\mathbf{r}) = \sum_{L=0}^{\infty}\sum_{M=-L}^{L} V_{LM}(r)Y_L^M(\Omega), \tag{1.65}$$

and using Eq. (1.58), the matrix elements can be written as

$$\langle\psi_{nlm}|V_{CF}|\psi_{nlm'}\rangle = \sum_{LM}\langle V_{LM}\rangle g_{L,l,l}^{M,m,m'}. \tag{1.66}$$

Here

$$\langle V_{LM}\rangle = \int r^2\,|R_{nl}(r)|^2\,V_{LM}(r)\,dr \tag{1.67}$$

is the expectation value of V_{LM} for the outer shell electrons, and

$$g_{L,l,l}^{M,m,m'} = \int \overline{Y_l^m}(\Omega) Y_L^M(\Omega) Y_l^{m'}(\Omega)\, d\Omega \tag{1.68}$$

are called Gaunt coefficients, which determine the selection rules for the matrix elements.

Stevens developed a method to compute these crystal field matrix elements using equivalent angular momentum operators to represent the spherical harmonics. These equivalent operators are known as *Stevens operators*, and can be used to expand the crystal field as

$$\hat{V}_{CF} = \sum_{k=0,2,\ldots} \sum_{q=-k}^{k} B_k^q \hat{O}_k^q(\mathbf{L}). \tag{1.69}$$

The coefficients B_k^q are related to the expectation value $\langle V_{LM} \rangle$, and the Stevens operators $\hat{O}_k^q$ have the same selection rules for the non-zero matrix elements as the Gaunt coefficients above. In the case of an atom with an outer f orbital, as the spin-orbit interaction is stronger than the crystal field, the same procedure can be applied in the basis of total angular momentum $|J, M_J\rangle$, and the Stevens operators are written in terms of total angular momentum $\hat{O}_k^q(\mathbf{J})$.

Once the coefficients of the crystal field expansion are computed, the splittings of the energy levels can be accessed by diagonalizing the matrix. One of the most extended approaches to obtain the crystal field expansion is by choosing the B_k^q parameters to fit some available experimental data. Getting the expansion form first principles is however more difficult, and often the results obtained are not in good agreement with experiments. Different methods have been explored for that purpose, such as getting the expansion from DFT calculations [85] or from a point charge model of the surface [86]. In this last case, the Coulomb potential of the point charges is expanded in spherical harmonics, which is known as the spherical multipole moments expansion. Next, the matrix elements are computed using Eq. (1.66). Finally, tabulated prefactors that relate the Stevens operators with the spherical harmonics are used to compute the B_k^q coefficients.

1.3 | Open quantum systems and master equations

Any real quantum system interacts with it's environment, which influences the dynamics of the system to a greater or lesser extent. Many interesting effects can't be explained without taking into account this coupling. Quantum decoherence, for example, can be understood as a transfer of information from the system to the environment. As another example, in order to properly describe a precessing magnetic moment, one must also include the damping to the surrounding atoms. For this reason, a complete description of the so-called *open quantum systems* must also include the degrees of freedom of the environment on the wave function. However, except for some academic systems, a microscopic description of the environment is impossible. This motivated the development of *quantum master equations* to study the dynamics of open quantum systems in terms of the *density matrix* formalism. A more detailed description about the formalism than the presented here can be found for example in Ref. [87].

1.3.1 | Density matrix

The density matrix is a generalization of a quantum state. A wave functions describes a *pure state*, while the density matrix can also represent a *mixed state*. A mixture of states is a statistical ensemble of independent systems, and is represented by the density matrix or density operator as

$$\hat{\rho} = \sum_i p_i |\Psi_i\rangle\langle\Psi_i|, \tag{1.70}$$

where p_i is the probability of finding the system in state Ψ_i. Within this formalism, the expectation value of of an observable $\hat{O}$ is given by the statistical average of the ensemble as

$$\langle\hat{O}\rangle = \sum_i p_i \langle\hat{O}\rangle_i = \mathrm{Tr}\{\hat{O}\,\hat{\rho}\}, \tag{1.71}$$

where $\langle\hat{O}\rangle_i$ is the expectation value of for the pure state $|\Psi_i\rangle$, and Tr denotes the trace of a matrix.

The dynamics of the density matrix are described by the Liouville - von-Neumann equation:

$$\frac{d\hat{\rho}(t)}{dt} = -i\left[\hat{H}, \hat{\rho}(t)\right]. \tag{1.72}$$

1.3.2 | REDUCED DENSITY MATRIX

An open quantum system is in general a quantum system $\mathcal{A}$ coupled to it's environment $\mathcal{B}$, and the Hilbert space of the total system will be given by the tensor product $\mathcal{H} = \mathcal{H}_\mathcal{A} \otimes \mathcal{H}_\mathcal{B}$. It is common to consider that the environment $\mathcal{B}$ is composed of an infinite number of degrees of freedom, and that it remains in a thermal equilibrium state, even if it interacts with system $\mathcal{A}$. In that case, the system is said to be coupled with a *bath*.

The expectation value of an observable $\hat{O}$ acting on the Hilbert space of the system $\mathcal{H}_\mathcal{A}$ is determined by

$$\langle\hat{O}\rangle = \mathrm{Tr}_\mathcal{A}\{\hat{O}\,\hat{\rho}_\mathcal{A}\}, \tag{1.73}$$

with the *reduced density matrix* defined as

$$\hat{\rho}_\mathcal{A} = \mathrm{Tr}_\mathcal{B}\{\hat{\rho}\}. \tag{1.74}$$

The partial traces are defined as

$$\mathrm{Tr}_\mathcal{A}\{\hat{O}\} = \sum_A \langle A|\hat{O}|A\rangle, \tag{1.75}$$

where $\{|A\rangle\}$ is the set of orthonormal eigenvectors of system $\mathcal{A}$.

It is clear then that the reduced density matrix gives all the information about any observable of the system $\mathcal{A}$, hence, it is a quantity of central interest on the theory of open quantum systems. The time evolution of the reduced density matrix is obtained by making the partial trace over the degrees of freedom of the bath on the Liouville - von-Neumann equation:

$$\frac{d\hat{\rho}_\mathcal{A}(t)}{dt} = -i\mathrm{Tr}\left\{\left[\hat{H}, \hat{\rho}(t)\right]\right\}. \tag{1.76}$$

Traceing out the degrees of freedom of the bath makes the evolution of the reduced density matrix non-unitary, which leads out to the irreversible behavior of open quantum systems and gives rise to effects such as quantum decoherence.

1.3.3 | BORN-MARKOV APPROXIMATION

In order to study the effect of the coupling between the system and the bath, the above exact equations must be further developed by making use of approximations that result io more tractable expressions. As the development of the above equations is more easily done in the interaction picture, it is convenient to distinguish the coupling term in the Hamiltonian of the complete system as

$$\hat{H} = \hat{H}_0 + \hat{V}. \tag{1.77}$$

Here $\hat{H}_0 = \hat{H}_{\mathcal{A}} + \hat{H}_{\mathcal{B}}$ contains the Hamiltonians of the system and the bath, and $\hat{V}$ is the interaction between both systems. Therefore, in the interaction picture, the time dependence of an operator $\hat{O}$ belonging to the Schrödinger picture is

$$\tilde{O}(t) = e^{i\hat{H}_0 t}\hat{O}e^{-i\hat{H}_0 t}. \tag{1.78}$$

Taking this into account, the Liouville - von Neumann equation for the reduced density matrix becomes

$$\frac{d\tilde{\rho}_{\mathcal{A}}(t)}{dt} = -i\,\mathrm{Tr}_{\mathcal{B}}\left\{\left[\tilde{V}(t), \tilde{\rho}(t)\right]\right\}. \tag{1.79}$$

Integrating this equation,

$$\tilde{\rho}_{\mathcal{A}}(t) = \tilde{\rho}_{\mathcal{A}}(t_0) - i\,\mathrm{Tr}_{\mathcal{B}}\left\{\int_{t_0}^{t} dt'\left[\tilde{V}(t'), \tilde{\rho}(t')\right]\right\}, \tag{1.80}$$

and inserting the expression in Eq. (1.79) yields

$$\frac{d\tilde{\rho}_{\mathcal{A}}(t)}{dt} = -i\mathrm{Tr}_{\mathcal{B}}\left\{\left[\tilde{V}(t), \tilde{\rho}(t_0)\right]\right\} - \int_{t_0}^{t} dt'\mathrm{Tr}_{\mathcal{B}}\left\{\left[\tilde{V}(t), \left[\tilde{V}(t'), \tilde{\rho}(t')\right]\right]\right\}. \tag{1.81}$$

If we prepare the system and the bath at the initial time t_0 to be on an uncorrelated product state $\tilde{\rho}(t_0) = \tilde{\rho}_{\mathcal{A}} \otimes \tilde{\rho}_{\mathcal{B}}$, where $\tilde{\rho}_{\mathcal{B}}$ represents some reference state for the bath, such as a thermal equilibrium $\rho_{\mathcal{B}}^{eq.}$, then, the

first term in Eq. (1.81) will be

$$\begin{aligned}
\mathrm{Tr}_{\mathcal{B}}\left\{\left[\tilde{V}(t),\tilde{\rho}(t_0)\right]\right\} &= \sum_{B}\Big(\langle A,B|\tilde{V}(t)\tilde{\rho}_{\mathcal{A}}(t_0)\rho_{\mathcal{B}}^{eq.}|A',B\rangle \\
&\qquad - \langle A,B|\tilde{\rho}_{\mathcal{A}}(t_0)\rho_{\mathcal{B}}^{eq.}\tilde{V}(t)|A',B\rangle\Big) \\
&= \sum_{B,A_1,B_1}\Big(\langle A,B|\tilde{V}(t)|A_1,B_1\rangle\langle A_1,B_1|\tilde{\rho}_{\mathcal{A}}(t_0)\rho_{\mathcal{B}}^{eq.}|A',B\rangle \\
&\qquad - \langle A,B|\tilde{\rho}_{\mathcal{A}}(t_0)\rho_{\mathcal{B}}^{eq.}|A_1,B_1\rangle\langle A_1,B_1|\tilde{V}(t)|A',B\rangle\Big) \\
&= \sum_{B,A_1,B_1}\frac{e^{-\beta E_B}}{Z_{\mathcal{B}}}\delta_{B_1,B} \\
&\qquad \times\Big(\langle A,B|\tilde{V}(t)|A_1,B_1\rangle\langle A_1|\tilde{\rho}_{\mathcal{A}}(t_0)\,|A'\rangle \\
&\qquad - \langle A|\tilde{\rho}_{\mathcal{A}}(t_0)|A_1\rangle\langle A_1,B_1|\tilde{V}(t)|A',B\rangle\Big) \\
&= \sum_{B,A_1}\frac{e^{-\beta E_B}}{Z_{\mathcal{B}}}\Big(\langle A,B|\tilde{V}(t)|A_1,B\rangle\langle A_1|\tilde{\rho}_{\mathcal{A}}(t_0)|A'\rangle \\
&\qquad - \langle A|\tilde{\rho}_{\mathcal{A}}(t_0)|A_1\rangle\langle A_1,B|\tilde{V}(t)|A',B\rangle\Big). \qquad (1.82)
\end{aligned}$$

Here $Z_{\mathcal{B}}$ is the partition function of the bath and E_B the energy of state $|B\rangle$. This term will be zero if the interaction $\hat{V}$ mixes only different $|B\rangle$ states, i.e., $\langle A_1,B|\tilde{V}(t)|A',B\rangle = 0$. If this is not the case, the diagonal part of the interaction can be included in the Hamiltonian of the bath $\hat{H}_{\mathcal{B}}$. Thus, the time evolution of the density matrix will be given by

$$\frac{d\tilde{\rho}_{\mathcal{A}}(t)}{dt} = -\int_{t_0}^{t}dt'\mathrm{Tr}_{\mathcal{B}}\left\{\left[\tilde{V}(t),\left[\tilde{V}(t'),\tilde{\rho}(t')\right]\right]\right\}. \qquad (1.83)$$

At this point, the *Born approximation* assumes that the interaction is weak, and the eigenstates of the system and bath will not be altered significantly. In such limit we can factorize the density matrix to be $\tilde{\rho}(t) = \tilde{\rho}_{\mathcal{A}}(t)\otimes\tilde{\rho}_{\mathcal{B}}(t)$. Additionally, if the dynamics of the bath are much faster than the dynamics of the system, the excitations of the bath caused by the system will decay quickly, and one can consider that the density matrix of the bath is always its equilibrium density matrix $\rho_{\mathcal{B}}^{eq.}$, and correlation with the bath will be lost quickly. Within this assumption, the system will depend only on its current state $\tilde{\rho}_{\mathcal{A}}(t)$, meaning that it has no memory of its state in the past, which is called a *Markovian system*. Then, replacing $\tilde{\rho}_{\mathcal{A}}(t')$ by $\tilde{\rho}_{\mathcal{A}}(t)$, the time evolution of the dynamics within the

Born-Markov approximation is given by:

$$\frac{d\tilde{\rho}_{\mathcal{A}}(t)}{dt} = -\int_{t_0}^{t} dt' \mathrm{Tr}_{\mathcal{B}} \left\{ \left[\tilde{V}(t), \left[\tilde{V}(t'), \tilde{\rho}_{\mathcal{A}}(t) \tilde{\rho}_{\mathcal{B}}^{eq.} \right] \right] \right\}. \tag{1.84}$$

This equation is called the Redfield equation, and is not yet a Markovian equation, since it still depends on the initial state of the system at t_0. Making the change of variable $t' = t - s$, and with the assumption of the fast correlation decay of the bath compared to the evolution of the system, $\tau_{\mathcal{B}} \ll t - t_0 \approx \infty$, with $\tau_{\mathcal{B}}$ the characteristic correlation time of the bath, the above equation becomes

$$\frac{d\tilde{\rho}_{\mathcal{A}}(t)}{dt} = -\int_{0}^{\infty} ds \mathrm{Tr}_{\mathcal{B}} \left\{ \left[\tilde{V}(t), \left[\tilde{V}(t-s), \tilde{\rho}_{\mathcal{A}}(t) \tilde{\rho}_{\mathcal{B}}^{eq.} \right] \right] \right\}. \tag{1.85}$$

Which is finally the *Markovian quantum master equation.*

1.3.4 | General form of the master equation

The Markovian quantum master equation can be further developed if the interaction is written by means of tensor products of operators $\hat{A}$ acting on the system and operators $\hat{B}$ acting on the bath:

$$\hat{V} = \sum_{\alpha} \hat{A}^{\alpha} \hat{B}^{\alpha}. \tag{1.86}$$

Using the matrix representation for the reduced density matrix,

$$\tilde{\rho}_{AA'}(t) = \langle A | \mathrm{Tr}_{\mathcal{B}} \tilde{\rho}(t) | A' \rangle = \sum_{B} \langle AB | \tilde{\rho}(t) | A'B \rangle, \tag{1.87}$$

the time evolution of the density matrix in the Schrödinger picture is given by

$$\begin{aligned}\frac{d\rho_{AA'}(t)}{dt} =& -i(E_A - E_{A'})\rho_{A,A'}(t) \\ &- \sum_{\alpha,\beta}\sum_{A_1,A_2} iA^{\alpha}_{AA_1}A^{\beta}_{A_1A_2}\rho_{A_2A'}(t)\langle B^{\alpha\beta}(E_{A_2} - E_{A_1} + i\eta)\rangle \\ &- \sum_{\alpha,\beta}\sum_{A_1,A_2} iA^{\beta}_{AA_1}\rho_{A_1A_2}(t)A^{\alpha}_{A_2A'}\langle B^{\alpha\beta}(E_{A_2} - E_{A'} - i\eta)\rangle \\ &+ \sum_{\alpha,\beta}\sum_{A_1,A_2} iA^{\beta}_{AA_1}\rho_{A_1A_2}(t)A^{\alpha}_{A_2A'}\langle B^{\alpha\beta}(E_{A_1} - E_A + i\eta)\rangle \\ &+ \sum_{\alpha,\beta}\sum_{A_1,A_2} i\rho_{AA_1}(t)A^{\alpha}_{A_1A_2}A^{\beta}_{A_2A'}\langle B^{\alpha\beta}(E_{A_1} - E_{A_2} - i\eta)\rangle,\end{aligned} \tag{1.88}$$

where we have defined the bath correlation function

$$\langle B^{\alpha\beta}(\omega)\rangle = \sum_{B,B_1}\frac{e^{-\beta E_B}}{Z_{\mathcal{B}}}\frac{B^{\alpha}_{BB_1}B^{\beta}_{B_1B}}{\omega + E_B - E_{B_1}} \tag{1.89}$$

$$= -\sum_{B,B_1}\frac{e^{-\beta E_B}}{Z_{\mathcal{B}}}\frac{B^{\alpha}_{BB_1}B^{\beta}_{B_1B}}{-\omega + E_{B_1} - E_B}. \tag{1.90}$$

Equation (1.88) is known as the master equation in Lindblad form or *Lindbladian*. An exhaustive derivation of this equation from the Markovian master equation can be found in Appendix B, together with an analytic analysis of this equation for some simple examples.

Chapter 2

Electron-phonon coupling of Fe adatom electron states on MgO/Ag(100)

Magnetic adatoms have shown to offer an exceptional base for making atomic-scale devices such as magnetic memories or quantum bits. The low coordination possessed by individual atoms deposited on surfaces preserves part of the orbital angular momentum along the perpendicular axis, while the in-plane orbital angular momentum is quenched. This gives rise to a large magnetic anisotropy energy (MAE) [56], which stabilizes their magnetic moment protecting it from fluctuations. However, duo to their atomic nature, a large variety of quantum effects are involved in their behavior.

Their magnetic structure has been widely characterized using experimental techniques such as inelastic electron tunneling spectroscopy [13, 20, 21, 25, 26, 28], X-ray magnetic circular dichroism [4, 9, 31, 32], or more recently by means of electron paramagnetic resonance [3, 34, 35, 40], which has improved the accessible energy resolution. The theoretical studies using model spin Hamiltonians [12, 44] or even *ab-initio* density-functional theory (DFT) [42, 45, 52] or multiplet calculations [54] has improved our understanding of their magnetic structure. Further studying how the adatoms interact with their environment has allowed a deeper understanding of the underlying physics. In particular, the influence of the substrate electronic states on the adatom has enabled the design of long-living magnetic quantum states. For that purpose, the MAE has

been increased by controlling the effect of the substrate crystal field on the electronic structure [2, 27, 88], and the interaction with the substrate electrons has been reduced by adding decoupling layer such as MgO or Cu_2N between the metallic substrate and the adatom [4, 21].

The large potential that magnetic adatoms have shown to engineer their coupling to the substrate has been possible thanks to a deep understanding of the involved interactions. While the electronic interactions has been widely studied during the last years [9, 17, 21, 26, 27, 31, 42, 46, 47, 54, 56, 88–92], the investigation of the effect of the electron-phonon interaction on the magnetic properties of adatoms has attracted much less attention. This has been so due to the challenge posed by the computation of the electron-phonon interaction on a super-cell system with a large number of atoms.

In this chapter we present a first principles characterization of the electron-phonon interaction on the electronic quasiparticle states of the Fe adatom on the MgO/Ag(100) surface. In Sec. 2.1, we introduce the theoretical framework used to analyze the effect of the electron-phonon coupling on the electronic states. Sec. 2.2 is dedicated to apply the presented formalism to the electronic states of the Fe adatom on MgO/Ag(100). In this regard, in Sec. 2.2.1 we provide the computational details of the first principles calculations. We next examine the electronic and vibrational structures of the MgO/Ag(100) substrate and the Fe adatom on Sec. 2.2.2, considering also the MgO layer dependence. We follow with the calculations and analysis of the electron-phonon coupling in Sec. 2.2.3. And finally, Sec. 2.3 summarizes the main results and conclusions.

2.1 | Electron-phonon interaction on electronic states

Starting from the Hamiltonian of the coupling between the electronic states and the nuclear motion presented in Sec. 1.1.5, here we follow the classical formalism developed in terms of many-body perturbation theory that has been successfully used for bulk materials as well as for surface states.

The matrix elements become relevant when studying this coupling perturbatively, which are given by Eq. (1.54). In the most general spin

non-collinear formalism, where the wave functions are spinors and the Kohn-Sham potential is a 2×2 matirx, the electron-phonon matrix elements are computed as

$$g^{\eta}_{\alpha\alpha'} = \sum_{s,s'} \frac{1}{\sqrt{2\omega_\eta}} \langle \psi^s_\alpha | \partial \hat{V}^{ss'}_\eta | \psi^{s'}_{\alpha'} \rangle = \sum_{s,s'} \sum_{I\kappa} \frac{\zeta^{I\kappa}_\eta}{\sqrt{2M_I\omega_\eta}} \langle \psi^s_\alpha | \partial \hat{V}^{ss'}_{I\kappa} | \psi^{s'}_{\alpha'} \rangle. \tag{2.1}$$

Above, s and s' indices represent the spin components of the Kohn-Sham potential.

The matrix element can be naturally divided into two pieces; the spin-diagonal ($s = s'$) and spin-flip ($s \neq s'$) parts. The former is mostly driven by the Hartree term and is therefore commonly regarded as the dominant contribution in most materials [69, 93]. The spin-flip part, in turn, originates from the relativistic spin-orbit interaction that scales as v^2/c^2, with v the electron velocity and c the speed of light.

Given their different nature, the spin-diagonal and spin-flip terms are expected to show marked differences in magnetic adatoms, *e.g.*, in their total strength as well as dependence on the insulating coverage. In this chapter we focus on the spin-diagonal electron-phonon contribution and present *ab-initio* calculations on a Fe adatom deposited on the MgO/Ag(100) surface. Therefore, the spin-diagonal electron-phonon matrix elements are computed as

$$g^{\eta}_{\alpha\alpha'} = \sum_{s,s'} \frac{\delta_{s,s'}}{\sqrt{2\omega_\eta}} \langle \psi^s_\alpha | \partial \hat{V}^{ss'}_\eta | \psi^{s'}_{\alpha'} \rangle. \tag{2.2}$$

Many-body perturbation theory is based on the Green's functions formalism, where the interaction is taken into account by means of the self-energy. The self-energy encodes all the information of the many-body effects and gives the Green's function of the interacting particles, called *quasiparticles*, by solving the Dyson equation. The many-body perturbation theory for coupled electrons and phonons is well established and the reader may refer to Refs. [67–69] for a more detailed theoretical development.

It can be shown that the electron-phonon self-energy can be written from the *state-dependent Eliashberg function* defined as

$$\alpha^2 F_i(\omega) = \sum_{\eta,f} \left| g^{\eta}_{if} \right|^2 \delta(\varepsilon_i - \varepsilon_f) \delta(\omega - \omega_\eta). \tag{2.3}$$

This quantity is widely used to study the electron-phonon interaction in metals [67, 68], and represents the scattering probability from an initial state with energy ε_i via a phonon of energy ω. This function enables us to identify the phonons that interact most prominently and, therefore, will be the fundamental quantity analyzed in this chapter.

The Eliashberg function also allows us to calculate the lifetime of excited single electron quasiparticles, integrating the scattering probabilities at all phonon energies,

$$\tau_i^{-1} = \Gamma_i = 2\pi \int_0^{\omega_{max}} \alpha^2 F_i(\omega) d\omega, \tag{2.4}$$

which resembles Fermi's Golden Rule. This lifetime should not be confused with the spin-flip lifetime measured experimentally, which is related to the a more complex collective behavior of all the electrons of the adatom.

The Eliashberg function also enables computing the dimensionless *mass enhancement parameter* λ for a given state i as

$$\lambda_i = 2 \int_0^{\omega_{max}} \frac{\alpha^2 F_i(\omega)}{\omega} d\omega. \tag{2.5}$$

In metals with full translational symmetry, this quantity describes the mass enhancement of electron quasiparticles at the Fermi level for low temperatures and is widely used to characterize the strength of the electron-phonon coupling. In the system that we are analyzing, as the most interesting electron states are localized around the iron adatom, we were forced to find another physical interpretation. In fact, it is easily shown that in this case the λ parameter describes the energy shift due to the electron-phonon interaction (see Appendix C),

$$\Delta\varepsilon \approx -\varepsilon_0 \lambda \left(\frac{\omega_0}{\varepsilon_0}\right)^2 \text{ for } |\varepsilon_0| \gg \omega_0, \tag{2.6}$$

and provides a feeling of the strength of the electron-phonon coupling. Above, ε_0 and ω_0 represent the unperturbed energy of the localized state and the energy of the localized vibrational mode, respectively.

2.2 | The Fe adatom on MgO/Ag(100)

After the first measurements of spin excitations on Mn adatoms adsorbed on a Al_2O_3/NiAl(110) surface [13], there have been many adatom

systems whose magnetic structures have been studied in great detail thanks to the development of experimental techniques such as inelastic electron tunneling spectroscopy [13, 20, 21, 25, 26, 28], X-ray magnetic circular dichroism [4, 9, 31, 32], spin-polarized scanning tunneling microscope [6, 8, 18, 23, 24] or electron paramagnetic resonance [3, 7, 40]. Moreover, a bunch of exhaustive theoretical studies have proven to provide accurate results in agreement with experimental results [2, 12, 42–48, 50–54, 61, 85, 89, 90]. In particular, DFT calculations have been widely used in order to explore the electronic structures of the adatom systems in detail.

Among the different systems studied, the Fe adatoms adsorbed on the MgO/Ag(100) surface stands out as a perfect candidate in which the effects of the electron-phonon coupling can be studied. It has been thoroughly characterized by means of both experimental and theoretical studies [3, 6, 30, 37, 38, 53–55, 85, 88], and, unlike the computationally more complex lantanide adatoms, it is an accessible system in order to compute the effect of the electron-phonon interaction.

2.2.1 | Computational details

The first principles calculations were preformed using the DFT formalism implemented in the SIESTA code [94], based on numerical linear combination of atomic orbitals (LCAO) basis sets and pseudopotentials (PPs) [95]. Optimized basis sets are used for silver and oxygen, a triple-zeta plus 2 polarization orbitals for magnesium and a triple-zeta plus 3 polarization orbitals for iron. Atomic cores are represented using separable [96] norm-conserving PPs [97]. The generalized gradient approximation parametrized by Perdew, Burke and Ernzerhof [98] (PBE-GGA) has been used for the exchange-correlation functional. The spin polarized calculations were done using the collinear formalism.

Calculations of the clean MgO/Ag(100) surface, are modeled using a slab system consisting of eleven silver atoms with a layer of magnesium oxide on both terminations. Coverages of MgO from 0 to 4 monolayers (MLs) are considered, with a minimum vacuum region of 18 Å to prevent interaction between slabs for 1 ML coverage. We also have considered the free standing 7 layer MgO surface on our calculations to disentangle the role of electronic interactions on the properties of the adatom. Additionally, the Fe adatom system calculations are preformed considering a

$4 \times 4 \times 1$ super-cell of the original MgO/Ag(100) surface, with the iron adatom on top of an oxygen site. This adds up to a total of 433 atoms for the 4 MgO layer adatom system calculations.

Integrations over the Brillouin zone are done using a $4 \times 4 \times 1$ Monkhorst-Pack mesh [99] for the clean MgO/Ag(100) slab, and the Γ point for the super-cell with the iron adatom. The occupations are calculated by the Fermi-Dirac distribution with an electronic temperature of 300 K to accelerate selfconsistency. Real space integrals are done using a mesh cutoff of 600 Ry for all calculations. Additionally, the `Grid.CellSampling` parameter has been used on the adatom system to mitigate the egg-box effect on atomic forces and properly determine the soft modes of the adatom.

Due to the large numbers of atoms present on the calculations, we have used the direct method with symmetries introduced on Sec. 1.1.4 to compute the lattice dynamics of a system. In general, in a system with N atoms, a naive implementation of the direct method would require $3 \times N$ standard self-consistent DFT calculations to compute the interatomic force constants. Therefore, a minimum of 1299 independent DFT calculations would be required in the case of the clean MgO/Ag(100) system with 4 MgO layers. However, making use of the P4/mmm space group symmetry of the system the complete interatomic force constants matrix can be computed from only 28 different DFT calculations.

Adding the iron adatom to the calculation breaks the translational and inversion symmetry of the system, while the 4-fold symmetry is still maintained. This means that one would be forced to consider hundreds of different self-consistent DFT calculations if the translational symmetry of the clean substrate was not exploited. However, as adding the adatom changes only the neighboring interatomic force constants and leaves most of the substrate unaltered, we reduced the number of DFT calculations by considering the interatomic force constants of the MgO/Ag(100) substrate without the adatom as an starting point. Then, we include the local modifications of the interatomic force constants due to the adatom by computing the interatomic force constants connected to the adatom and the oxygen underneath it. Thereby, only 32 independent DFT calculations are needed to completely determine the vibrational modes of the Fe adatom on a $4 \times 4 \times 1$ 4 ML MgO/Ag(100) super-cell. 28 for the substrate + 2 for the iron + 2 for the oxygen below it (note that the 4-fold symmetry makes the x and y Cartesian directions equivalent).

Following the approach of the direct method presented on Sec. 1.1.4, the potential induced by the atomic displacement $\mathbf{u}_I^\kappa$ is also computed by differentiating the Kohn-Sham potential (V_{KS}) by a centered finite differences formula:

$$\partial \hat{V}_{I\kappa}^{ss'} = \frac{\hat{V}_{\mathrm{KS}}^{ss'}(\mathbf{R} + \mathbf{u}_I^\kappa) - \hat{V}_{\mathrm{KS}}^{ss'}(\mathbf{R} - \mathbf{u}_I^\kappa)}{2u_I^\kappa}. \tag{2.7}$$

It is also important to note that, given that $\partial V_{I\kappa}$ is generally well localized around the displaced atom, the approach followed to compute the interatomic force constants in the adatom system can also be safely employed to compute the induced potentials.

Finally, the electron-phonon matrix elements (2.1) are computed in Fourier space as most of the state-of-the-art electron-phonon calculations do [69, 100, 101]. Therefore, being SIESTA a LCAO method, the wave functions have to be converted from the basis of atomic orbitals to a plane wave basis. For this purpose we follow the procedure presented on Appendix D.

2.2.2 | Electronic and vibrational properties

In this section we will describe the ground state properties of the Fe/MgO/Ag(100) system. We have chosen the Ag(100) surface covered with three MgO layers as the reference system analyzed in Secs. 2.2.2.1 and 2.2.2.2, given that it best exemplifies the central features of interest. The analysis of the MgO layer dependence is done in Sec. 2.2.2.3.

2.2.2.1 | Clean MgO/Ag(100) substrate

Figure 2.1 shows the electronic band structure of the MgO/Ag(100) surface for 3 ML of MgO. The projected density of states (PDOS) is shown in Figure 2.1b, where the electronic states of the MgO layer are below 2 eV from the Fermi level. Indeed, the meV energy window of phonon energies around the Fermi level is exclusively dominated by silver states. Focusing on the band structure in Figure 2.1a, the blue area represents the bulk band projection of the silver (100) surface. It is known from previous works that the Ag(100) surface hosts a surface state close to the Fermi energy

at the X point of the surface Brillouin zone [102–107]. Our calculation shows an electronic state localized on the MgO/Ag(100) interface with similar energy around the same region. As we will show, this interface state will play an important role in the conduction properties and on the electron-phonon coupling due to its energy and proximity to the surface.

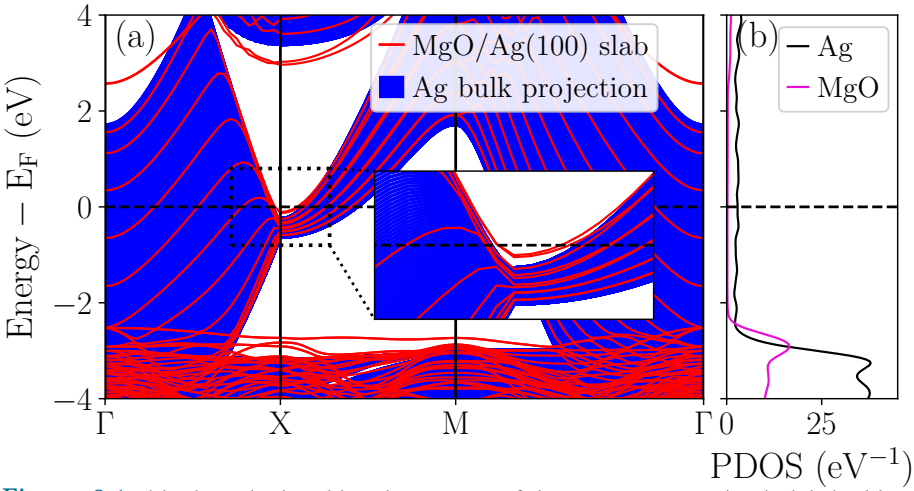

Figure 2.1: (a) The calculated band structure of the 3 ML MgO/Ag(100) slab (red lines) together with the bulk band projection of silver (solid blue). The inset shows the detail close to the Fermi energy of the interface state at the high symmetry X point. (b) The calculated projected DOS of the MgO layer and the Ag(100) substrate. The dashed line represents the Fermi level.

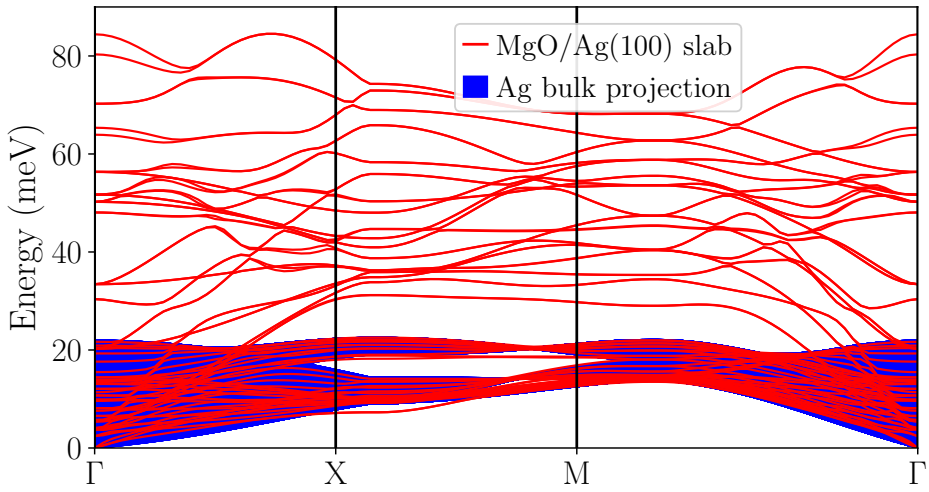

Figure 2.2: Calculated phonon dispersion of the 3 ML MgO/Ag(100) slab (red lines) and silver bulk phonon projection (solid blue).

In Figure 2.2 we present the calculated phonon dispersion of the

3 ML MgO/Ag(100) surface. The blue area represents the bulk phonon projection of the Ag(100) surface and the red lines show the calculated phonon dispersion of the MgO/Ag(100) slab, which is very similar to that of the clean Ag(100) surface at least up to 20 meV [108]. The higher energy modes correspond to vibrations of MgO. The first acoustic mode of the MgO layer is completely mixed with silver oscillations in the 10-20 meV energy range.

2.2.2.2 | Fe adatom

We analyze now the properties of the Fe adatom deposited on the $4 \times 4 \times 1$ 3 ML-MgO/Ag(100) super-cell. We found the oxygen top adsorption site to be energetically the most favorable one for iron, in agreement with previous studies [3, 6, 88]. After relaxation, the oxygen atom is slightly displaced upwards with a resulting Fe-O bond of 2.01 Å, in agreement with Ref. 88. The system develops a magnetic ground state, with a local magnetic moment of 3.97 μ_B for the iron adatom, and 0.1 μ_B spread over the surrounding atoms.

In Figure 2.3 we show the spin resolved PDOS projected on the Fe adatom. The occupation of the valence $3d$ electrons has a similar configuration to the free atom; the five majority states are filled, whereas only one minority orbital is fully occupied; note that the $3d_{z^2}$ is partially occupied because it is highly hybridized with the $4s$ orbital. The only orbital that falls in the meV range from the Fermi level is the minority $3d_{xy}$, which will therefore play a central role in the forthcoming analysis of the electron-phonon interaction.

Next we analyze the vibration modes of the 3 ML Fe-MgO/Ag(100) system. The phonon DOS projected on the iron adatom is shown in Figure 2.4. The figure reveals a vibrational mode completely localized in iron at 7.3 meV. Physically, this peak corresponds to two degenerate modes of the adatom oscillating parallel to the surface. At higher energies, in the 12-25 meV range, we observe the presence of multiple modes with an out-of-plane polarization and with a more pronounced mixing with the substrate, as inferred from the broadening of the peak.

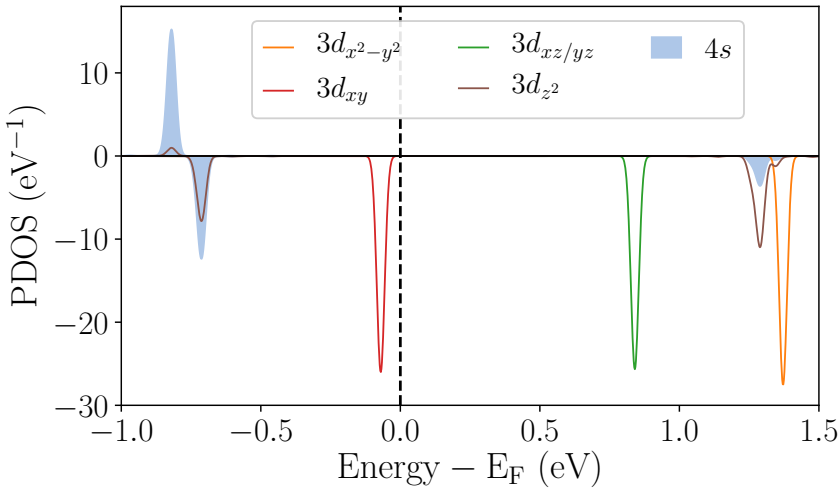

Figure 2.3: Projected DOS of iron's $3d$ (solid line) and $4s$ (solid background) orbitals for Fe on 3 ML MgO/Ag(100). Positive and negative values of the PDOS indicate majority and minority spin channels, respectively. The Fermi energy is marked by a vertical dashed line.

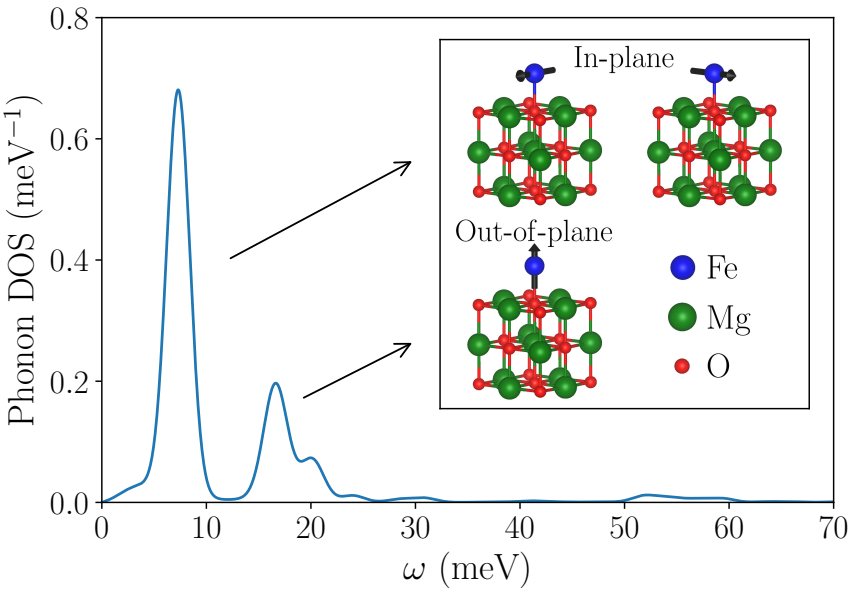

Figure 2.4: Phonon DOS projected onto the Fe adatom deposited on 3 ML MgO/Ag(100). The inset shows the MgO layers and the Fe adatom, with the arrows indicating the polarization vector of the vibrational modes localized on the adatom.

2.2.2.3 | Layer dependent electronic and vibrational properties

Here we study the influence of the number of MgO layers on the electronic and vibrational properties. As a general trend, increasing the MgO coverage has the effect of isolating the adatom from the interactions with electrons and phonons of the silver substrate. However, the trend is not monotonic due to a marked difference between the geometric configurations with even and odd number of MgO layers. Figure 2.5 shows schematically that when the number of MgO layers is odd, the adatom has an atom of the first silver layer underneath in the same vertical line, whereas it lies on over a hollow site of the Ag(100) surface termination when the number of MgO layers is even. This observation is crucial for understanding the electronic hybridization and the vibrational structure of the system for different coverages of MgO.

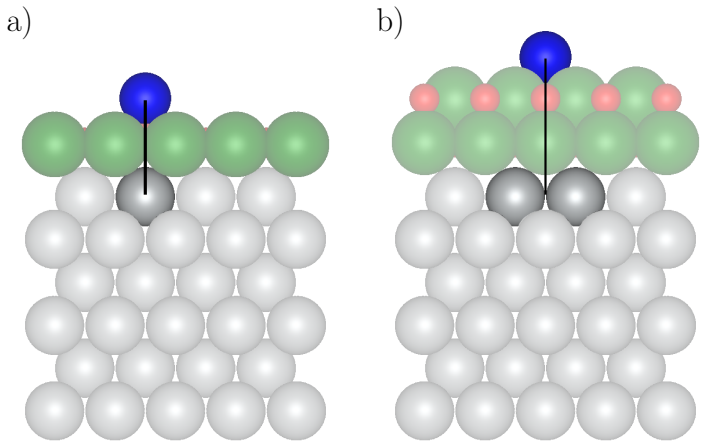

Figure 2.5: Positioning of the iron adatom respect to the Ag(100) substrate for an (a) odd and (b) even number of MgO layers. The vertical black line is a guide for the eye.

In Figure 2.6 we illustrate the electronic DOS projected on the minority spin channel of the iron adatom for coverages of MgO ranging from 0 to 4 MLs together with iron on free standing MgO. As a general trend we observe that the broadening of the peaks decreases when increasing the number of MgO layers. For the clean Ag(100) surface (0 ML), the iron projected states are completely broadened around the Fermi level, with no clear peak structure. Already for 1 ML coverage, the $3d_{xy}$ peak is localized close to E_F, and its width decreases with increasing coverage as a consequence of the insulating nature of MgO. For free standing MgO the

iron $3d$ states are located at slightly different energies, but the broadening of the peaks is very similar to the 4 ML MgO/Ag(100) system, indicating that the iron adatom is well protected from the silver substrate electrons with 4 ML of MgO.

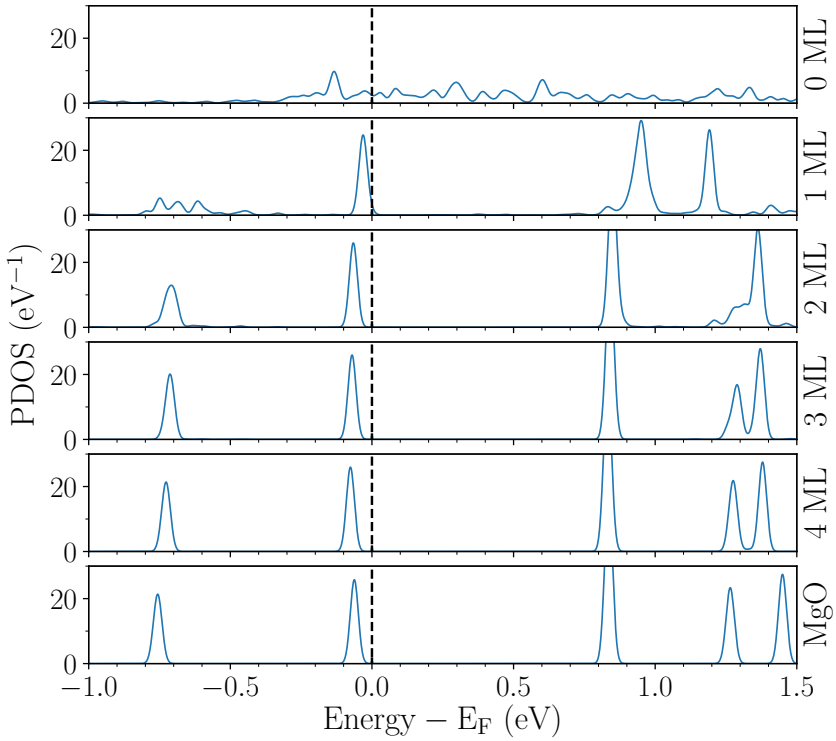

Figure 2.6: Calculated DOS of Fe-MgO/Ag(100) projected onto the iron adatom for different coverages of MgO and Fe on free standing MgO. The vertical dashed lines indicate the Fermi level.

An important contribution to the hybridization can be associated to the interface state discussed in Figure 2.1, since it lies close to the iron's $3d_{xy}$ state both in real space and in energy. This is made clear in Figure 2.7, where we show the isosurface of this interface state for different MgO coverages. For 1 ML of MgO, it is clear from Figure 2.7a that the interface state is mainly localized in the first three layers of silver, but it already shows a considerable hybridization with the iron adatom. For larger coverages of MgO, the hybridization is reduced considerably, as can be noted from the value of the isosurface used in order to make the hybridization visible. Another feature revealed by the figure is the different atomic nature of the hybridization depending on the MgO coverage. Due to the qualitative difference between odd and even configurations,

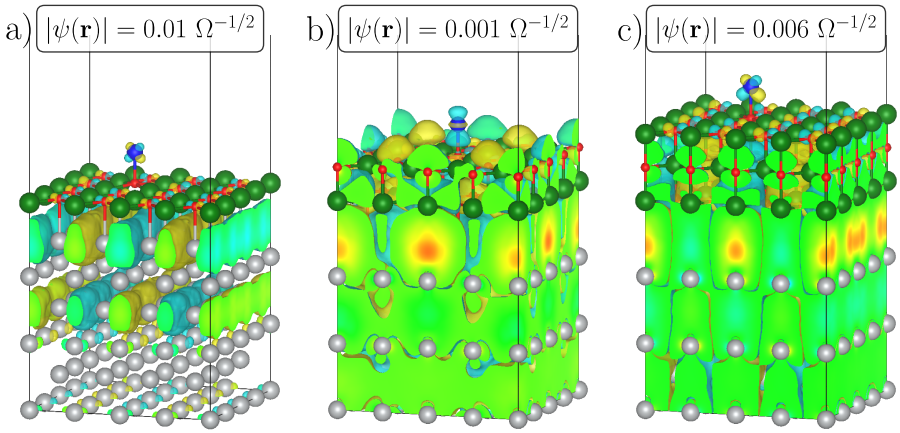

Figure 2.7: Isosurface of the interface state discussed in Figure 2.1 for different coverages of MgO: a) 1 ML, b) 2 ML and c) 3 ML. The value of the isosurface has been chosen to make visible the hybridization with the iron adatom. Ω is the volume of the unit cell.

the hybridized interface state has a $3d_{z^2}$ orbital character around the iron adatom for an even number of MgO layers, while for odd coverages the hybridization has a $3d_{xz/yz}$ orbital nature on the adatom.

Coming next to the vibrational structure, Figure 2.8 shows the phonon DOS projected on the adatom for different number of MgO layers. For the system with the iron adatom adsorbed on the clean Ag(100) surface (0 ML), the figure shows that the energy of all vibrational modes is increased compared to coverages $\geq$ 1 ML. In the clean substrate the adatom is adsorbed on a hollow site and, thus, it is integrated more compactly into the surface, shifting up the energy of the modes due to the stronger interaction with the neighboring atoms. When adding MgO for coverages $\geq$ 2 ML, the largest contribution to the phonon DOS of iron comes from the in-plane modes located approximately at the same energy of around 7.3 meV. In the specific case of a single layer of MgO, the proximity of the silver substrate affects considerably the energy of the localized modes of the iron adatom, softening the energy of the in-plane mode to $\approx$ 3.2 meV. On the other hand, our calculations for Fe on free standing MgO show that the in-plane mode energy is approximately at 7 meV, with a phonon DOS practically equal to the 4 ML MgO/Ag(100) system. This indicates that the vibrational structure will remain unaltered for larger MgO coverages. Incidentally, we note that the energy of the in-plane mode of a Ho adatom in free standing MgO was found at 4.7 meV [62]; the ratio between the two energy modes is described reasonably well by the mass ratio of the two adatoms, $\sqrt{M_{\mathrm{Fe}}/M_{\mathrm{Ho}}}$. Finally, Figure 2.8 shows that the out-of plane

modes, located between 10 to 20 meV, are hardened by increasing the MgO coverage, the reason being that MgO vibrationenergies are about 4 times more energetic than in silver.

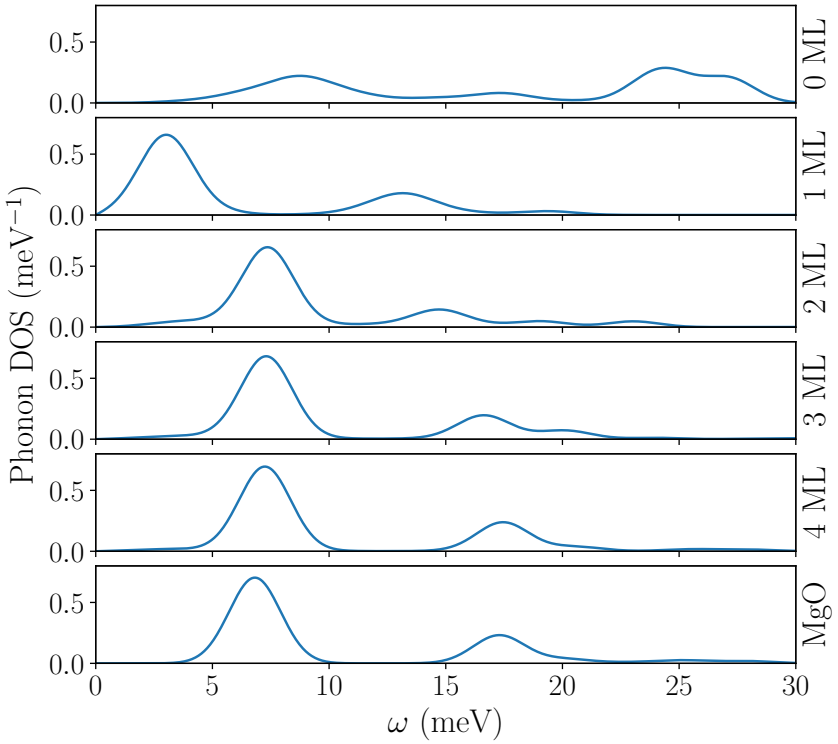

Figure 2.8: The calculated phonon DOS projected onto the Fe adatom deposited on MgO/Ag(100) with coverages ranging from 0 ML (bare silver surface) to 4 ML of MgO and Fe on free standing MgO.

2.2.3 | Electron-phonon coupling

Having analyzed all the ingredients needed to compute the electron-phonon matrix elements, in this section we study the effect of the electron-phonon interaction on the one-particle states of the system. The size of the electron-phonon interaction is determined by the scattering matrix elements defined in Eqs. (2.1) and (2.2). Those expressions show that the strength of the electron-phonon interaction depends on the overlap between three quantities: initial and final electronic states, and the potential induced by the phonon. Given that the electron-phonon interaction influences the electronic properties mostly on a energy window on the scale of meV around the Fermi level, the effect on the adatom will be dominated

by the $3d_{xy}$ spin-down state. For this reason, and given that the initial $3d_{xy}$ state is localized on the adatom and the only energetically available final states are on the silver substrate, the larger the hybridization of silver states with iron, the larger the electron-phonon scattering matrix elements will be. Furthermore, the vibrational modes that involve the atoms around iron will also be crucial due to the overlap of the potential induced by this phonons with the initial $3d_{xy}$ state.

2.2.3.1 | ELIASHBERG FUNCTION

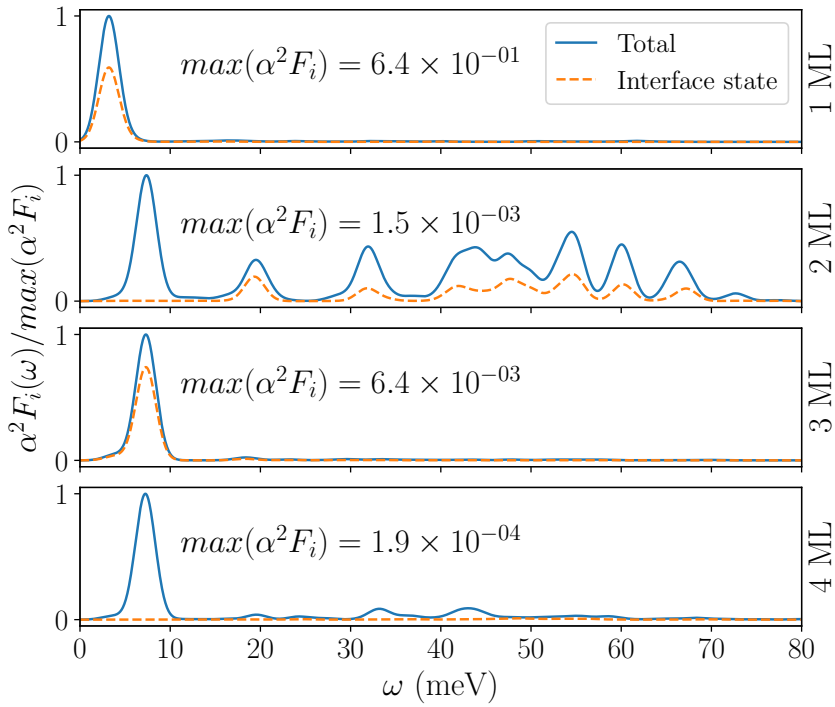

Figure 2.9: Calculated Eliashberg function of the initial $3d_{xy}$ state of the iron adatom on MgO/Ag(100) for MgO coverages from 1 ML to 4 ML. The solid blue line represents the total scattering probability, while the dashed orange line includes scattering only through the interface state.

Figure 2.9 shows our calculated Eliashberg function for the $3d_{xy}$ state of the adatom on the MgO/Ag(100) surface, for MgO coverages ranging from 1 ML to 4 ML. We have not included free standing MgO since the initial $3d_{xy}$ state does not have available final states to scatter to due to the energy gap of MgO around the Fermi level. The Eliashberg function is largely dominated by a strong peak located between 3 and 8 meV

depending on the coverage, which coincides with the energy of the in-plane phonon modes localized in iron (see Figure 2.8). The importance of local in-plane modes revealed by these results is consistent with what was found by Donati *et al.* [62] in a similar system.

Noteworthily, our calculations reveal that for odd coverages of MgO, the main scattering channel is the interface state shown in Figure 2.7, whose contribution to the Eliashberg function represents as much as the 70% in the case of 3 ML coverage. For 1 ML, the proximity of the adatom to the silver substrate opens new scattering channels to the bulk silver states, reducing the contribution of the interface state to a 50% of the total electron-phonon scattering rate. On the other hand, the different atomic nature of the interface state around the adatom for even and odd coverages of MgO (see Figure 2.7) strongly suppresses scattering to the interface state for an even number of MgO layers, reducing significantly the strong peak observed for an odd coverage of MgO. This makes the contribution of high energy MgO phonons comparable to the contribution of the in-plane modes.

2.2.3.2 | λ parameter and quasiparticle lifetime

The calculated λ parameter of the localized iron $3d_{xy}$ state is shown in Figure 2.10 for the different MgO coverages; in order to have a comparative indication of the strength of the coupling we have also included the λ parameter of bulk Pb, which ranks among the strongest ever reported with $\lambda = 1.56$ [109], whereas on noble metal surfaces it can vary on the range $0.11 - 0.01$ [110]. We observe a clear step between 1 ML and 2 ML coverages. In fact, for ≤ 1 ML coverages, the strength of the electron-phonon interaction is quantitatively close to the one found for bulk Pb, which from Eq. (2.6) gives a positive energy shift of around 10% for the $3d_{xy}$ state. We find that for larger coverages, the λ parameter shows a reduction of two orders of magnitude, indicating that the $3d_{xy}$ orbital becomes effectively protected from the electron-phonon interaction. Clearly, our analysis indicates that a single MgO layer is not enough to screen or decouple the electronic states of the iron adatom from the silver substrate. Interestingly, the lifetime of the magnetic moment of Fe on MgO/Ag(100) has never been reported for coverages smaller than 2 MgO layers. While a single monolayer of MgO on Ag(100) occurs infrequently in experiment [6], this coincidence might also suggests that an effective screening of the electron-phonon coupling is an important ingredient for

achieving magnetic stability of single adatoms.

Additionally, we observe that the layer dependence of the λ parameter follows a clear odd-even step structure, whereas it decreases if we do not consider scattering through the interface state (see dashed line in Figure 2.10). Thus, the interface state is the main responsible of the step structure, which is consistent with our analysis of the geometric configuration in terms of the number of MgO layers and the connection with the hybridization of the interface state.

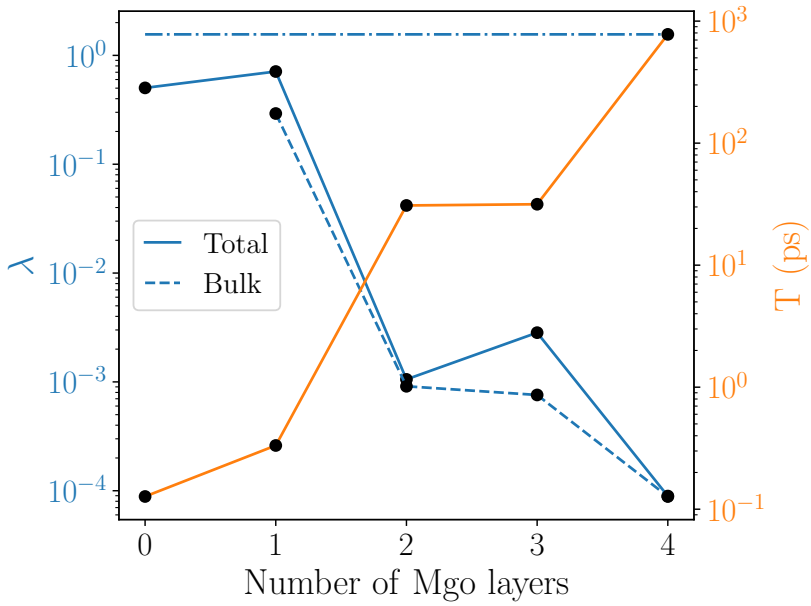

Figure 2.10: Calculated electron-phonon λ parameter (left axis) and electron-phonon lifetime of a one-particle excitation (right axis) for the $3d_{xy}$ orbital of the iron adatom deposited on MgO/Ag(100) as a function of the MgO coverage. The dashed line represents the λ parameter for scattering through silver bulk states, whereas the solid line represents the total λ parameter (silver bulk plus interface state scattering channels). The dash-dotted line indicates the λ parameter of bulk Pb, a material with strong electron-phonon coupling.

Figure 2.10 shows our calculated lifetime for a hole on the $3d_{xy}$ orbital of the adatom as a function of MgO layers. For 0 ML and 1 ML coverages, the lifetime of the quasiparticle is of the order of 0.1 ps, whereas we obtain a lifetime of around 30 ps for 2 and 3 ML coverages and of 800 ps for 4 MLs. Again, we observe a clear step structure, with a jump of two orders of magnitude from 1 ML to 2 ML coverage, which is also caused by the absence of the interface state scattering channel for an even number of MgO layers.

2.3 | Summary and outlook

In this chapter, we have conducted a detailed *ab-initio* analysis of the spin-diagonal electron-phonon interaction of an iron adatom on the MgO/Ag(100) surface. In Sec. 2.2.2 we have calculated the electronic and vibrational structures of the adatom and the substrate, pointing out the importance of the silver substrate providing final states to scatter on the electron-phonon interaction. We have computed the strength of the electron-phonon coupling in Sec. 2.2.3. Using the Eliashberg function we have demonstrated that the in-plane oscillations of the adatom are the most important vibrational modes, which is in good agreement with what was found in Ho on MgO/Ag(100) [62]. Moreover, the calculated λ parameter and quasiparticle lifetime show qualitative differences on the electron-phonon interaction strength for even and odd number of MgO layers. This difference between even and odd coverages is explained by the presence of an interface state of the substrate close to the high symmetry point X, which represents the most important scattering channel for odd coverages of MgO; its contribution represents up to 70% of the total scattering rate in the case of 3 ML coverage, whereas for an even number of MgO layers its contribution is highly suppressed. Finally, as a central result, we have shown that a single MgO layer is not capable of effectively screening the spin-diagonal electron-phonon interaction on the iron adatom, whose calculated strength is comparable to the largest values found among bulk materials. In turn, our calculations show that electron-phonon scattering is deeply suppressed for two or more layers of MgO.

Chapter 3

Spin-relaxation of a single Fe adatom coupled to vibrations

In the same context as in the previous Chapter, where magnetic adatoms offer an exceptional scenario to study spin dynamics and relaxation, further understanding how adatoms interact with their environment is essential to improve their control and manipulation techniques for applications such as quantum computing or magnetic storage devices.

With the growth of inelastic electron tunneling spectroscopy [13], successful theoretical models have been proposed to capture the essential physics behind experiments [43, 44]. The subsequent emergence of electron spin resonance combined with scanning tunneling spectroscopy has allowed remarkable results providing a boost on energy and spatial resolution [3, 7, 10, 34–37]. However, the physical origin of the resonant transitions is still unclear, even after several theoretical models have been proposed [38, 41, 53]. In the case of the long living magnetic states found in adatoms such as Ho or Fe on MgO/Ag(100) [4, 6, 8], interactions with the environment are believed to destabilize the magnetic moments by inducing transitions between the different spin states. However, the difficulty of performing first-principles calculations of spin lifetimes and transition rates complicates verifying the origin of the transition mechanisms involved on experimental measurements.

The effects of electronic interactions on adatom properties have been extensively studied with the help of the first principles schemes [5, 25, 44–52, 54], but much less attention has been paid to the interaction with substrate vibrations, i.e. phonons. Nevertheless, it has been speculated

many times about the role of spin-phonon coupling as a spin-relaxation mechanism in single adatoms. In particular, it is believed that it plays a key role, limiting the spin-lifetime, when the interaction with substrate conduction electrons is reduced by making use of insulating decoupling layers, such as Cu_2N or MgO [4, 21]. In the related field of molecular magnets, *ab-initio* calculations of the spin-phonon coupling have a long track record [70–77]. However, in the case of adatoms on surfaces, a convincing theoretical approach has been so far inaccessible due to the computational challenge posed by the many-body character of the problem and the huge number of atoms in a surface simulation.

In this chapter we present a method that combines first-principles density functional theory (DFT) calculations with an atomic multiplet model for accessing the electron-phonon spin relaxation time of a single Fe atom on MgO/Ag(100). Sec. 3.1 is dedicated to introduce the method, and we provide the derivation of the master equation that gives access to the spin relaxation time. In Sec. 3.2 we apply the presented formalism to study the spin-flip lifetime of the Fe adatom on MgO/Ag(100). For this, we first provide the computational details of the first principles calculations in Sec. 3.2.1. We next analyze the electronic and vibrational structures of the adatom on Sec. 3.2.2. In particular, Sec. 3.2.2.1 presents the DFT electronic and vibrational structures, and Sec. 3.2.2.2 shows the multiplet Stevens Hamiltonian. We follow with the calculations and analysis of the spin-flip lifetime of the Fe adatom in Sec. 3.2.3. Finally, Sec. 3.3 summarizes the main results and conclusions.

3.1 | Electron-phonon coupling on spin relaxation

In Chapter 2 we studied the effect of the electron-phonon interaction on the one-electron Kohn-Sham states. However, in order to describe the spin relaxation measured in experiments, the multiplet character of the magnetic states of the adatom has to be taken into account. Figure 3.1 shows a typical energy diagram of a magnetic adatom, where two possible relaxation mechanisms from the first excited state to the ground state have been indicated. $|\Psi_i\rangle$ denote the multiplet wave function of each magnetic state, which, in essence, are a linear combination of Slater determinants of the one-electron atomic orbitals of the adatom.

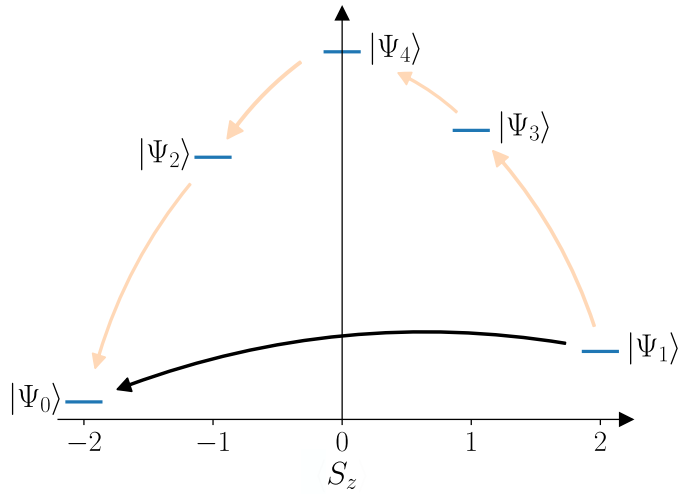

Figure 3.1: Schematic representation of th energy level diagram of a spin-2 adatom. The solid black arrow indicates the first order or direct transition from one spin state to the other. The blurry arrows represent a cascade-like mechanism, where the spin-flip transition is realized in a step-by-step process with smallest possible change in ΔM_S.

In the basis of one-electron atomic orbitals $|\psi_i\rangle$ with quantum numbers $i = \{n, l, m, \sigma\}$ (n is the principal quantum number, l the angular momentum, m its projection and σ the spin), the coupling between electrons and phonons is described by (See Sec. 1.1.5),

$$\hat{H}_{\text{el.}-\text{ph.}} = \sum_{\eta} \hat{H}^{\eta}_{\text{el.}-\text{ph.}} = \sum_{i,f,\eta} g^{\eta}_{if}\, c^{\dagger}_{f} c_i\, (b^{\dagger}_{\eta} + b_{\eta}). \tag{3.1}$$

Above, the electron-phonon matrix element g^{η}_{if} determines the probability amplitude of an atomic state $|\psi_i\rangle$ to be scattered to a state $|\psi_f\rangle$ by the emission or absorption of a phonon η. $c^{\dagger}$ and c ($b^{\dagger}$ and b) are the electron (phonon) creation and annihilation operators, respectively. In reality, the atomic orbitals are hybridized with the substrate and lose spherical symmetry. Even so, it is very useful to keep the associated quantum numbers to be able to perform multiplet calculations with total angular momentum.

To take hybridization into account, we define new atomic orbitals $|\tilde{\psi}_i\rangle$ by projection of the DFT spinor wave functions $|\psi^{\text{DFT}}_n\rangle$,

$$|\tilde{\psi}_i\rangle = \sum_{n} |\psi^{\text{DFT}}_n\rangle \, \langle \psi^{\text{DFT}}_n | \psi_i \rangle \,, \tag{3.2}$$

where we have limited the summation to an energy window equal to the broadening of each orbital on the DFT calculation. In this way, the electron-phonon matrix elements between the one-electron atomic orbitals are approximated by

$$g_{if}^{\eta} = \sum_{s,s'} \frac{1}{\sqrt{2\omega_\eta}} \langle \tilde{\psi}_i^s | \partial \hat{V}_\eta^{ss'} | \tilde{\psi}_f^{s'} \rangle = \sum_{s,s'} \sum_{I\kappa} \frac{\zeta_\eta^{I\kappa}}{\sqrt{2M_I\omega_\eta}} \langle \tilde{\psi}_i^s | \partial \hat{V}_{I\kappa}^{ss'} | \tilde{\psi}_f^{s'} \rangle. \tag{3.3}$$

Note that by computing the matrix elements in this way we are able to capture the effect of the hybridization between the iron and the substrate, which can vary for different substrates. Using this scheme, the adatom's wave functions are more delocalized than the pure atomic orbitals, and therefore, the electron-phonon coupling in the substrate area is also accounted.

However, in order to incorporate the many-body nature of the magnetic states, we need an approximation for the matrix elements between multiplet states, $G_{if}^{\eta} = \langle \Psi_i | \hat{H}_{el.-ph.}^{\eta} | \Psi_f \rangle$, with the notation of lower case letters for one-electron states and capital letters for multiplets. We calculated these matrix elements by employing the *ab-initio* matrix elements for one-electron states $|\tilde{\psi}_i\rangle$ and contracting the creation and annihilation operators of $\hat{H}_{el.-ph.}$ in Eq. 3.1 and the second quantization representation of the multiplet wave functions Ψ_i. See Appendix E for more details about the second quantization representation of the multiplet wave functions.

Finally, the fundamental Hamiltonian describing the magnetic states of an adatom and the phonon bath coupled with each other, can be defined as,

$$\hat{H} = \sum_i E_i C_i^\dagger C_i + \sum_\eta \omega_\eta b_\eta^\dagger b_\eta + \sum_{i,f,\eta} G_{if}^{\eta}\, C_f^\dagger C_i\, (b_\eta^\dagger + b_\eta). \tag{3.4}$$

The first term describes the electronic structure of the adatom, with eigenvalues E_i. The second term describes the unperturbed phonon system, where ω_η are the frequencies of the lattice vibrations. And, the third term describes the coupling between electrons and phonons, where G_{if}^{η} are the electron-phonon matrix elements between the adatom multiplet states.

The dynamics of the adatom coupled with the phonon bath, represented by Eq. (3.4), can be described by a master equation within the open quantum system formalism introduced in Sec. 1.3. In pump probe experiments performed to measure spin-flip lifetimes, an excited state of

the adatom is populated by a pump pulse, and then the evolution towards the ground state is measured with probe pulses. In the density matrix formalism, the evolution of the occupations of the electronic states of the adatom is given by the diagonal elements of the reduced density matrix of the adatom. Therefore, using the Born-Markov master equation given in Eq. 1.88 we obtain the rate equation for the diagonal elements of the density matrix of the adatom:

$$\begin{aligned}\frac{d\rho_{ii}(t)}{dt} = &+2\pi \sum_{j,\eta} |G^{\eta}_{ij}|^2 \rho_{jj}(t) \times \Big[n^{\eta}_{BE} \delta(E_j - E_i + \omega_\eta) \\ &\qquad + (n^{\eta}_{BE} + 1)\delta(E_j - E_i - \omega_\eta) \Big] \\ &-2\pi \sum_{j,\eta} |G^{\eta}_{ij}|^2 \rho_{ii}(t) \times \Big[n^{\eta}_{BE} \delta(E_i - E_j + \omega_\eta) \\ &\qquad + (n^{\eta}_{BE} + 1)\delta(E_i - E_j - \omega_\eta) \Big]. \end{aligned} \tag{3.5}$$

Here n^{η}_{BE} represents the thermal occupation of a phonon ω_η given by the Bose–Einstein distribution function.

For low temperatures considered in the experimental setup ($k_B T \approx 0.1$ meV), it is a safe assumption to consider only the direct transition marked with a black arrow on Figure 3.1 from the first excited state to the ground state. In this situation, with $E_i - E_f = \Delta E > 0$:

$$\begin{aligned}\frac{d\rho_{11}(t)}{dt} = &+ 2\pi\rho_{00}(t) \sum_{\nu} |g^{\nu}_{1,0}|^2 n_{BE}(\omega_\nu)\delta(\Delta E - \omega_\nu) \\ &- 2\pi\rho_{11}(t) \sum_{\nu} |g^{\nu}_{1.0}|^2 (n_{BE}(\omega_\nu) + 1)\delta(\Delta E - \omega_\nu), \end{aligned} \tag{3.6}$$

and

$$\begin{aligned}\frac{d\rho_{00}(t)}{dt} = &+ 2\pi\rho_{11}(t) \sum_{\nu} |g^{\nu}_{1,0}|^2 (n_{BE}(\omega_\nu) + 1)\delta(\Delta E - \omega_\nu) \\ &- 2\pi\rho_{00}(t) \sum_{\nu} |g^{\nu}_{1,0}|^2 n_{BE}(\omega_\nu)\delta(\Delta E - \omega_\nu). \end{aligned} \tag{3.7}$$

Therefore, using a matrix notation,

$$\begin{pmatrix} d\rho_{11}/dt \\ d\rho_{00}/dt \end{pmatrix} = \begin{pmatrix} -(\Gamma_0 + \Gamma_T) & +\Gamma_T \\ +(\Gamma_0 + \Gamma_T) & -\Gamma_T \end{pmatrix} \cdot \begin{pmatrix} \rho_{11} \\ \rho_{00} \end{pmatrix}, \tag{3.8}$$

where we have defined the temperature independent rate

$$\Gamma_0 = 2\pi \sum_\eta |G^\eta_{1,0}|^2 \delta(\Delta E - \omega_\eta), \tag{3.9}$$

and the temperature dependent rate

$$\Gamma_T = 2\pi \sum_\eta |G^\eta_{1,0}|^2 n^\eta_{BE} \delta(\Delta E - \omega_\eta). \tag{3.10}$$

This set of coupled differential equations has a simple solution in the basis of eigenvectors that diagonalizes the matrix above:

$$\begin{pmatrix} \rho_{11}(t) \\ \rho_{00}(t) \end{pmatrix} = C_1 \begin{pmatrix} \Gamma_T/(\Gamma_0 + \Gamma_T) \\ 1 \end{pmatrix} + C_2 \begin{pmatrix} 1 \\ -1 \end{pmatrix} e^{-(\Gamma_0 + 2\Gamma_T)t}. \tag{3.11}$$

Where C_1 and C_2 are constants to be determined by the initial conditions of the system. If the adatom is prepared to be in the excited state Ψ_1, then $\rho_{11}(0) = 1$ and $\rho_{00}(0) = 0$, thus the evolution of the density matrix is given by

$$\rho_{11}(t) = \frac{\Gamma_T}{\Gamma_0 + 2\Gamma_T} + \frac{\Gamma_0 + \Gamma_T}{\Gamma_0 + 2\Gamma_T} e^{-(\Gamma_0 + 2\Gamma_T)t}, \tag{3.12}$$

and

$$\rho_{00}(t) = \frac{\Gamma_0 + \Gamma_T}{\Gamma_0 + 2\Gamma_T} - \frac{\Gamma_0 + \Gamma_T}{\Gamma_0 + 2\Gamma_T} e^{-(\Gamma_0 + 2\Gamma_T)t}. \tag{3.13}$$

Thus, the Fermi's Golden Rule rate equation for the direct transition can be inferred from these equations:

$$\Gamma_{1\to 0} = \Gamma_0 + 2\Gamma_T = 2\pi \sum_\eta |G^\eta_{1,0}|^2 \left[2n_{BE}(\omega_\eta) + 1\right] \delta(E_1 - E_0 - \omega_\eta). \tag{3.14}$$

While Eq. (3.4) comprises all the needed information about the system in a simple and concise form, the real difficulty lies on obtaining all the parameters for an accurate description of the system. In this respect, we have used DFT calculations to compute the one-electron electronic structure and the vibrational properties of the system by means of the direct method presented in Chapter 1. The one-electron electron-phonon matrix elements are then computed with the procedure explained above.

However, given that DFT is a ground state method, and furthermore, it adopts a one-electron picture with a single Slater determinant wave function, it usually fails predicting the magnetic structure of adatoms. Therefore, we have considered a Stevens Hamiltonian in order to capture the many-body character of the adatom, and in this way properly describe the low energy spectrum of the adatom on the meV range and the corresponding multiplet wave functions. Finally, the matrix elements between multiplet states have been calculated mixing the one-electron matrix elements obtained from the DFT calculations and the multiplet wave functions obtained form the Stevens Hamiltonian.

3.2 | The Fe adatom on MgO/Ag(100)

Among all the different adatom systems, the Fe adatom on top of a MgO/Ag(100) surface has been one of the most studied systems [3, 6, 30, 37, 38, 53–55, 85, 88]. It possess a long spin relaxation time of the order of milliseconds, which makes it a very interesting system to study the spin dynamics on adatoms. Additionally, it has been shown that the spin-lifetime of this system is limited by non-electronic contributions [6], which makes Fe on MgO/Ag(100) a perfect benchmark system to study the effect of the coupling with phonons.

3.2.1 | Computational details

Most of the computational details used for the DFT calculations preformed in this Chapter are the same as in the previous one, therefore, the reader is referred to Sec. 2.2.1 for all the details. As the main difference, in this Chapter we have used spin non-collinear calculations to include the spin-orbit interaction. The calculations have been done using the off-site formalism for the spin-orbit coupling implemented in SIESTA [94, 111]. Spin-orbit interaction allows transitions between the one-electron states with different spin component, and thus, it is very important to describe the spin-flip relaxation mechanism.

Most of the computational details used for the DFT calculations preformed in this Chapter are the same as in the previous one, therefore, the reader is referred to Sec. 2.2.1 for all the details. As the main difference, in this Chapter we have used spin non-collinear calculations to include the

spin-orbit interaction. The calculations have been done using the off-site formalism for the spin-orbit coupling implemented in SIESTA [94, 111].

3.2.2 | Electronic and vibrational properties

In this section we describe the ground state properties of Fe on MgO/Ag(100). We analyze the DFT calculations in Sec. 3.2.2.1, i.e., the one-electron electronic structure and the vibrational structure of the adatom. Sec. 3.2.2.2 is devoted to study the low energy spectrum obtained by the Stevens Hamiltonian.

3.2.2.1 | DFT calculations

In general, since iron is a $3d$ transition metal, adding spin-orbit coupling to the calculations doesn't change significantly the electronic and vibrational structures of the adatom. And, in fact, the results obtained here are very similar to the ones presented in Sec. 2.2.2 of the previous Chapter.

The spin-orbit DFT calculations predict a magnetic ground state with a total magnetic moment of $4.06\,\mu_B$, of which $3.97\,\mu_B$ is localized on the iron adatom. It is formed by the Fe $3d$ orbitals, of which 5 majority spin and 1 minority spin are occupied. Figure 3.2 illustrates this with the spin-resolved projected density of states (PDOS) of the Fe adatom. The results for different MgO coverages are similar, the major difference being a larger hybridization in the case of 2 MgO layers, mostly in the spin majority $3d_{xy}$ and $3d_{z^2}$ orbitals.

Coming next to the vibrational modes of Fe, Figure 3.3 shows the phonon DOS projected on the iron adatom. The figure reveals a vibrational mode completely localized in iron at $7.3\,\mathrm{meV}$, which corresponds to a double degenerate in-plane oscillation of the adatom with respect to the MgO surface. At higher energies, in the $12\,\mathrm{meV}$ to $25\,\mathrm{meV}$ range, the multiple modes observed are related with an out-of-plane polarization of the adatom. These modes show a more pronounced mixing with the substrate, as can be appreciated from the broadening of the peak, specially for a 2 ML coverage of MgO.

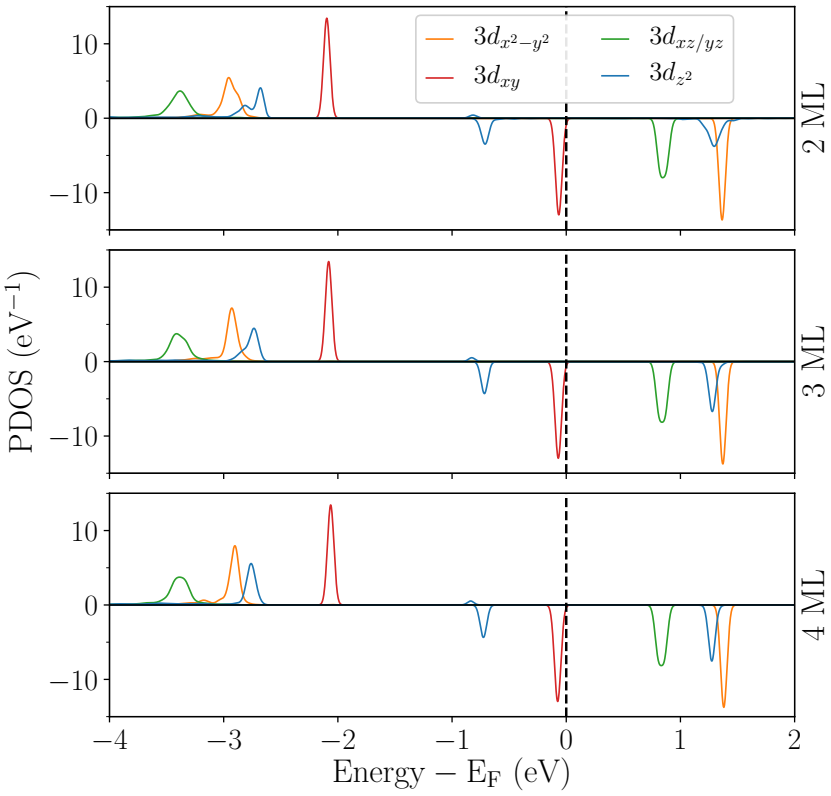

Figure 3.2: Projected DOS of iron's $3d$ orbitals for Fe on 3 ML MgO/Ag(100). Positive and negative values of the PDOS indicate majority and minority spin channels, respectively. The Fermi energy is marked by a vertical dashed line.

3.2.2.2 | STEVENS HAMILTONIAN

In order to incorporate the many-body nature of the adatom [54], we now consider a multiplet Hamiltonian in terms of fixed total spin (**S**) and total orbital angular momentum (**L**) operators. Starting from the ^5D term of an isolated iron atom with a d^6 configuration, the lowest energy term according to Hund's rules, the crystal field of the substrate can be expanded using Stevens operators $\hat{O}_n^m(\mathbf{L})$. In the case of Fe on top of an O atom of MgO, it is known that the low energy levels are well described by,

$$H = B_2^0\hat{O}_2^0 + B_4^0\hat{O}_4^0 + B_4^4\hat{O}_4^4 + \lambda\mathbf{L}\cdot\mathbf{S} + \mu_B\left(\mathbf{L}+2\mathbf{S}\right)\cdot\mathbf{B}, \qquad (3.15)$$

where $B_2^0 = -317.43\,\text{meV}$, $B_4^0 = -6.58\,\text{meV}$, $B_4^4 = -4.36\,\text{meV}$ and $\lambda = -12.6\,\text{meV}$ were obtained from a point charge model [86]. The first two terms compose the Axial Crystal Field (ACF) and the third one the

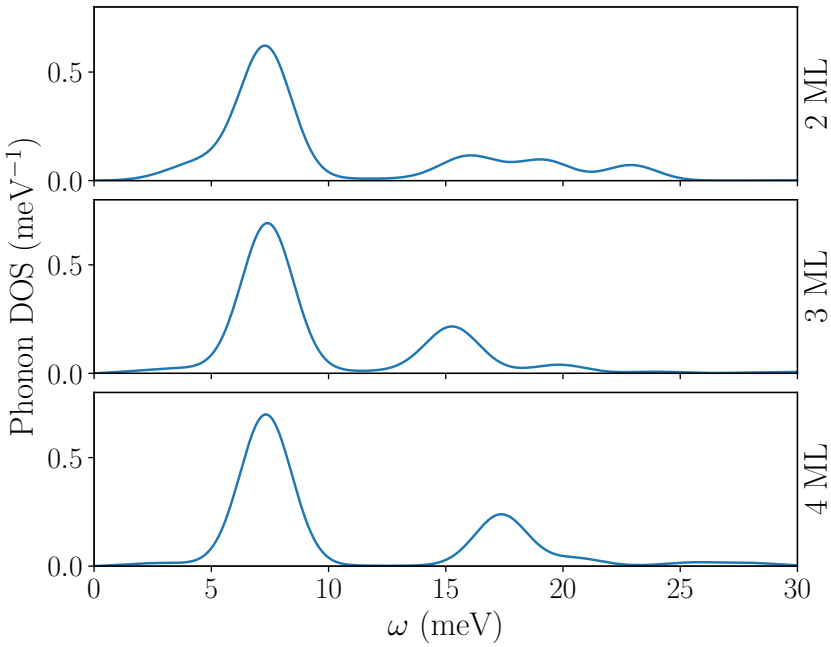

Figure 3.3: Phonon DOS projected onto the Fe adatom deposited on MgO/Ag(100) for 2 to 4 MLs of MgO.

Transverse Crystal Field (TCF). The fourth term describes the spin-orbit coupling with interaction strength λ and the last one accounts for the Zeeman term, with μ_B the Bohr magneton and **B** the magnetic field.

Direct diagonalization of the Hamiltonian 3.15 using the product basis of projections of total spin M_S and orbital angular momenta M_L, $\{|M_S, M_L\rangle\}$, gives access to the energy level spectrum and multiplet wave functions of the adatom. Figure 3.4 shows the low energy diagram for $B_z = 5\,\mathrm{T}$, which shows the usual parabolic shape found in experiments [6]. The zero field splitting (ZFS) indicated in the figure is of $14.38\,\mathrm{meV}$, which is in good agreement with experimental measurements [6, 88]. The magnetic anisotropy (MAE), also indicated in the figure, is of $20.06\,\mathrm{meV}$.

Figure 3.5 shows the evolution of the multiplet-state energies under the action of each term of the Hamiltonian. The ACF produces by far the biggest energy splitting, as can be inferred from the value of B_2^0. The lowest energy subspace consists of ten degenerate $M_L = \pm 2$ states. The TCF mixes states with $\Delta M_L = \pm 4$, producing two spin quintuplets with fully quenched orbital moments. The spin-orbit coupling breaks the degeneracy of the lowest energy subspace, and it is the ultimate

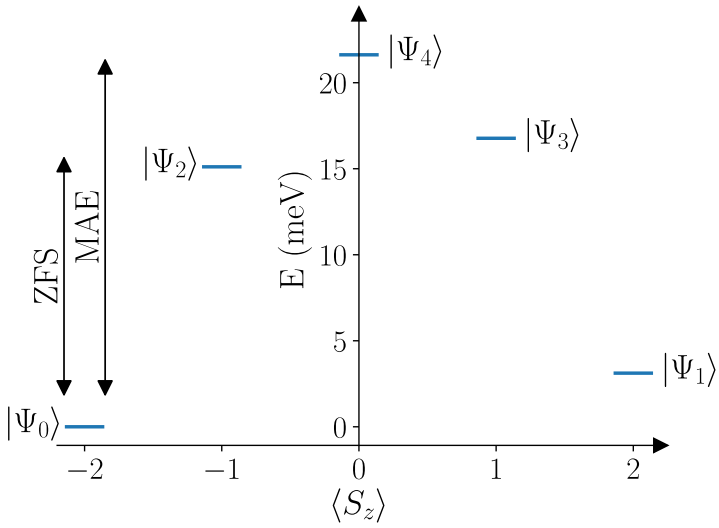

Figure 3.4: Energy level diagram of the 5 lowest energy states of the Crystal Field Hamiltonian (3.15).

responsible of the parabolic low energy spectrum shown in Figure 3.4. The quadratic evolution that shows the spin-orbit interaction indicates that it is a second order correction of the energy that mixes the two quintuplets generated by the TCF. Finally, the magnetic field induces the usual linear Zeeman splitting.

3.2.3 | Spin-flip lifetime

After analyzing the electronic and vibrational structure, in this section we study the electron-phonon spin-flip relaxation mechanism of the system. We examine the impact of all the different parameters on the spin lifetime, i.e. the effect of the number of MgO layers, the crystal field parameters, the magnetic field and the temperature.

3.2.3.1 | Effect of the MgO layer thickness

Figure 3.6 shows the calculated spin-flip lifetime for the direct transition for MgO coverages ranging from 2 ML to 4 ML at $T = 0\,\mathrm{K}$ and $B_z = 5\,\mathrm{T}$ computed using Eq. (3.14). The calculated lifetime ranges

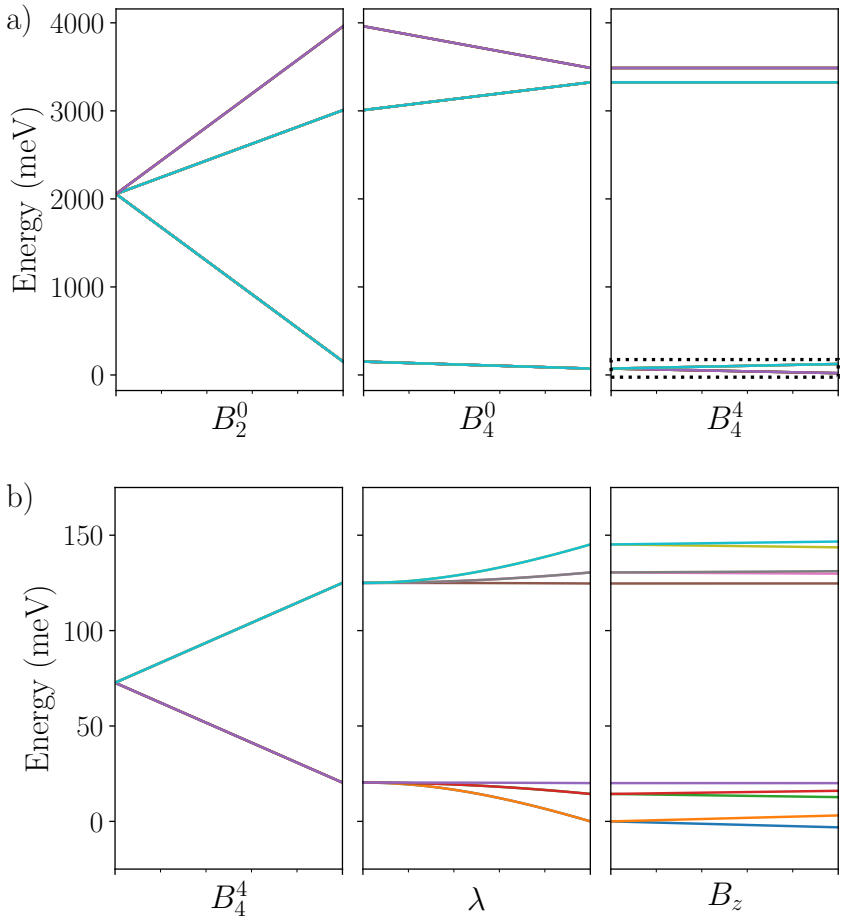

Figure 3.5: a) Evolution of the multiplet states energies under the ACF and TCF. b) Zoom of the evolution of low energy multiplet states under the TCF, spin-orbit interaction and magnetic field.

between 10 ms and 50 ms. In the case of 2 MLs, the experimentally measured spin lifetime is believed to be dominated by the electron-hole pair creation in the substrate [6], which is not included in our model; it is therefore reasonable that our calculated lifetime is nearly an order of magnitude larger than the experimentally measured one. However, for 3 and 4 ML coverages, the calculated lifetimes are of the same order as the experimentally measured values [6]. Noteworthily, as shown by the experimental measurements, our calculation also shows that the lifetime due to the spin-phonon coupling does not change drastically for 3 and 4 ML MgO coverages. Moreover, we found that for temperatures below 2 K, the lifetime does not change significantly (less than 10^{-8}ms), which is in good agreement the experimental measurements. This suggests that

the relaxation is caused by the spontaneous emission of phonons, instead than an absorption of thermally occupied phonon states [6].

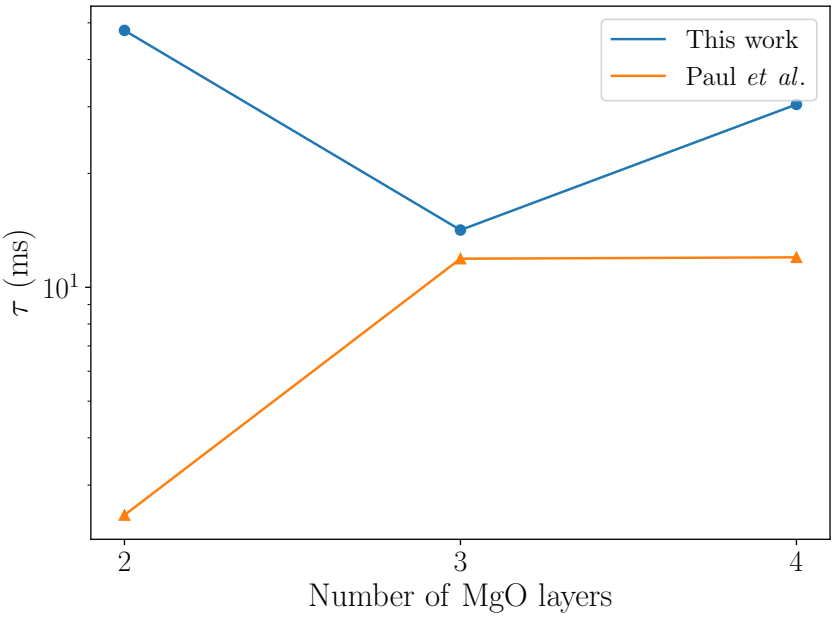

Figure 3.6: Spin lifetime as a function of the MgO coverage. Calculated values (blue) and experimental measurements (orange) from Ref. [6] are given by dots, while lines are shown as a guide for the eye.

On close inspection, we have found that the contributions to the multiplet wave functions $|\Psi_0\rangle$ and $|\Psi_1\rangle$ from states $|M_{\mathrm{S}}, M_{\mathrm{L}}\rangle = |\pm 2, \pm 2\rangle$ are determinant. This reveals that the spin relaxation mechanism is dominated by the overlap of components with $\Delta M_L = \pm 4$ This has important consequences and means that an effective Hamiltonian of the form

$$H_{eff} \propto L_+^4 + L_-^4, \tag{3.16}$$

captures the main characteristic of the spin-phonon coupling of the Fe adatom. In this aspect, the scattering process is related principally to the transition between the one-electron d_{xy} and $d_{x^2-y^2}$ orbitals shown in Figure 3.2. Therefore, changes on the hybridization of these states for different MgO coverages can cause variations on the spin lifetime.

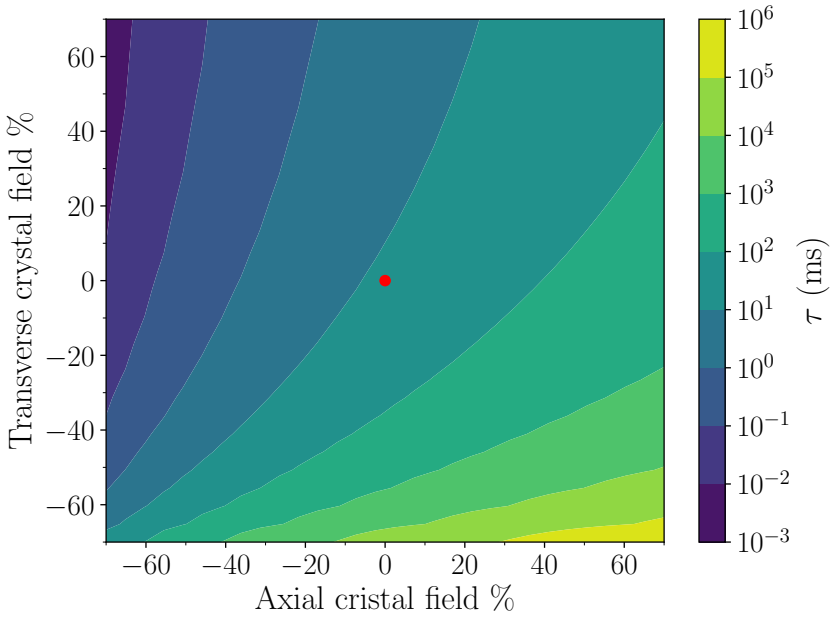

Figure 3.7: Calculated lifetime as a function of the ACF and TCF for 3 MLs of MgO. The red dot indicates the crystal field values given in Ref. [86].

3.2.3.2 | Influence of the crystal field

As an important observation, if TCF is absent ($B_4^4 = 0$ on Eq. (3.15) ($B_4^4 = 0$), the components with $\Delta M_L = \pm 4$ would not be mixed on the multiplet wave functions, preventing the decay of state $|\Psi_1\rangle$ into $|\Psi_0\rangle$. To investigate this aspect, we have computed the spin-lifetime varying both the ACF and the TCF to determine which term influences most the spin-phonon transition. Figure 3.7 shows that the lifetime is influenced in orders of magnitude by variations not only of the TCF, but also of the ACF. Additionally, Figure 3.7 reveals that in order to achieve longer spin lifetimes the ACF should be increased, whereas the TCF should be reduced. It is important to point out that the TCF is much smaller than the ACF (see parameters of Eq.(3.15)) and that Figure 3.7 shows relative variations of the crystal field parameters. However, as explained in Sec. 3.2.2.2, the low-energy spectrum of the adatom is closely related to the energy difference between the quintuplets created by the TCF. Therefore, small changes on the TCF have a much larger impact on the low-energy spectrum than variations in the ACF, which barely influences the low-energy levels. Moreover, as suggested in Ref. [3], the TCF can be easily modified in experiment, for example applying an oscillating bias voltage, which could have a big impact on the spin-lifetime measurements

according to our results.

3.2.3.3 | Magnetic field dependence

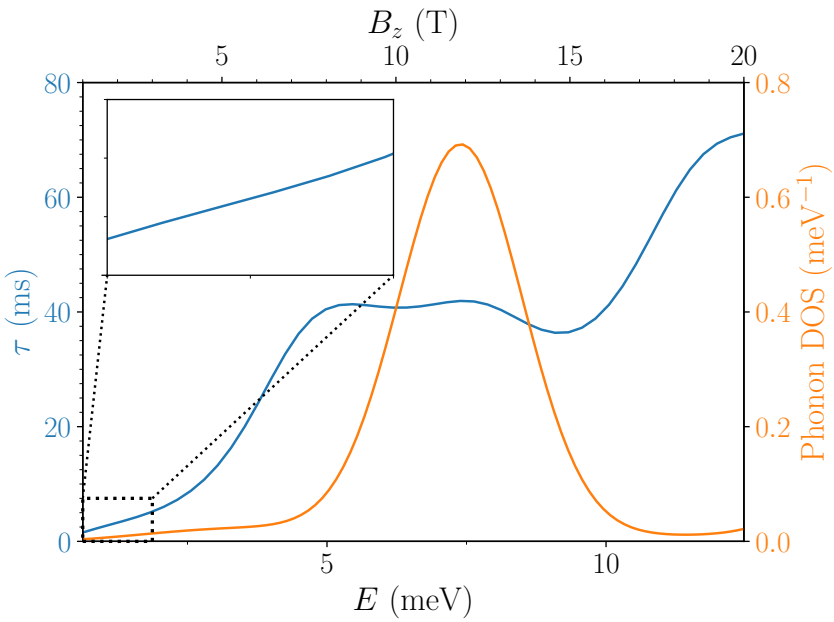

Figure 3.8: Lifetime as a function of the Zeeman splitting E (left axis) and phonon DOS projected onto the Fe adatom (right axis) for 3 MgO layers.

Another interesting property that is accessible in our model is the influence of the magnetic field on the spin-lifetime. Figure 3.8 shows the calculated lifetime (left axis) as a function of the magnetic field or Zeeman splitting energy for a magnetic field perpendicular to the substrate. We observe that for magnetic fields lower than 2 T, the lifetime increases linearly with the magnetic field, in excellent agreement whit previous experimental measurements [30]. This originates from the decreasing admixture of the states enabling $\Delta M_L = \pm 4$ transitions in the multiplet wave functions as the magnetic field increases. For this low energy range, the main scattering channel are phonons that are delocalized throughout the entire system.

Interestingly, when the Zeeman splitting matches the energy of the local in-plane mode of the iron adatom (shown by the projected phonon DOS in Figure 3.8), the lifetime saturates due to the sharp increase in density of available final states for that energy range. As such localized vibrations are a common feature of magnetic adatoms, we propose that

the experimental detection of such a plateau in the lifetime of the spin transitions is a clear way to prove that the spin-phonon coupling is indeed the primary relaxation mechanism.

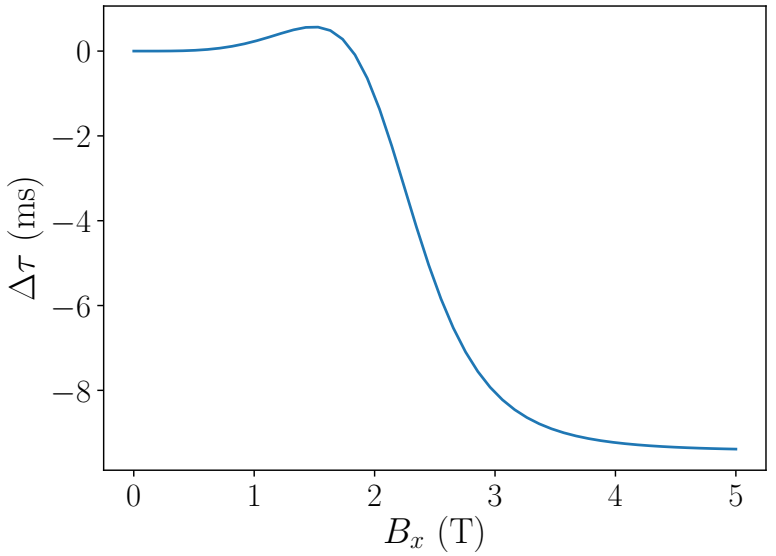

Figure 3.9: Lifetime as a function of a magnetic field parallel to the substrate for 3 MgO layers and $B_z = 5\,\mathrm{T}$.

On the other hand, the behavior of the lifetime when a magnetic field parallel to the substrate is applied is shown in Figure 3.9. The Zeeman term for a parallel magnetic field mixes states with $\Delta M_L = \pm 1$ and $\Delta M_S = \pm 1$. Initially, increasing B_x increments the spin lifetime because the coefficients of the $|M_\mathrm{S}, M_\mathrm{L}\rangle = |\pm 2, \pm 2\rangle$ terms are reduced due to the mixture that it produces. However, as the parallel magnetic field is further increased, new scattering channels are opened due to the bigger admixture of $|M_\mathrm{S}, M_\mathrm{L}\rangle$ states, until the lifetime saturates.

3.3 | Summary and outlook

In summary, we presented a theory that combines the multiplet structure of the adatom with the *ab-initio* information about all the electrons and phonons in the system and their coupling to study the electron-phonon-induced spin-flip transitions of adatoms on surfaces. We applied

our model to the Fe adatom on MgO/Ag(100), showing a good qualitative and order-of-magnitude agreement with available experiments by Paul *et al.* [6], demonstrating that the essential features of the problem are successfully captured within the developed theory. In particular, we reveal that both local vibrations of the adatom and substrate phonons of MgO are relevant for the spin relaxation, and that therefore, a correct description of the substrate is essential. Additionally, we identify the most important components of the multiplet states for the spin-phonon relaxation mechanism in this particular system. This has allowed exploring the effect of the crystal field on the spin lifetime, which can help future research on this field. Finally, we have studied the influence of the magnetic field on the spin lifetime, proposing that a saturation of the spin lifetime as a function of the applied magnetic field is a clear fingerprint of a dominant spin-phonon contribution to the relaxation process.

Chapter 4

Overview and final conclusions

The main goal of this thesis was to study from first principles the effect of the coupling between electrons and lattice vibrations in magnetic adatoms. For this purpose, we have considered the Fe adatom deposited on MgO/Ag(100) as a benchmark system.

First of all, in Chapter 2, we have studied the impact of the electron-phonon interaction on the electronic states of the Fe adatom deposited on MgO/Ag(100). We have pointed out the importance of the silver substrate providing final states to the scattering process. Using the Eliashberg function, we have shown that the oscillations in the plane of the adatom are the vibrational modes that show the biggest coupling with the electronic states of the adatom. This indicates the importance of the local in-plane modes in the electron-phonon coupling on adatoms, in agreement with what was found in Ho on MgO/Ag(100) [62]. We also have computed the strength of the electron-phonon interaction, represented by the λ parameter and the quasiparticle lifetime, for different numbers of MgO layers. Our calculations show qualitative differences for even and odd number of MgO layers, which are explained by the presence of an interface state of the substrate close to the high symmetry point X. The interface state represents the most important scattering channel for odd coverages of MgO, with a contribution up to 70% of the total scattering rate in the case of 3 ML coverage, whereas for an even number of MgO layers its contribution is highly suppressed. This disparity is caused by the distinct geometric position of the adatom with respect to the silver

substrate for even and odd coverages. Finally, we have shown that the calculated strength of the electron-phonon interaction on the case of a single MgO layer is comparable to the largest values found among bulk materials, while the electron-phonon scattering is deeply suppressed for two or more layers of MgO. This reveals that a single MgO layer is not capable of effectively screening the electron-phonon interaction on the iron adatom.

In Chapter 3 we have provided a better insight of the role of electron-phonon coupling in the spin-flip relaxation mechanism of the Fe adatom on MgO/Ag(100). We have presented a theory that combines the multiplet structure of the adatom with the *ab-initio* electronic and vibrational structures of the system and their coupling in order to study the electron-phonon-induced spin-flip transitions of adatoms on surfaces. Our calculations with the Fe adatom show a good order-of-magnitude agreement with available experiments by Paul *et al.* [6], which demonstrates that the essential features of the problem are successfully captured within the developed method. Additionally, our model has enabled us to identify the most important components of the multiplet states for the spin-phonon relaxation mechanism, revealing the critical electronic orbital states in this particular system. Moreover, we have explored the effect of the crystal field on the spin lifetime, which can help to design systems with longer spin-relaxation times in the future. Finally, we have analyzed the effect of the external magnetic field applied in experiments on the spin lifetime. We have identified that for the magnetic fields considered on the experiments both the localized vibrational modes of the iron and phonons from the MgO substrate contribute equally to the spin lifetime, showing that a correct description of the substrate is also essential. Our calculations also reveal a saturation of the spin lifetime when the Zeeman splitting matches the energy of the local in-plane mode of the iron adatom, which can be a clear fingerprint to identify experimentally a dominant spin-phonon contribution to the relaxation process.

As a final conclusion, we have conducted a novel study in the field of magnetic adatoms, developing and applying first principles methods to study the role of electron-phonon coupling in the spin relaxation mechanism.

Appendices

Appendix A

Pseudo-Potentials

The idea of pseudo-potentials is to replace the Coulomb potential of the atomic nucleus and the core electrons with an effective potential acting on valence electrons. Within this approach, the core electrons, together with the nuclei, are considered as a rigid ion cores, and the chemically active valence electrons are dealt with explicitly by means of significantly smoother pseudo wave functions. This brings two main computational benefits. First, it allows to deal with few valence electrons, and second, the pseudo wave functions of the latter can be expanded with smaller basis set. In this Appendix we review the basic theory and generation of norm-conserving pseudo-potentials.

The atomic Schrödinger equation

For a spherically symmetric atom, the radial and angular parts of the wave function can be separated using spherical harmonics:

$$\Psi_{nlm}(\mathbf{r}) = \psi_{nl}(r) Y_{lm}(\theta, \phi). \tag{A.1}$$

The resulting equation for the radial wave function is

$$-\frac{1}{2r^2}\frac{d}{dr}\left[r^2\frac{d}{dr}\psi_{nl}(r)\right] + \left[\frac{l(l+1)}{2r^2} + V_{ext}(r)\right]\psi_{nl}(r) = \varepsilon_{nl}\psi_{nl}(r). \tag{A.2}$$

Which, with the transformation $u_{nl}(r) = r\psi_{nl}(r)$, becomes

$$-\frac{1}{2}\frac{d^2}{dr^2}u_{nl}(r) + \left[\frac{l(l+1)}{2r^2} + V_{ext}(r)\right] u_{nl}(r) = \varepsilon_{nl}u_{nl}(r), \tag{A.3}$$

with boundary conditions $u_{nl}(r \to 0) \propto r^{l+1}$ and $u_{nl}(r \to \infty) \to 0$.

PSEUDO WAVE FUNCTIONS

Once the all electron wave functions, ψ_{nl}^{AE}, are obtained, the pseudo wave functions, ψ_{nl}^{PS}, are generated removing the nodes of the all electron wave functions. While different methods have been developed for this purpose, the pseudo wave functions must satisfy some requirements to be accurate and transferable. In the case of norm-conserving pseudo-potentials the all electron and pseudo wave functions must agree beyond a chosen core radius r_c, and inside r_c the integrated charge must be the same:

$$\int_0^{r_c} r^2|\psi_{nl}^{AE}|^2 dr = \int_0^{r_c} r^2|\psi_{nl}^{PS}|^2 dr. \tag{A.4}$$

Figure A.1 shows a comparison between the radial parts of the all electron wave functions and the pseudo wave functions for a Ag atom.

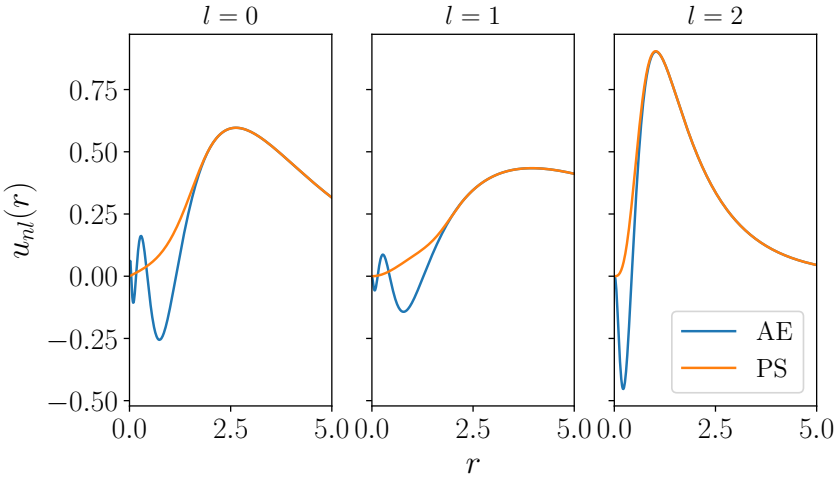

Figure A.1: Radial parts of the all electron and pseudo wave functions for a Ag atom.

l-DEPENDENT PSEUDO-POTENTIALS

The next step consists on computing the pseudo-potential from the pseudo wave functions. The first type of pseudo-potential is the semilocal one, which can be written as

$$\hat{V}_{SL} = V_{local}(r) + \delta\hat{V}_{SL} \tag{A.5}$$

$$= V_{local}(r) + \sum_{l,m} |Y_{lm}(\theta,\phi)\rangle\, \delta V_l(r)\, \langle Y_{lm}(\theta,\phi)|\,, \tag{A.6}$$

where

$$V_l(r) = V_{l,total} - (V^{PS}_{Hartree}(r) + V^{PS}_{xc}(r)), \tag{A.7}$$

and

$$\delta V_l(r) = V_l(r) - V_{local}(r). \tag{A.8}$$

Above $V^{PS}_{Hartree}$ and V^{PS}_{xc} are the Hartree potential and the exchange-correlation potential of the pseudo wave functions. In this type of pseudo-potential the wave functions are projected into spherical harmonics in order to obtain the potential. This is computationally expensive involving integrals of two wave functions:

$$\langle\psi_i|\, \delta\hat{V}_{SL}\, |\psi_j\rangle = \tag{A.9}$$

$$\int \left[\psi_i(\mathbf{r}) \sum_{l,m} Y_{lm}(\hat{\mathbf{r}})\delta V_l(r) \int sin\theta'\, Y_{lm}(\theta',\phi')\psi_j(r,\theta',\phi')\, d\theta' d\phi'\right] d\mathbf{r}. \tag{A.10}$$

SEPARABLE PSEUDO-POTENTIALS

To avoid this integrals Kleinman and Bylander showed that the effect of the semilocal $\delta V_l(r)$ potential can be replaced by a separable operator $\delta\hat{V}_{NL}$ so that the pseudo-potential has the form

$$\hat{V}_{PP} = V_{local}(r) + \delta\hat{V}_{NL}, \tag{A.11}$$

with

$$\delta\hat{V}_{NL} = \sum_{l,m} \frac{\left|\psi^{PS}_{lm}\delta V_l\right\rangle \left\langle\delta V_l\psi^{PS}_{lm}\right|}{\langle\psi^{PS}_{lm}|\, \delta V_l\, |\psi^{PS}_{lm}\rangle}. \tag{A.12}$$

The functions $\left\langle\delta V_l\psi^{PS}_{lm}\right|$ are projectors that operate on the wave functions as

$$\left\langle\delta V_l\psi^{PS}_{lm}|\psi\right\rangle = \int d\mathbf{r}\delta V_l(r)\psi^{PS}_{lm}(\mathbf{r})\psi(\mathbf{r}). \tag{A.13}$$

The advantage of this method is that matrix elements require only products of single wave function projections:

$$\langle\psi_i|\,\delta\hat{V}_{NL}\,|\psi_j\rangle = \sum_{l,m}\frac{\langle\psi_i|\psi_{lm}^{PS}\delta V_l\rangle\,\langle\delta V_l\psi_{lm}^{PS}|\psi_j\rangle}{\langle\psi_{lm}^{PS}|\,\delta V_l\,|\psi_{lm}^{PS}\rangle} \tag{A.14}$$

$$= \sum_{l,m}\int\delta V_l(r)\psi_{lm}^{PS}(\mathbf{r})\psi_i(\mathbf{r})d\mathbf{r}\int\delta V_l(r)\psi_{lm}^{PS}(\mathbf{r})\psi_j(\mathbf{r})d\mathbf{r} \times\frac{1}{\langle\psi_{lm}^{PS}|\,\delta V_l\,|\psi_{lm}^{PS}\rangle}. \tag{A.15}$$

The construction of the separable potential could be modified to generate the pseudo-potential directly without constructing the semilocal potential $V_l(r)$ first. Initially the pseudo wave functions $\psi_{lm}^{PS}(\mathbf{r})$ and the local potential $V_{local}(r)$ are created, as in the creation of a semilocal pseudo-potential. Then, defining the projector

$$\chi_{lm}^{PS}(\mathbf{r}) = \left\{\varepsilon_l - \left[-\frac{\nabla^2}{2} + V_{local}(r)\right]\right\}\psi_{lm}^{PS}(\mathbf{r}), \tag{A.16}$$

the non-local operator is written as

$$\delta\hat{V}_{NL} = \sum_{l,m}\frac{\left|\chi_{lm}^{PS}\right\rangle\left\langle\chi_{lm}^{PS}\right|}{\langle\chi_{lm}^{PS}|\psi_{lm}^{PS}\rangle}, \tag{A.17}$$

which the same properties of (A.12), i.e.

$$\hat{H}\psi_{lm}^{PS} = \varepsilon_l\psi_{lm}^{PS}. \tag{A.18}$$

To extend the range of energies over which the phase shifts of the original all-electron potential are described, the construction procedure of the projectors could be generalized to satisfy the Schrödinger equation at different energies ε_{ls} for each angular momentum. Thus,

$$\chi_{lms}^{PS}(\mathbf{r}) = \left\{\varepsilon_{ls} - \left[-\frac{\nabla^2}{2} + V_{local}(r)\right]\right\}\psi_{lms}^{PS}(\mathbf{r}). \tag{A.19}$$

And doing the transformation

$$\beta_{lms} = \sum_{s'} B^{-1}_{lms,lms'}\chi_{lms'}^{PS}, \tag{A.20}$$

where

$$B_{lms,l'm's'} = \left\langle \psi^{PS}_{lms} | \chi^{PS}_{l'm's'} \right\rangle = \delta_{lm,l'm'} \left\langle \psi^{PS}_{lms} | \chi^{PS}_{lms'} \right\rangle, \tag{A.21}$$

the separable PP can be written as

$$\delta \hat{V}_{NL} = \sum_{l,m} \left[\sum_{s,s'} B_{lms,lms'} \left| \beta_{lms} \right\rangle \left\langle \beta_{lms'} \right| \right]. \tag{A.22}$$

Appendix B

Density matrix

Using the matrix representation for the reduced density matrix,

$$\tilde{\rho}_{AA'}(t) = \langle A|\mathrm{Tr}_{\mathcal{B}}\tilde{\rho}(t)|A'\rangle = \sum_{B}\langle AB|\tilde{\rho}(t)|A'B\rangle, \tag{B.1}$$

it's time evolution within the Born-Markov approximation can be written as:

$$\frac{d\tilde{\rho}_{AA'}(t)}{dt} = -\int_0^\infty ds \sum_B \langle AB|\left[\tilde{V}(t),\left[\tilde{V}(t-s),\tilde{\rho}(t)\right]\right]|A'B\rangle. \tag{B.2}$$

Expanding the commutator (with $t' = t - s$),

$$\begin{aligned}\left[\tilde{V}(t),\left[\tilde{V}(t'),\tilde{\rho}(t)\right]\right] &= \left[\tilde{V}(t),\tilde{V}(t')\tilde{\rho}(t) - \tilde{\rho}(t)\tilde{V}(t')\right] \\ &= \tilde{V}(t)\tilde{V}(t')\tilde{\rho}(t) - \tilde{V}(t)\tilde{\rho}(t)\tilde{V}(t') \\ &\quad - \tilde{V}(t')\tilde{\rho}(t)\tilde{V}(t) + \tilde{\rho}(t)\tilde{V}(t')\tilde{V}(t),\end{aligned} \tag{B.3}$$

and taking into account that $\hat{V} = \sum_\alpha \hat{A}^\alpha \hat{B}^\alpha$, where the $\hat{A}^\alpha$ operators act on the system states and the $\hat{B}^\alpha$ operators on the bath states:

$$\begin{aligned}\left[\tilde{V}(t),\left[\tilde{V}(t'),\tilde{\rho}(t)\right]\right] = \sum_{\alpha,\beta}\Big[&\tilde{A}^\alpha(t)\tilde{B}^\alpha(t)\tilde{A}^\beta(t')\tilde{B}^\beta(t')\tilde{\rho}(t) \\ &-\tilde{A}^\alpha(t)\tilde{B}^\alpha(t)\tilde{\rho}(t)\tilde{A}^\beta(t')\tilde{B}^\beta(t') \\ &-\tilde{A}^\beta(t')\tilde{B}^\beta(t')\tilde{\rho}(t)\tilde{A}^\alpha(t)\tilde{B}^\alpha(t) \\ &+\tilde{\rho}(t)\tilde{A}^\beta(t')\tilde{B}^\beta(t')\tilde{A}^\alpha(t)\tilde{B}^\alpha(t)\Big].\end{aligned} \tag{B.4}$$

And separating each term:

$$\frac{d\tilde{\rho}_{AA'}(t)}{dt} = -\int_0^\infty ds C_1 + C_2 + C_3 + C_4. \tag{B.5}$$

Where,

$$\begin{aligned} C_1 &= \sum_{\alpha,\beta} \langle A|\tilde{A}^\alpha(t)\tilde{A}^\beta(t')\tilde{\rho}_{\mathcal{A}}(t)|A'\rangle \mathrm{Tr}_{\mathcal{B}}\left\{\tilde{B}^\alpha(t)\tilde{B}^\beta(t')\tilde{\rho}_{\mathcal{B}}^{eq.}\right\} \\ &= \sum_{\alpha,\beta} \langle A|\tilde{A}^\alpha(t)\tilde{A}^\beta(t')\tilde{\rho}_{\mathcal{A}}(t)|A'\rangle \langle\tilde{B}^\alpha(t)\tilde{B}^\beta(t')\rangle, \end{aligned} \tag{B.6}$$

$$\begin{aligned} C_2 &= -\sum_{\alpha,\beta} \langle A|\tilde{A}^\alpha(t)\tilde{\rho}_{\mathcal{A}}(t)\tilde{A}^\beta(t')|A'\rangle \mathrm{Tr}_{\mathcal{B}}\left\{\tilde{B}^\alpha(t)\tilde{\rho}_{\mathcal{B}}^{eq.}\tilde{B}^\beta(t')\right\} \\ &= -\sum_{\alpha,\beta} \langle A|\tilde{A}^\alpha(t)\tilde{\rho}_{\mathcal{A}}(t)\tilde{A}^\beta(t')|A'\rangle \langle\tilde{B}^\beta(t')\tilde{B}^\alpha(t)\rangle, \end{aligned} \tag{B.7}$$

$$\begin{aligned} C_3 &= -\sum_{\alpha,\beta} \langle A|\tilde{A}^\beta(t')\tilde{\rho}_{\mathcal{A}}(t)\tilde{A}^\alpha(t)|A'\rangle \mathrm{Tr}_{\mathcal{B}}\left\{\tilde{B}^\beta(t')\tilde{\rho}_{\mathcal{B}}^{eq.}\tilde{B}^\alpha(t)\right\} \\ &= -\sum_{\alpha,\beta} \langle A|\tilde{A}^\beta(t')\tilde{\rho}_{\mathcal{A}}(t)\tilde{A}^\alpha(t)|A'\rangle \langle\tilde{B}^\alpha(t)\tilde{B}^\beta(t')\rangle, \end{aligned} \tag{B.8}$$

and

$$\begin{aligned} C_4 &= \sum_{\alpha,\beta} \langle A|\tilde{\rho}_{\mathcal{A}}(t)\tilde{A}^\beta(t')\tilde{A}^\alpha(t)|A'\rangle \mathrm{Tr}_{\mathcal{B}}\left\{\tilde{\rho}_{\mathcal{B}}^{eq.}\tilde{B}^\beta(t')\tilde{B}^\alpha(t)\right\} \\ &= \sum_{\alpha,\beta} \langle A|\tilde{\rho}_{\mathcal{A}}(t)\tilde{A}^\beta(t')\tilde{A}^\alpha(t)|A'\rangle \langle\tilde{B}^\beta(t')\tilde{B}^\alpha(t)\rangle. \end{aligned} \tag{B.9}$$

Where the correlation functions are defined as

$$\begin{aligned} \langle\tilde{B}^\alpha(t)\tilde{B}^\beta(t')\rangle &= \mathrm{Tr}_{\mathcal{B}}\left\{\tilde{B}^\alpha(t)\tilde{B}^\beta(t')\tilde{\rho}_{\mathcal{B}}^{eq.}\right\} = \sum_B \langle B|\tilde{B}^\alpha(t)\tilde{B}^\beta(t')\tilde{\rho}_{\mathcal{B}}^{eq.}|B\rangle \\ &= \sum_{B,B_1,B_2} \langle B|\tilde{B}^\alpha(t)|B_1\rangle\langle B_1|\tilde{B}^\beta(t')|B_2\rangle\langle B_2|\tilde{\rho}_{\mathcal{B}}^{eq.}|B\rangle \\ &= \sum_{B,B_1,B_2} \langle B|\tilde{B}^\alpha(t)|B_1\rangle\langle B_1|\tilde{B}^\beta(t')|B_2\rangle \frac{e^{-\beta E_B}}{Z_{\mathcal{B}}}\delta_{B_2,B} \\ &= \sum_{B,B_1} \langle B|\tilde{B}^\alpha(t)|B_1\rangle\langle B_1|\tilde{B}^\beta(t')|B\rangle \frac{e^{-\beta E_B}}{Z_{\mathcal{B}}} \\ &= \sum_{B,B_1} e^{i(E_B - E_{B_1})(t-t')} B^\alpha_{BB_1} B^\beta_{B_1B} \frac{e^{-\beta E_B}}{Z_{\mathcal{B}}}, \end{aligned} \tag{B.10}$$

and

$$\begin{aligned}\langle\tilde{B}^{\beta}(t')\tilde{B}^{\alpha}(t)\rangle &= \mathrm{Tr}_{\mathcal{B}}\left\{\tilde{B}^{\beta}(t')\tilde{B}^{\alpha}(t)\tilde{\rho}_{\mathcal{B}}^{eq.}\right\} = \sum_{B}\langle B|\tilde{B}^{\beta}(t')\tilde{B}^{\alpha}(t)\tilde{\rho}_{\mathcal{B}}^{eq.}|B\rangle \\ &= \sum_{B,B_1,B_2}\langle B|\tilde{B}^{\beta}(t')|B_1\rangle\langle B_1|\tilde{B}^{\alpha}(t)|B_2\rangle\langle B_2|\tilde{\rho}_{\mathcal{B}}^{eq.}|B\rangle \\ &= \sum_{B,B_1,B_2}\langle B|\tilde{B}^{\beta}(t')|B_1\rangle\langle B_1|\tilde{B}^{\alpha}(t)|B_2\rangle\frac{e^{-\beta E_B}}{Z_{\mathcal{B}}}\delta_{B_2,B} \\ &= \sum_{B,B_1}\langle B|\tilde{B}^{\beta}(t')|B_1\rangle\langle B_1|\tilde{B}^{\alpha}(t)|B\rangle\frac{e^{-\beta E_B}}{Z_{\mathcal{B}}} \\ &= \sum_{B,B_1}e^{i(E_{B_1}-E_B)(t-t')}B^{\beta}_{BB_1}B^{\alpha}_{B_1B}\frac{e^{-\beta E_B}}{Z_{\mathcal{B}}}. \end{aligned} \tag{B.11}$$

Then,

$$\begin{aligned}C_1 &= \sum_{\alpha,\beta}\langle A|\tilde{A}^{\alpha}(t)\tilde{A}^{\beta}(t')\tilde{\rho}_{\mathcal{A}}(t)|A'\rangle\langle\tilde{B}^{\alpha}(t)\tilde{B}^{\beta}(t')\rangle \\ &= \sum_{\alpha,\beta}\sum_{A_1,A_2}\langle A|\tilde{A}^{\alpha}(t)|A1\rangle\langle A_1|\tilde{A}^{\beta}(t')|A_2\rangle\langle A_2|\tilde{\rho}_{\mathcal{A}}(t)|A'\rangle\langle\tilde{B}^{\alpha}(t)\tilde{B}^{\beta}(t')\rangle \\ &= \sum_{\alpha,\beta}\sum_{A_1,A_2}e^{i(E_A-E_{A_1})t}e^{i(E_{A_1}-E_{A_2})t'}A^{\alpha}_{AA_1}A^{\beta}_{A_1A_2}\tilde{\rho}_{A_2A'}(t)\langle\tilde{B}^{\alpha}(t)\tilde{B}^{\beta}(t')\rangle \\ &= \sum_{\alpha,\beta}\sum_{A_1,A_2}\sum_{B,B_1}e^{i(E_A-E_{A_1})t}e^{i(E_{A_1}-E_{A_2})t'}e^{i(E_B-E_{B_1})(t-t')} \\ &\qquad\times A^{\alpha}_{AA_1}A^{\beta}_{A_1A_2}\tilde{\rho}_{A_2A'}(t)B^{\alpha}_{BB_1}B^{\beta}_{B_1B}\frac{e^{-\beta E_B}}{Z_{\mathcal{B}}}, \end{aligned} \tag{B.12}$$

$$\begin{aligned}C_2 &= -\sum_{\alpha,\beta}\langle A|\tilde{A}^{\alpha}(t)\tilde{\rho}_{\mathcal{A}}(t)\tilde{A}^{\beta}(t')|A'\rangle\langle\tilde{B}^{\beta}(t')\tilde{B}^{\alpha}(t)\rangle \\ &= -\sum_{\alpha,\beta}\sum_{A_1,A_2}\langle A|\tilde{A}^{\alpha}(t)|A1\rangle\langle A_1|\tilde{\rho}_{\mathcal{A}}(t)|A_2\rangle\langle A_2|\tilde{A}^{\beta}(t')|A'\rangle\langle\tilde{B}^{\beta}(t')\tilde{B}^{\alpha}(t)\rangle \\ &= -\sum_{\alpha,\beta}\sum_{A_1,A_2}e^{i(E_A-E_{A_1})t}e^{i(E_{A_2}-E_{A'})t'}A^{\alpha}_{AA_1}\tilde{\rho}_{A_1A_2}(t)A^{\beta}_{A_2A'}\langle\tilde{B}^{\beta}(t')\tilde{B}^{\alpha}(t)\rangle \\ &= -\sum_{\alpha,\beta}\sum_{A_1,A_2}\sum_{B,B_1}e^{i(E_A-E_{A_1})t}e^{i(E_{A_2}-E_{A'})t'}e^{i(E_{B_1}-E_B)(t-t')} \\ &\qquad\times A^{\alpha}_{AA_1}\tilde{\rho}_{A_1A_2}(t)A^{\beta}_{A_2A'}B^{\beta}_{BB_1}B^{\alpha}_{B_1B}\frac{e^{-\beta E_B}}{Z_{\mathcal{B}}}, \end{aligned} \tag{B.13}$$

$$
\begin{aligned}
C_3 &= -\sum_{\alpha,\beta}\langle A|\tilde{A}^{\beta}(t')\tilde{\rho}_{\mathcal{A}}(t)\tilde{A}^{\alpha}(t)|A'\rangle\langle\tilde{B}^{\alpha}(t)\tilde{B}^{\beta}(t')\rangle \\
&= -\sum_{\alpha,\beta}\sum_{A_1,A_2}\langle A|\tilde{A}^{\beta}(t')|A1\rangle\langle A_1|\tilde{\rho}_{\mathcal{A}}(t)|A_2\rangle\langle A_2|\tilde{A}^{\alpha}(t)|A'\rangle\langle\tilde{B}^{\alpha}(t)\tilde{B}^{\beta}(t')\rangle \\
&= -\sum_{\alpha,\beta}\sum_{A_1,A_2} e^{i(E_A-E_{A_1})t'}e^{i(E_{A_2}-E_{A'})t}A^{\beta}_{AA_1}\tilde{\rho}_{A_1A_2}(t)A^{\alpha}_{A_2A'}\langle\tilde{B}^{\alpha}(t)\tilde{B}^{\beta}(t')\rangle \\
&= -\sum_{\alpha,\beta}\sum_{A_1,A_2}\sum_{B,B_1} e^{i(E_A-E_{A_1})t'}e^{i(E_{A_2}-E_{A'})t}e^{i(E_B-E_{B_1})(t-t')} \\
&\qquad\qquad \times A^{\beta}_{AA_1}\tilde{\rho}_{A_1A_2}(t)A^{\alpha}_{A_2A'}B^{\alpha}_{BB_1}B^{\beta}_{B_1B}\frac{e^{-\beta E_B}}{Z_{\mathcal{B}}}, \qquad \text{(B.14)}
\end{aligned}
$$

and

$$
\begin{aligned}
C_4 &= \sum_{\alpha,\beta}\langle A|\tilde{\rho}_{\mathcal{A}}(t)\tilde{A}^{\beta}(t')\tilde{A}^{\alpha}(t)|A'\rangle\langle\tilde{B}^{\beta}(t')\tilde{B}^{\alpha}(t)\rangle \\
&= \sum_{\alpha,\beta}\sum_{A_1,A_2}\langle A|\tilde{\rho}_{\mathcal{A}}(t)|A1\rangle\langle A_1|\tilde{A}^{\beta}(t')|A_2\rangle\langle A_2|\tilde{A}^{\alpha}(t)|A'\rangle\langle\tilde{B}^{\beta}(t')\tilde{B}^{\alpha}(t)\rangle \\
&= \sum_{\alpha,\beta}\sum_{A_1,A_2} e^{i(E_{A_1}-E_{A_2})t'}e^{i(E_{A_2}-E_{A'})t}\tilde{\rho}_{AA_1}(t)A^{\beta}_{A_1A_2}A^{\alpha}_{A_2A'}\langle\tilde{B}^{\beta}(t')\tilde{B}^{\alpha}(t)\rangle \\
&= \sum_{\alpha,\beta}\sum_{A_1,A_2}\sum_{B,B_1} e^{i(E_{A_1}-E_{A_2})t'}e^{i(E_{A_2}-E_{A'})t}e^{i(E_{B_1}-E_B)(t-t')} \\
&\qquad\qquad \times \tilde{\rho}_{AA_1}(t)A^{\beta}_{A_1A_2}A^{\alpha}_{A_2A'}B^{\beta}_{BB_1}B^{\alpha}_{B_1B}\frac{e^{-\beta E_B}}{Z_{\mathcal{B}}}. \qquad \text{(B.15)}
\end{aligned}
$$

Doing now each integral:

$$
\begin{aligned}
I_1 &= -\int_0^{\infty} dsC_1 \\
&= -\sum_{\alpha,\beta}\sum_{A_1,A_2}\sum_{B,B_1} A^{\alpha}_{AA_1}A^{\beta}_{A_1A_2}\tilde{\rho}_{A_2A'}(t)B^{\alpha}_{BB_1}B^{\beta}_{B_1B}\frac{e^{-\beta E_B}}{Z_{\mathcal{B}}} \\
&\qquad\qquad \times e^{i(E_A-E_{A_2})t}\int_0^{\infty} dse^{i(E_{A_2}-E_{A_1}+E_B-E_{B_1})s}. \qquad \text{(B.16)}
\end{aligned}
$$

And introducing a convergence factor $\eta \to 0^+$:

$$\int_0^\infty ds e^{i(E_{A_2}-E_{A_1}+E_B-E_{B_1})s} = \int_0^\infty ds e^{i(E_{A_2}-E_{A_1}+E_B-E_{B_1})s} e^{-\eta s} = \frac{i}{E_{A_2}-E_{A_1}+E_B-E_{B_1}+i\eta}. \quad \text{(B.17)}$$

Where I have used $\int_0^\infty ds e^{(iA-\eta)s} = i/(A+i\eta)$.

Thus,

$$I_1 = -\sum_{\alpha,\beta}\sum_{A_1,A_2}\sum_{B,B_1} A^\alpha_{AA_1} A^\beta_{A_1A_2} \tilde{\rho}_{A_2A'}(t) B^\alpha_{BB_1} B^\beta_{B_1B} \frac{e^{-\beta E_B}}{Z_{\mathcal{B}}} \times \frac{i e^{i(E_A-E_{A_2})t}}{E_{A_2}-E_{A_1}+E_B-E_{B_1}+i\eta}, \quad \text{(B.18)}$$

$$\begin{aligned} I_2 &= \sum_{\alpha,\beta}\sum_{A_1,A_2}\sum_{B,B_1} A^\alpha_{AA_1} \tilde{\rho}_{A_1A_2}(t) A^\beta_{A_2A'} B^\beta_{BB_1} B^\alpha_{B_1B} \frac{e^{-\beta E_B}}{Z_{\mathcal{B}}} \\ &\quad \times e^{i(E_A-E_{A_1})t} \int_0^\infty ds e^{i(E_{A_2}-E_{A'})(t-s)} e^{i(E_{B_1}-E_B)s} \\ &= \sum_{\alpha,\beta}\sum_{A_1,A_2}\sum_{B,B_1} A^\alpha_{AA_1} \tilde{\rho}_{A_1A_2}(t) A^\beta_{A_2A'} B^\beta_{BB_1} B^\alpha_{B_1B} \frac{e^{-\beta E_B}}{Z_{\mathcal{B}}} \\ &\quad \times \frac{i e^{i(E_A-E_{A_1}+E_{A_2}-E_{A'})t}}{E_{A'}-E_{A_2}+E_{B_1}-E_B+i\eta}, \end{aligned} \quad \text{(B.19)}$$

$$\begin{aligned} I_3 &= \sum_{\alpha,\beta}\sum_{A_1,A_2}\sum_{B,B_1} A^\beta_{AA_1} \tilde{\rho}_{A_1A_2}(t) A^\alpha_{A_2A'} B^\alpha_{BB_1} B^\beta_{B_1B} \frac{e^{-\beta E_B}}{Z_{\mathcal{B}}} \\ &\quad \times e^{i(E_{A_2}-E_{A'})t} \int_0^\infty ds e^{i(E_A-E_{A_1})(t-s)} e^{i(E_B-E_{B_1})s} \\ &= \sum_{\alpha,\beta}\sum_{A_1,A_2}\sum_{B,B_1} A^\beta_{AA_1} \tilde{\rho}_{A_1A_2}(t) A^\alpha_{A_2A'} B^\alpha_{BB_1} B^\beta_{B_1B} \frac{e^{-\beta E_B}}{Z_{\mathcal{B}}} \\ &\quad \times \frac{i e^{i(E_{A_2}-E_{A'}+E_A-E_{A_1})t}}{E_{A_1}-E_A+E_B-E_{B_1}+i\eta}, \end{aligned} \quad \text{(B.20)}$$

and

$$
\begin{aligned}
I_4 = &-\sum_{\alpha,\beta}\sum_{A_1,A_2}\sum_{B,B_1}\tilde{\rho}_{AA_1}(t)A^{\beta}_{A_1A_2}A^{\alpha}_{A_2A'}B^{\beta}_{BB_1}B^{\alpha}_{B_1B}\frac{e^{-\beta E_B}}{Z_{\mathcal{B}}} \\
&\times e^{i(E_{A_2}-E_{A'})t}\int_0^{\infty} ds e^{i(E_{A_1}-E_{A_2})(t-s)}e^{i(E_{B_1}-E_B)s} \\
= &-\sum_{\alpha,\beta}\sum_{A_1,A_2}\sum_{B,B_1}\tilde{\rho}_{AA_1}(t)A^{\beta}_{A_1A_2}A^{\alpha}_{A_2A'}B^{\beta}_{BB_1}B^{\alpha}_{B_1B}\frac{e^{-\beta E_B}}{Z_{\mathcal{B}}} \\
&\times \frac{ie^{i(E_{A_1}-E_{A'})t}}{E_{A_2}-E_{A_1}+E_{B_1}-E_B+i\eta}. \qquad \text{(B.21)}
\end{aligned}
$$

Plugging the four contributions in (B.5) and renaming some α, β indices:

$$
\begin{aligned}
\frac{d\tilde{\rho}_{AA'}(t)}{dt} = &-\sum_{\alpha,\beta}\sum_{A_1,A_2}\sum_{B,B_1}A^{\alpha}_{AA_1}A^{\beta}_{A_1A_2}\tilde{\rho}_{A_2A'}(t)B^{\alpha}_{BB_1}B^{\beta}_{B_1B}\frac{e^{-\beta E_B}}{Z_{\mathcal{B}}} \\
&\times \frac{ie^{i(E_A-E_{A_2})t}}{E_{A_2}-E_{A_1}+E_B-E_{B_1}+i\eta} \\
&+\sum_{\alpha,\beta}\sum_{A_1,A_2}\sum_{B,B_1}A^{\beta}_{AA_1}\tilde{\rho}_{A_1A_2}(t)A^{\alpha}_{A_2A'}B^{\alpha}_{BB_1}B^{\beta}_{B_1B}\frac{e^{-\beta E_B}}{Z_{\mathcal{B}}} \\
&\times \frac{ie^{i(E_A-E_{A_1}+E_{A_2}-E_{A'})t}}{E_{A'}-E_{A_2}+E_{B_1}-E_B+i\eta} \\
&+\sum_{\alpha,\beta}\sum_{A_1,A_2}\sum_{B,B_1}A^{\beta}_{AA_1}\tilde{\rho}_{A_1A_2}(t)A^{\alpha}_{A_2A'}B^{\alpha}_{BB_1}B^{\beta}_{B_1B}\frac{e^{-\beta E_B}}{Z_{\mathcal{B}}} \\
&\times \frac{ie^{i(E_{A_2}-E_{A'}+E_A-E_{A_1})t}}{E_{A_1}-E_A+E_B-E_{B_1}+i\eta} \\
&-\sum_{\alpha,\beta}\sum_{A_1,A_2}\sum_{B,B_1}\tilde{\rho}_{AA_1}(t)A^{\alpha}_{A_1A_2}A^{\beta}_{A_2A'}B^{\beta}_{BB_1}B^{\beta}_{B_1B}\frac{e^{-\beta E_B}}{Z_{\mathcal{B}}} \\
&\times \frac{ie^{i(E_{A_1}-E_{A'})t}}{E_{A_2}-E_{A_1}+E_{B_1}-E_B+i\eta}. \qquad \text{(B.22)}
\end{aligned}
$$

Defining the correlation function

$$\langle B^{\alpha\beta}(\omega)\rangle = \sum_{B,B_1} \frac{e^{-\beta E_B}}{Z_{\mathcal{B}}} \frac{B^{\alpha}_{BB_1} B^{\beta}_{B_1 B}}{\omega + E_B - E_{B_1}} \tag{B.23}$$

$$= -\sum_{B,B_1} \frac{e^{-\beta E_B}}{Z_{\mathcal{B}}} \frac{B^{\alpha}_{BB_1} B^{\beta}_{B_1 B}}{-\omega + E_{B_1} - E_B}, \tag{B.24}$$

it can be rewritten as:

$$\begin{aligned}
\frac{d\tilde{\rho}_{AA'}(t)}{dt} = &-\sum_{\alpha,\beta}\sum_{A_1,A_2} iA^{\alpha}_{AA_1} A^{\beta}_{A_1A_2} \tilde{\rho}_{A_2A'}(t) e^{i(E_A - E_{A_2})t} \\
&\qquad \times \langle B^{\alpha\beta}(E_{A_2} - E_{A_1} + i\eta)\rangle \\
&-\sum_{\alpha,\beta}\sum_{A_1,A_2} iA^{\beta}_{AA_1} \tilde{\rho}_{A_1A_2}(t) A^{\alpha}_{A_2A'} e^{i(E_A - E_{A_1} + E_{A_2} - E_{A'})t} \\
&\qquad \times \langle B^{\alpha\beta}(E_{A_2} - E_{A'} - i\eta)\rangle \\
&+\sum_{\alpha,\beta}\sum_{A_1,A_2} iA^{\beta}_{AA_1} \tilde{\rho}_{A_1A_2}(t) A^{\alpha}_{A_2A'} e^{i(E_{A_2} - E_{A'} + E_A - E_{A_1})t} \\
&\qquad \times \langle B^{\alpha\beta}(E_{A_1} - E_A + i\eta)\rangle \\
&+\sum_{\alpha,\beta}\sum_{A_1,A_2} i\tilde{\rho}_{AA_1}(t) A^{\alpha}_{A_1A_2} A^{\beta}_{A_2A'} e^{i(E_{A_1} - E_{A'})t} \\
&\qquad \times \langle B^{\alpha\beta}(E_{A_1} - E_{A_2} - i\eta)\rangle.
\end{aligned} \tag{B.25}$$

Returning to the Schrödinger picture by using

$$\rho_{AA'}(t) = e^{-i(E_A - E_{A'})t} \tilde{\rho}_{A,A'}(t) \tag{B.26}$$

and

$$\begin{aligned}
\frac{d\rho_{AA'}(t)}{dt} &= -i(E_A - E_{A'}) e^{-i(E_A - E_{A'})t} \tilde{\rho}_{A,A'}(t) + e^{-i(E_A - E_{A'})t} \frac{d\tilde{\rho}_{AA'}(t)}{dt} \\
&= -i(E_A - E_{A'}) \rho_{A,A'}(t) + e^{-i(E_A - E_{A'})t} \frac{d\tilde{\rho}_{AA'}(t)}{dt}.
\end{aligned} \tag{B.27}$$

The master equation becomes

$$\begin{aligned}\frac{d\rho_{AA'}(t)}{dt} =& -i(E_A - E_{A'})\rho_{A,A'}(t) \\ &- \sum_{\alpha,\beta}\sum_{A_1,A_2} iA^{\alpha}_{AA_1}A^{\beta}_{A_1A_2}\rho_{A_2A'}(t)\langle B^{\alpha\beta}(E_{A_2} - E_{A_1} + i\eta)\rangle \\ &- \sum_{\alpha,\beta}\sum_{A_1,A_2} iA^{\beta}_{AA_1}\rho_{A_1A_2}(t)A^{\alpha}_{A_2A'}\langle B^{\alpha\beta}(E_{A_2} - E_{A'} - i\eta)\rangle \\ &+ \sum_{\alpha,\beta}\sum_{A_1,A_2} iA^{\beta}_{AA_1}\rho_{A_1A_2}(t)A^{\alpha}_{A_2A'}\langle B^{\alpha\beta}(E_{A_1} - E_A + i\eta)\rangle \\ &+ \sum_{\alpha,\beta}\sum_{A_1,A_2} i\rho_{AA_1}(t)A^{\alpha}_{A_1A_2}A^{\beta}_{A_2A'}\langle B^{\alpha\beta}(E_{A_1} - E_{A_2} - i\eta)\rangle.\end{aligned} \tag{B.28}$$

Taking only the diagonal elements of the density matrix on both sides of the equation we will obtain Fermi's Golden Rule:

$$\begin{aligned}\frac{d\rho_{AA}(t)}{dt} =& -\sum_{\alpha,\beta}\sum_{A_1} iA^{\alpha}_{AA_1}A^{\beta}_{A_1A}\rho_{AA}(t)\langle B^{\alpha\beta}(E_A - E_{A_1} + i\eta)\rangle \\ &- \sum_{\alpha,\beta}\sum_{A_1} iA^{\beta}_{AA_1}\rho_{A_1A_1}(t)A^{\alpha}_{A_1A}\langle B^{\alpha\beta}(E_{A_1} - E_A - i\eta)\rangle \\ &+ \sum_{\alpha,\beta}\sum_{A_1} iA^{\beta}_{AA_1}\rho_{A_1A_1}(t)A^{\alpha}_{A_1A}\langle B^{\alpha\beta}(E_{A_1} - E_A + i\eta)\rangle \\ &+ \sum_{\alpha,\beta}\sum_{A_1} i\rho_{AA}(t)A^{\alpha}_{AA_1}A^{\beta}_{A_1A}\langle B^{\alpha\beta}(E_A - E_{A_1} - i\eta)\rangle.\end{aligned} \tag{B.29}$$

And using

$$\lim_{\eta\to 0^+}\frac{1}{\omega \pm i\eta} = \mathcal{P}\frac{1}{\omega} \mp i\pi\delta(\omega), \tag{B.30}$$

the correlation function will be

$$\begin{aligned}\langle B^{\alpha\beta}(\omega \pm i\eta)\rangle &= \sum_{B,B_1}\frac{e^{-\beta E_B}}{Z_{\mathcal{B}}}\frac{B^{\alpha}_{BB_1}B^{\beta}_{B_1B}}{\omega + E_B - E_{B_1} + i\eta} \\ &= \sum_{B,B_1}\frac{e^{-\beta E_B}}{Z_{\mathcal{B}}}B^{\alpha}_{BB_1}B^{\beta}_{B_1B} \\ &\quad\times\left(\mathcal{P}\frac{1}{\omega + E_B - E_{B_1}} \mp i\pi\delta\left(\omega + E_B - E_{B_1}\right)\right).\end{aligned} \tag{B.31}$$

Thus:

$$\frac{d\rho_{AA}(t)}{dt} = -2\pi \sum_{\alpha,\beta} \sum_{A_1} \sum_{B,B_1} \frac{e^{-\beta E_B}}{Z_{\mathcal{B}}} B^{\alpha}_{BB_1} B^{\beta}_{B_1 B} A^{\alpha}_{AA_1} A^{\beta}_{A_1 A} \rho_{AA}(t) \times \delta\left(E_A - E_{A_1} + E_B - E_{B_1}\right)$$

$$+ 2\pi \sum_{\alpha,\beta} \sum_{A_1} \sum_{B,B_1} \frac{e^{-\beta E_B}}{Z_{\mathcal{B}}} B^{\alpha}_{BB_1} B^{\beta}_{B_1 B} A^{\beta}_{AA_1} \rho_{A_1 A_1}(t) A^{\alpha}_{A_1 A} \times \delta\left(E_{A_1} - E_A + E_B - E_{B_1}\right). \tag{B.32}$$

And trying a solution like $\rho_{AA}(t) = e^{-\Gamma_A t}\rho_{AA}(t_0)$ yields the Fermi's Golden Rule for the scattering rate:

$$\Gamma_A = +2\pi \sum_{\alpha,\beta} \sum_{A_1} \sum_{B,B_1} \frac{e^{-\beta E_B}}{Z_{\mathcal{B}}} B^{\alpha}_{BB_1} B^{\beta}_{B_1 B} A^{\alpha}_{AA_1} A^{\beta}_{A_1 A} \times \delta\left(E_A - E_{A_1} + E_B - E_{B_1}\right)$$

$$- 2\pi \sum_{\alpha,\beta} \sum_{A_1} \sum_{B,B_1} \frac{e^{-\beta E_B}}{Z_{\mathcal{B}}} B^{\alpha}_{BB_1} B^{\beta}_{B_1 B} A^{\beta}_{AA_1} A^{\alpha}_{A_1 A} \times \delta\left(E_{A_1} - E_A + E_B - E_{B_1}\right). \tag{B.33}$$

Example

As a simple example we will consider a spin system coupled with a phonon bath. For the spin system we consider the next Hamiltonian:

$$\hat{H}_S = D\hat{S}_z^2 + \mu_B g B \hat{S}_z,$$

for the phonon bath

$$\hat{H}_{ph.} = \omega_\nu \left(b_\nu^\dagger b_\nu + \frac{1}{2}\right), \tag{B.34}$$

and lets consider that the coupling between both systems is modeled with the Hamiltonian

$$\hat{V} = \frac{\lambda_\nu}{2}\left(\hat{S}_+^2 + \hat{S}_-^2\right)\left(b_\nu^\dagger + b_\nu\right). \tag{B.35}$$

The basis for the spin Hamiltonian is

$$|A\rangle \to |s,m\rangle \equiv |m\rangle, \tag{B.36}$$

where

$$\hat{H}_S|m\rangle = (Dm^2 + \mu_B Bm)|m\rangle. \tag{B.37}$$

And the basis for the phonon Hamiltonian is

$$|B\rangle \to |n\rangle = \frac{1}{\sqrt{n!}}\prod_{i=0}^{n} b_\nu^\dagger|0\rangle = \frac{1}{\sqrt{n!}}\left(b_\nu^\dagger\right)^n|0\rangle, \tag{B.38}$$

with

$$\hat{H}_{ph.}|n\rangle = \omega_\nu\left(n+\frac{1}{2}\right)|n\rangle, \tag{B.39}$$

where n is the number of phonons of the system. The density matrix at thermal equilibrium is given by

$$\hat{\rho}_{ph.}^{eq.} = \sum_{n=0}^{\infty}\frac{e^{-\beta\omega_\nu(n+1/2)}}{Z_{ph.}^{eq.}}|n\rangle\langle n|, \tag{B.40}$$

where $Z_{ph.}^{eq.}$ is the grand partition function defined as

$$\begin{aligned} Z_{ph.}^{eq.} &= \mathrm{Tr}\left\{e^{-\beta H_{ph.}}\right\} = \sum_{n=0}^{\infty}\langle n|e^{-\beta H_{ph.}}|n\rangle = \sum_{n=0}^{\infty}e^{-\beta\omega_\nu(n+1/2)} \\ &= e^{-\beta\omega_\nu/2}\sum_{n=0}^{\infty}e^{-\beta\omega_\nu n} = e^{-\beta\omega_\nu/2}\sum_{n=0}^{\infty}\left(e^{-\beta\omega_\nu}\right)^n \\ &= \frac{e^{-\beta\omega_\nu/2}}{1-e^{-\beta\omega_\nu}}. \end{aligned} \tag{B.41}$$

The average number of particles can be calculated from the density matrix, and gives the usual expression for the Bose-Einstein distribution:

$$\begin{aligned} \langle\hat{n}\rangle = n_{BE}(\omega_\nu) &= \mathrm{Tr}\left\{\hat{n}\hat{\rho}_{ph.}^{eq.}\right\} = \sum_{n=0}^{\infty}n\frac{e^{-\beta\omega_\nu(n+1/2)}}{Z_{ph.}^{eq.}} \\ &= \sum_{n=0}^{\infty}ne^{-\beta\omega_\nu(n+1/2)}\frac{1-e^{-\beta\omega_\nu}}{e^{-\beta\omega_\nu/2}} = \left(1-e^{-\beta\omega_\nu}\right)\sum_{n=0}^{\infty}n\left(e^{-\beta\omega_\nu}\right)^n \\ &= \left(1-e^{-\beta\omega_\nu}\right)\frac{e^{-\beta\omega_\nu}}{\left(e^{-\beta\omega_\nu}-1\right)^2} = -\frac{e^{-\beta\omega_\nu}}{e^{-\beta\omega_\nu}-1} = \frac{1}{e^{\beta\omega_\nu}-1} \end{aligned} \tag{B.42}$$

In this example, the part of the interaction $\hat{V}$ acting on the spin system is

$$A = A^{\alpha} = A^{\beta} = \lambda_{\nu} \left(\hat{S}_{+}^{2} + \hat{S}_{-}^{2} \right), \tag{B.43}$$

with the matrix elements

$$\begin{aligned} A_{m,m'} &= \frac{\lambda_{\nu}}{2} \langle m | \hat{S}_{+}^{2} + \hat{S}_{-}^{2} | m' \rangle \\ &= \frac{\lambda_{\nu}}{2} \left(\langle m | \hat{S}_{+}^{2} | m' \rangle + \langle m | \hat{S}_{-}^{2} | m' \rangle \right) \\ &= \frac{\lambda_{\nu}}{2} \Big(\quad \sqrt{(s-m')(s+m'+1)(s-m'-1)(s+m'+2)} \delta_{m,m'+2} \\ &\qquad + \sqrt{(s+m')(s-m'+1)(s+m'-1)(s-m'+2)} \delta_{m,m'-2} \Big) \\ &= \frac{\lambda_{\nu}}{2} \left(A_{+}(m') \delta_{m,m'+2} + A_{-}(m') \delta_{m,m'-2} \right). \end{aligned} \tag{B.44}$$

On the other hand, the interaction acting on the phonon system is

$$B = B^{\alpha} = B^{\beta} = \left(b_{\nu}^{\dagger} + b_{\nu} \right), \tag{B.45}$$

with the matrix elements

$$B_{n,n'} = \langle n | b_{\nu}^{\dagger} + b_{\nu} | n' \rangle = \sqrt{n'+1} \delta_{n,n'+1} + \sqrt{n'} \delta_{n,n'-1}. \tag{B.46}$$

Thus, the correlation function is

$$\begin{aligned} \langle B(\omega) \rangle &= \sum_{n,n'} \frac{e^{-\beta E_n}}{Z_{\mathcal{B}}} \frac{B_{nn'} B_{n'n}}{\omega + E_n - E_{n'}} \\ &= \sum_{n,n'} \frac{e^{-\beta E_n}}{Z_{\mathcal{B}}} \frac{\left(\sqrt{n'+1} \sqrt{n} \delta_{n',n-1} + \sqrt{n'} \sqrt{n+1} \delta_{n',n+1} \right)}{\omega + E_n - E_{n'}} \\ &= \sum_{n} \frac{e^{-\beta E_n}}{Z_{\mathcal{B}}} \left(\frac{n}{\omega + E_n - E_{n-1}} + \frac{n+1}{\omega + E_n - E_{n+1}} \right) \\ &= \sum_{n} \frac{e^{-\beta E_n}}{Z_{\mathcal{B}}} \left(\frac{n}{\omega + \omega_{\nu}} + \frac{n+1}{\omega - \omega_{\nu}} \right) \\ &= \left(\frac{n_{BE}}{\omega + \omega_{\nu}} + \frac{n_{BE}+1}{\omega - \omega_{\nu}} \right). \end{aligned} \tag{B.47}$$

Plugging this on the Liouville-von Neumann and taking only the diagonal elements of the density matrix we obtain the master equation

$$\begin{aligned}
\frac{d\rho_{mm}(t)}{dt} =& -i\frac{\lambda_\nu^2}{4}A_-(m+2)A_+(m)\rho_{mm}(t)\langle B(E_m - E_{m+2} + i\eta)\rangle \\
&- i\frac{\lambda_\nu^2}{4}A_+(m-2)A_-(m)\rho_{mm}(t)\langle B(E_m - E_{m-2} + i\eta)\rangle \\
&- i\frac{\lambda_\nu^2}{4}A_-(m+2)A_+(m)\rho_{(m+2)(m+2)}(t)\langle B(E_{m+2} - E_m - i\eta)\rangle \\
&- i\frac{\lambda_\nu^2}{4}A_+(m-2)A_-(m)\rho_{(m-2)(m-2)}(t)\langle B(E_{m-2} - E_m - i\eta)\rangle \\
&+ i\frac{\lambda_\nu^2}{4}A_-(m+2)A_+(m)\rho_{(m+2)(m+2)}(t)\langle B(E_{m+2} - E_m + i\eta)\rangle \\
&+ i\frac{\lambda_\nu^2}{4}A_+(m-2)A_-(m)\rho_{(m-2)(m-2)}(t)\langle B(E_{m-2} - E_m + i\eta)\rangle \\
&+ i\frac{\lambda_\nu^2}{4}A_-(m+2)A_+(m)\rho_{mm}(t)\langle B(E_m - E_{m+2} - i\eta)\rangle \\
&+ i\frac{\lambda_\nu^2}{4}A_+(m-2)A_-(m)\rho_{mm}(t)\langle B(E_m - E_{m-2} - i\eta)\rangle. \quad \text{(B.48)}
\end{aligned}$$

And including the expression of the correlation functions:

$$\begin{aligned}
\frac{d\rho_{mm}(t)}{dt} =& -2\pi\frac{\lambda_\nu^2}{4}A_-(m+2)A_+(m)\rho_{mm}(t)n_{BE}\delta\left(E_m - E_{m+2} + \omega_\nu\right) \\
&- 2\pi\frac{\lambda_\nu^2}{4}A_-(m+2)A_+(m)\rho_{mm}(t)\left(n_{BE}+1\right)\delta\left(E_m - E_{m+2} - \omega_\nu\right) \\
&- 2\pi\frac{\lambda_\nu^2}{4}A_+(m-2)A_-(m)\rho_{mm}(t)n_{BE}\delta\left(E_m - E_{m-2} + \omega_\nu\right) \\
&- 2\pi\frac{\lambda_\nu^2}{4}A_+(m-2)A_-(m)\rho_{mm}(t)\left(n_{BE}+1\right)\delta\left(E_m - E_{m-2} - \omega_\nu\right) \\
&+ 2\pi\frac{\lambda_\nu^2}{4}A_-(m+2)A_+(m)\rho_{(m+2)(m+2)}(t)n_{BE}\delta\left(E_{m+2} - E_m + \omega_\nu\right) \\
&+ 2\pi\frac{\lambda_\nu^2}{4}A_-(m+2)A_+(m)\rho_{(m+2)(m+2)}(t)\left(n_{BE}+1\right)\delta\left(E_{m+2} - E_m - \omega_\nu\right) \\
&+ 2\pi\frac{\lambda_\nu^2}{4}A_+(m-2)A_-(m)\rho_{(m-2)(m-2)}(t)n_{BE}\delta\left(E_{m-2} - E_m + \omega_\nu\right) \\
&+ 2\pi\frac{\lambda_\nu^2}{4}A_+(m-2)A_-(m)\rho_{(m-2)(m-2)}(t)\left(n_{BE}+1\right)\delta\left(E_{m-2} - E_m - \omega_\nu\right), \quad \text{(B.49)}
\end{aligned}$$

where we have used the real part (the diagonal terms are real) of

$$\lim_{\eta\to 0^+}\frac{1}{\omega \pm i\eta} = \mathcal{P}\frac{1}{\omega} \mp i\pi\delta(\omega). \quad \text{(B.50)}$$

At $T = 0$, $n_{BE} = 0$, and thus:

$$\begin{aligned}\frac{d\rho_{mm}(t)}{dt} =& -2\pi\frac{\lambda_\nu^2}{4}A_-(m+2)A_+(m)\rho_{mm}(t)\delta\left(E_m - E_{m+2} - \omega_\nu\right)\\ &-2\pi\frac{\lambda_\nu^2}{4}A_+(m-2)A_-(m)\rho_{mm}(t)\delta\left(E_m - E_{m-2} - \omega_\nu\right)\\ &+2\pi\frac{\lambda_\nu^2}{4}A_-(m+2)A_+(m)\rho_{(m+2)(m+2)}(t)\delta\left(E_{m+2} - E_m - \omega_\nu\right)\\ &+2\pi\frac{\lambda_\nu^2}{4}A_+(m-2)A_-(m)\rho_{(m-2)(m-2)}(t)\delta\left(E_{m-2} - E_m - \omega_\nu\right).\end{aligned} \tag{B.51}$$

Where some of this terms will be zero due to the delta function.

For example, if $S = 1$:

$$\begin{aligned}\frac{d\rho_{11}(t)}{dt} =& -2\pi\lambda_\nu^2\rho_{11}(t)\delta\left(E_1 - E_{-1} - \omega_\nu\right)\\ &+2\pi\lambda_\nu^2\rho_{-1-1}(t)\delta\left(E_{-1} - E_1 - \omega_\nu\right),\end{aligned} \tag{B.52}$$

$$\frac{d\rho_{00}(t)}{dt} = 0, \tag{B.53}$$

$$\begin{aligned}\frac{d\rho_{-1-1}(t)}{dt} =& -2\pi\lambda_\nu^2\rho_{-1-1}(t)\delta\left(E_{-1} - E_1 - \omega_\nu\right)\\ &+2\pi\lambda_\nu^2\rho_{11}(t)\delta\left(E_1 - E_{-1} - \omega_\nu\right).\end{aligned} \tag{B.54}$$

If there is no magnetic field, $E_1 = E_{-1}$, and because ω_ν is a positive energy, the δ factors will be zero and we will not have evolution at all.

If we have a positive magnetic field, it will split the degeneracy between E_1 and E_{-1} so that $E_1 - E_{-1} = 2\mu_B B$:

$$\begin{aligned}\frac{d\rho_{11}(t)}{dt} =& -2\pi\lambda_\nu^2\rho_{11}(t)\delta\left(2\mu_B B - \omega_\nu\right)\\ &+2\pi\lambda_\nu^2\rho_{-1-1}(t)\delta\left(2\mu_B B + \omega_\nu\right),\end{aligned} \tag{B.55}$$

$$\frac{d\rho_{00}(t)}{dt} = 0, \tag{B.56}$$

$$\begin{aligned}\frac{d\rho_{-1-1}(t)}{dt} =& -2\pi\lambda_\nu^2\rho_{-1-1}(t)\delta\left(2\mu_B B + \omega_\nu\right)\\ &+2\pi\lambda_\nu^2\rho_{11}(t)\delta\left(2\mu_B B - \omega_\nu\right).\end{aligned} \tag{B.57}$$

If the splitting matches the phonon energy, $2\mu_B B = \omega_\nu$, only the $\delta(2\mu_B B - \omega_\nu)$ terms will survive, and thus:

$$\frac{d\rho_{11}(t)}{dt} = -2\pi\lambda_\nu^2\rho_{11}(t), \tag{B.58}$$

$$\frac{d\rho_{00}(t)}{dt} = 0, \tag{B.59}$$

$$\frac{d\rho_{-1-1}(t)}{dt} = +2\pi\lambda_\nu^2\rho_{11}(t). \tag{B.60}$$

This means that if the initial state is a pure $m = -1$ state, which is the ground state, $\rho_{11}(t_0) = 0$, therefore, we will not have any evolution. Conversely, if the initial state is a pure $m = 1$ state, this being an excited state, it will relax to the $m = -1$ ground state with a relaxation rate $\Gamma = 2\pi\lambda_\nu^2$.

The scattering rate can be obtained also for $T \neq 0$. In this case the evolution of the diagonal elements of the density matrix is described by:

$$\frac{d\rho_{11}(t)}{dt} = -2\pi\lambda_\nu^2\rho_{11}(t)\,(n_{BE}+1) + 2\pi\lambda_\nu^2\rho_{-1-1}(t)n_{BE}, \tag{B.61}$$

$$\frac{d\rho_{00}(t)}{dt} = 0, \tag{B.62}$$

$$\frac{d\rho_{-1-1}(t)}{dt} = +2\pi\lambda_\nu^2\rho_{11}(t)\,(n_{BE}+1) - 2\pi\lambda_\nu^2\rho_{-1-1}(t)n_{BE}. \tag{B.63}$$

Therefore, now, it is possible to jump from the ground state $m = -1$ to the excited state $m = 1$ by the absorption of a phonon. If we write the three equations in matrix form:

$$\begin{pmatrix} d\rho_{11}/dt \\ d\rho_{00}/dt \\ d\rho_{-1-1}/dt \end{pmatrix} = \begin{pmatrix} -2\pi\lambda_\nu^2(n_{BE}+1) & 0 & 2\pi\lambda_\nu^2 n_{BE} \\ 0 & 0 & 0 \\ 2\pi\lambda_\nu^2(n_{BE}+1) & 0 & -2\pi\lambda_\nu^2 n_{BE} \end{pmatrix} \cdot \begin{pmatrix} \rho_{11} \\ \rho_{00} \\ \rho_{-1-1} \end{pmatrix}. \tag{B.64}$$

The three eigenvalues of the matrix are

$$\lambda_1 = 0,\ \lambda_2 = 0, \text{ and } \lambda_3 = -2\pi\lambda_\nu^2(2n_{BE}+1), \tag{B.65}$$

with eigenvectors

$$v_1 = \begin{pmatrix} 0 \\ 1 \\ 0 \end{pmatrix}, v_2 = \begin{pmatrix} 1 \\ 0 \\ (n_{BE}+1)/n_{BE} \end{pmatrix}, \text{and } v_3 = \begin{pmatrix} 1 \\ 0 \\ -1 \end{pmatrix}. \tag{B.66}$$

Thus, the evolution of the diagonal elements of the density matrix is given by:

$$\begin{pmatrix} \rho_{11}(t) \\ \rho_{00}(t) \\ \rho_{-1-1}(t) \end{pmatrix} = C_1 \begin{pmatrix} 0 \\ 1 \\ 0 \end{pmatrix} + C_2 \begin{pmatrix} 1 \\ 0 \\ \frac{n_{BE}+1}{n_{BE}} \end{pmatrix} + C_3 e^{-2\pi\lambda_\nu^2(2n_{BE}+1)t} \begin{pmatrix} 1 \\ 0 \\ -1 \end{pmatrix}. \tag{B.67}$$

If we prepare the initial condition to have $\rho_{11}(0) = 1$ and $\rho_{00}(0) = \rho_{-1-1}(0) = 0$, the three unknown constants can be obtained, which in this case yields

$$\rho_{11}(t) = \frac{n_{BE}}{2n_{BE}+1} + \frac{n_{BE}+1}{2n_{BE}+1} e^{-2\pi\lambda_\nu^2(2n_{BE}+1)t}, \tag{B.68}$$

$$\rho_{00}(t) = 0, \tag{B.69}$$

$$\rho_{-1-1}(t) = \frac{n_{BE}+1}{2n_{BE}+1} - \frac{n_{BE}+1}{2n_{BE}+1} e^{-2\pi\lambda_\nu^2(2n_{BE}+1)t}. \tag{B.70}$$

Appendix C

Energy renormalization of localized electronic states

In this Appendix we will derive the energy shift that experiences a localized electronic state in the Einstein model. In this case, the energy renormalization of the electronic state can be directly related with the λ parameter. In the Einsten model, with a dispersionless phonon with energy ω_0, the real part of the electron-phonon self-energy of an electron is determined by the λ parameter:

$$\Sigma(\omega) = \lambda \frac{\omega_0}{2} log \left| \frac{\omega - \omega_0}{\omega + \omega_0} \right|. \tag{C.1}$$

The relevant vibrational modes in Fe on MgO/Ag(100) are the localized dispersionless in-plane modes of the iron adatom, which are very soft modes. Therefore, the energy of the localized electronic $3d_{xy}$ state is much higher, and the self-energy can be safely approximated as

$$\Sigma(\omega) \approx -\lambda \frac{\omega_0^2}{\omega} \text{for } \omega \gg \omega_0. \tag{C.2}$$

This makes possible to solve the Dyson equation analytically for the $3d_{xy}$ orbital,

$$\varepsilon = \varepsilon_0 + \Sigma(\varepsilon) = \varepsilon_0 - \lambda \frac{\omega_0^2}{\varepsilon}, \tag{C.3}$$

and obtain the renormalized energy ε in terms of the phonon energy ω_0, the λ parameter and the unperturbed electron energy ε_0:

$$\begin{aligned}\varepsilon &= \frac{\varepsilon_0}{2}\left[1+\sqrt{1-4\lambda\left(\frac{\omega_0}{\varepsilon_0}\right)^2}\right] \\ &\approx \varepsilon_0\left[1-\lambda\left(\frac{\omega_0}{\varepsilon_0}\right)^2\right] \text{ for } |\varepsilon_0| \gg \omega_0. \end{aligned} \tag{C.4}$$

Thus, the shift in energy is

$$\Delta\varepsilon \approx -\varepsilon_0\lambda\left(\frac{\omega_0}{\varepsilon_0}\right)^2 \text{ for } |\varepsilon_0| \gg \omega_0, \tag{C.5}$$

which always moves the energy of the localized state closer to the Fermi level.

Appendix D

Plane wave expansion of LCAO wave functions

In the linear combination of atomic orbitals (LCAO) method the wave function is expressed as

$$\psi_n(\mathbf{r}) = \sum_\mu c_n^\mu \, \phi_\mu(\mathbf{r}). \tag{D.1}$$

Above, μ accounts all indices:

$$\phi_\mu(\mathbf{r}) = \phi_{\alpha,l,m}(\mathbf{r} - \mathbf{R}_I), \tag{D.2}$$

where l and m are the usual quantum numbers of orbital angular momentum, $\mathbf{R}_I$ is the atomic position where the orbital is centered, and α is the orbital index.

The wave function can be then expanded in a Fourier series as

$$\psi_n(\mathbf{r}) = \int \psi_n(\mathbf{G}) e^{i\mathbf{G}\cdot\mathbf{r}} d\mathbf{G}, \tag{D.3}$$

which can be rewritten in terms of the Fourier transform of the atomic orbitals as

$$\psi_n(\mathbf{G}) = \sum_\mu c_n^\mu \phi_\mu(\mathbf{G}) = \sum_\mu c_n^\mu \int \phi_\mu(\mathbf{r}) e^{-i\mathbf{G}\cdot\mathbf{r}} d\mathbf{r}. \tag{D.4}$$

To compute $\phi_\mu(\mathbf{G})$ it is convenient to use the plane wave expansion

$$e^{-i\mathbf{G}\cdot\mathbf{r}} = 4\pi \sum_{l=0}^{\infty} \sum_{m=-l}^{l} (-i)^l j_l(Gr) Y_{lm}(\hat{\mathbf{G}}) Y_{lm}^*(\hat{\mathbf{r}}), \tag{D.5}$$

where j_l is the spherical Bessel function and Y_{lm} are the spherical harmonics. Therefore, writing the radial and angular parts of $\phi_\mu(\mathbf{r})$ explicitly:

$$\phi_\mu(\mathbf{G}) = 4\pi \sum_{l'=0}^{\infty} \sum_{m'=-l'}^{l'} \int \phi_\mu(r) Y_{lm}(\hat{\mathbf{r}}) (-i)^{l'} j_{l'}(Gr) Y_{l'm'}(\hat{\mathbf{G}}) Y^*_{l'm'}(\hat{\mathbf{r}}) d\mathbf{r}. \tag{D.6}$$

The angular part of the integral can be done using the orthogonality of spherical harmonics, which reduces the Fourier transform of the basis orbitals to a radial transformation:

$$\phi_\mu(\mathbf{G}) = 4\pi(-i)^l \int \phi_\mu(r) j_l(Gr) dr Y_{lm}(\hat{\mathbf{G}}). \tag{D.7}$$

Finally, writing all the indices explicitly, the plane wave expansion of an LCAO wave function is given by

$$\psi_n(\mathbf{G}) = \sum_{I,\alpha,l,m} c_n^{I,\alpha,l,m} e^{-i\mathbf{G}\cdot\mathbf{R}_I} \phi_{\alpha,l.m}(G) Y_{lm}(\hat{\mathbf{G}}), \tag{D.8}$$

where

$$\phi_{\alpha,l.m}(G) = 4\pi(-i)^l \int \phi_{\alpha,l.m}(G)(r) j_l(Gr) dr. \tag{D.9}$$

Appendix E

Basis states in second quantization

The multiplet wave functions of the adatom are obtained from a crystal field Hamiltonian in terms of Stevens operators. The Hamiltonian is diagonalized in the basis of total orbital angular momentum and total spin $|M_S, M_L\rangle$. To obtain the second quantization expression of the basis states $|M_S, M_L\rangle$ of the ${}^5D$ term ($S = 2$ and $L = 2$), we have started from the trivial maximum $M_S = 2$ and $M_L = 2$ state given by

$$|2, 2\rangle = c^\dagger_{2\downarrow} c^\dagger_{-2\uparrow} c^\dagger_{-1\uparrow} c^\dagger_{0\uparrow} c^\dagger_{1\uparrow} c^\dagger_{2\uparrow} |0\rangle, \tag{E.1}$$

where subindices denote orbital angular momentum z-projection and spin, respectively, and $|0\rangle$ denotes the state with no d electrons. The order for the operators chosen along the work is placing spin majority operators on the right, with highest orbital angular momentum z-projection on the right. The remaining states can be obtained by applying S_- and L_- operators. All the states are listed below:

$|M_S, M_L\rangle$

$$|\ \ 2,\ \ 2\rangle = c^\dagger_{2\downarrow} c^\dagger_{-2\uparrow} c^\dagger_{-1\uparrow} c^\dagger_{0\uparrow} c^\dagger_{1\uparrow} c^\dagger_{2\uparrow} |0\rangle \tag{E.2}$$

$$|\ \ 1,\ \ 2\rangle = \frac{1}{\sqrt{4}} \Big(c^\dagger_{1\downarrow} c^\dagger_{2\downarrow} c^\dagger_{-2\uparrow} c^\dagger_{-1\uparrow} c^\dagger_{0\uparrow} c^\dagger_{2\uparrow} - c^\dagger_{0\downarrow} c^\dagger_{2\downarrow} c^\dagger_{-2\uparrow} c^\dagger_{-1\uparrow} c^\dagger_{1\uparrow} c^\dagger_{2\uparrow} + c^\dagger_{-1\downarrow} c^\dagger_{2\downarrow} c^\dagger_{-2\uparrow} c^\dagger_{0\uparrow} c^\dagger_{1\uparrow} c^\dagger_{2\uparrow} - c^\dagger_{-2\downarrow} c^\dagger_{2\downarrow} c^\dagger_{-1\uparrow} c^\dagger_{0\uparrow} c^\dagger_{1\uparrow} c^\dagger_{2\uparrow} \Big) |0\rangle \tag{E.3}$$

$$|\ \ 0,\ \ 2\rangle = \frac{1}{\sqrt{6}} \Big(c^\dagger_{0\downarrow} c^\dagger_{1\downarrow} c^\dagger_{2\downarrow} c^\dagger_{-2\uparrow} c^\dagger_{-1\uparrow} c^\dagger_{2\uparrow} - c^\dagger_{-1\downarrow} c^\dagger_{1\downarrow} c^\dagger_{2\downarrow} c^\dagger_{-2\uparrow} c^\dagger_{0\uparrow} c^\dagger_{2\uparrow} \tag{E.4}$$

$$+ c^\dagger_{-2\downarrow}c^\dagger_{1\downarrow}c^\dagger_{2\downarrow}c^\dagger_{-1\uparrow}c^\dagger_{0\uparrow}c^\dagger_{2\uparrow} + c^\dagger_{-1\downarrow}c^\dagger_{0\downarrow}c^\dagger_{2\downarrow}c^\dagger_{-2\uparrow}c^\dagger_{1\uparrow}c^\dagger_{2\uparrow}$$

$$-c^\dagger_{-2\downarrow}c^\dagger_{0\downarrow}c^\dagger_{2\downarrow}c^\dagger_{-1\uparrow}c^\dagger_{1\uparrow}c^\dagger_{2\uparrow} + c^\dagger_{-2\downarrow}c^\dagger_{-1\downarrow}c^\dagger_{2\downarrow}c^\dagger_{0\uparrow}c^\dagger_{1\uparrow}c^\dagger_{2\uparrow}\Big)|0\rangle$$

$$|-1,\ \ 2\rangle = \frac{1}{\sqrt{4}}\Big(c^\dagger_{-1\downarrow}c^\dagger_{0\downarrow}c^\dagger_{1\downarrow}c^\dagger_{2\downarrow}c^\dagger_{-2\uparrow}c^\dagger_{2\uparrow} - c^\dagger_{-2\downarrow}c^\dagger_{0\downarrow}c^\dagger_{1\downarrow}c^\dagger_{2\downarrow}c^\dagger_{-1\uparrow}c^\dagger_{2\uparrow} \tag{E.5}$$

$$+c^\dagger_{-2\downarrow}c^\dagger_{-1\downarrow}c^\dagger_{1\downarrow}c^\dagger_{2\downarrow}c^\dagger_{0\uparrow}c^\dagger_{2\uparrow} - c^\dagger_{-2\downarrow}c^\dagger_{-1\downarrow}c^\dagger_{0\downarrow}c^\dagger_{2\downarrow}c^\dagger_{1\uparrow}c^\dagger_{2\uparrow}\Big)|0\rangle$$

$$|-2,\ \ 2\rangle = c^\dagger_{-2\downarrow}c^\dagger_{-1\downarrow}c^\dagger_{0\downarrow}c^\dagger_{1\downarrow}c^\dagger_{2\downarrow}c^\dagger_{2\uparrow}|0\rangle \tag{E.6}$$

$$|\ \ 2,\ \ 1\rangle = c^\dagger_{1\downarrow}c^\dagger_{-2\uparrow}c^\dagger_{-1\uparrow}c^\dagger_{0\uparrow}c^\dagger_{1\uparrow}c^\dagger_{2\uparrow}|0\rangle \tag{E.7}$$

$$|\ \ 1,\ \ 1\rangle = \frac{1}{\sqrt{4}}\Big(c^\dagger_{1\downarrow}c^\dagger_{2\downarrow}c^\dagger_{-2\uparrow}c^\dagger_{-1\uparrow}c^\dagger_{0\uparrow}c^\dagger_{1\uparrow} - c^\dagger_{0\downarrow}c^\dagger_{1\downarrow}c^\dagger_{-2\uparrow}c^\dagger_{-1\uparrow}c^\dagger_{1\uparrow}c^\dagger_{2\uparrow} \tag{E.8}$$

$$+c^\dagger_{-1\downarrow}c^\dagger_{1\downarrow}c^\dagger_{-2\uparrow}c^\dagger_{0\uparrow}c^\dagger_{1\uparrow}c^\dagger_{2\uparrow} - c^\dagger_{-2\downarrow}c^\dagger_{1\downarrow}c^\dagger_{-1\uparrow}c^\dagger_{0\uparrow}c^\dagger_{1\uparrow}c^\dagger_{2\uparrow}\Big)|0\rangle$$

$$|\ \ 0,\ \ 1\rangle = \frac{1}{\sqrt{6}}\Big(c^\dagger_{0\downarrow}c^\dagger_{1\downarrow}c^\dagger_{2\downarrow}c^\dagger_{-2\uparrow}c^\dagger_{-1\uparrow}c^\dagger_{1\uparrow} - c^\dagger_{-1\downarrow}c^\dagger_{1\downarrow}c^\dagger_{2\downarrow}c^\dagger_{-2\uparrow}c^\dagger_{0\uparrow}c^\dagger_{1\uparrow} \tag{E.9}$$

$$+ c^\dagger_{-2\downarrow}c^\dagger_{1\downarrow}c^\dagger_{2\downarrow}c^\dagger_{-1\uparrow}c^\dagger_{0\uparrow}c^\dagger_{1\uparrow} + c^\dagger_{-1\downarrow}c^\dagger_{0\downarrow}c^\dagger_{1\downarrow}c^\dagger_{-2\uparrow}c^\dagger_{1\uparrow}c^\dagger_{2\uparrow}$$

$$-c^\dagger_{-2\downarrow}c^\dagger_{0\downarrow}c^\dagger_{1\downarrow}c^\dagger_{-1\uparrow}c^\dagger_{1\uparrow}c^\dagger_{2\uparrow} + c^\dagger_{-2\downarrow}c^\dagger_{-1\downarrow}c^\dagger_{1\downarrow}c^\dagger_{0\uparrow}c^\dagger_{1\uparrow}c^\dagger_{2\uparrow}\Big)|0\rangle$$

$$|-1,\ \ 1\rangle = \frac{1}{\sqrt{4}}\Big(c^\dagger_{-1\downarrow}c^\dagger_{0\downarrow}c^\dagger_{1\downarrow}c^\dagger_{2\downarrow}c^\dagger_{-2\uparrow}c^\dagger_{1\uparrow} - c^\dagger_{-2\downarrow}c^\dagger_{0\downarrow}c^\dagger_{1\downarrow}c^\dagger_{2\downarrow}c^\dagger_{-1\uparrow}c^\dagger_{1\uparrow} \tag{E.10}$$

$$+c^\dagger_{-2\downarrow}c^\dagger_{-1\downarrow}c^\dagger_{1\downarrow}c^\dagger_{2\downarrow}c^\dagger_{0\uparrow}c^\dagger_{1\uparrow} - c^\dagger_{-2\downarrow}c^\dagger_{-1\downarrow}c^\dagger_{0\downarrow}c^\dagger_{1\downarrow}c^\dagger_{1\uparrow}c^\dagger_{2\uparrow}\Big)|0\rangle$$

$$|-2,\ \ 1\rangle = c^\dagger_{-2\downarrow}c^\dagger_{-1\downarrow}c^\dagger_{0\downarrow}c^\dagger_{1\downarrow}c^\dagger_{2\downarrow}c^\dagger_{1\uparrow}|0\rangle \tag{E.11}$$

$$|\ \ 0,\ \ 2\rangle = c^\dagger_{0\downarrow}c^\dagger_{-2\uparrow}c^\dagger_{-1\uparrow}c^\dagger_{0\uparrow}c^\dagger_{1\uparrow}c^\dagger_{2\uparrow}|0\rangle$$

$$|\ \ 1,\ \ 0\rangle = \frac{1}{\sqrt{4}}\Big(c^\dagger_{0\downarrow}c^\dagger_{2\downarrow}c^\dagger_{-2\uparrow}c^\dagger_{-1\uparrow}c^\dagger_{0\uparrow}c^\dagger_{1\uparrow} - c^\dagger_{0\downarrow}c^\dagger_{1\downarrow}c^\dagger_{-2\uparrow}c^\dagger_{-1\uparrow}c^\dagger_{0\uparrow}c^\dagger_{2\uparrow} \tag{E.12}$$

$$+c^\dagger_{-1\downarrow}c^\dagger_{0\downarrow}c^\dagger_{-2\uparrow}c^\dagger_{0\uparrow}c^\dagger_{1\uparrow}c^\dagger_{2\uparrow} - c^\dagger_{-2\downarrow}c^\dagger_{0\downarrow}c^\dagger_{-1\uparrow}c^\dagger_{0\uparrow}c^\dagger_{1\uparrow}c^\dagger_{2\uparrow}\Big)|0\rangle$$

$$|\ \ 0,\ \ 0\rangle = \frac{1}{\sqrt{6}}\Big(c^\dagger_{0\downarrow}c^\dagger_{1\downarrow}c^\dagger_{2\downarrow}c^\dagger_{-2\uparrow}c^\dagger_{-1\uparrow}c^\dagger_{0\uparrow} - c^\dagger_{-1\downarrow}c^\dagger_{0\downarrow}c^\dagger_{2\downarrow}c^\dagger_{-2\uparrow}c^\dagger_{0\uparrow}c^\dagger_{1\uparrow} \tag{E.13}$$

$$+c^\dagger_{-2\downarrow}c^\dagger_{0\downarrow}c^\dagger_{2\downarrow}c^\dagger_{-1\uparrow}c^\dagger_{0\uparrow}c^\dagger_{1\uparrow} + c^\dagger_{-1\downarrow}c^\dagger_{0\downarrow}c^\dagger_{1\downarrow}c^\dagger_{-2\uparrow}c^\dagger_{0\uparrow}c^\dagger_{2\uparrow}$$

$$-c^\dagger_{-2\downarrow}c^\dagger_{0\downarrow}c^\dagger_{1\downarrow}c^\dagger_{-1\uparrow}c^\dagger_{0\uparrow}c^\dagger_{2\uparrow} + c^\dagger_{-2\downarrow}c^\dagger_{-1\downarrow}c^\dagger_{0\downarrow}c^\dagger_{0\uparrow}c^\dagger_{1\uparrow}c^\dagger_{2\uparrow}\Big)|0\rangle$$

$$|-1,\ \ 0\rangle = \frac{1}{\sqrt{4}}\Big(c^\dagger_{-1\downarrow}c^\dagger_{0\downarrow}c^\dagger_{1\downarrow}c^\dagger_{2\downarrow}c^\dagger_{-2\uparrow}c^\dagger_{0\uparrow} - c^\dagger_{-2\downarrow}c^\dagger_{0\downarrow}c^\dagger_{1\downarrow}c^\dagger_{2\downarrow}c^\dagger_{-1\uparrow}c^\dagger_{0\uparrow} \tag{E.14}$$

$$+c^\dagger_{-2\downarrow}c^\dagger_{-1\downarrow}c^\dagger_{0\downarrow}c^\dagger_{2\downarrow}c^\dagger_{0\uparrow}c^\dagger_{1\uparrow} - c^\dagger_{-2\downarrow}c^\dagger_{-1\downarrow}c^\dagger_{0\downarrow}c^\dagger_{1\downarrow}c^\dagger_{0\uparrow}c^\dagger_{2\uparrow}\Big)|0\rangle$$

$$|-2,\quad 0\rangle = c^\dagger_{-2\downarrow}c^\dagger_{-1\downarrow}c^\dagger_{0\downarrow}c^\dagger_{1\downarrow}c^\dagger_{2\downarrow}c^\dagger_{0\uparrow}|0\rangle \tag{E.15}$$

$$|-1,\quad 2\rangle = c^\dagger_{-1\downarrow}c^\dagger_{-2\uparrow}c^\dagger_{-1\uparrow}c^\dagger_{0\uparrow}c^\dagger_{1\uparrow}c^\dagger_{2\uparrow}|0\rangle$$

$$\begin{aligned}|\quad 1,-1\rangle = \frac{1}{\sqrt{4}}\Big(&c^\dagger_{-1\downarrow}c^\dagger_{2\downarrow}c^\dagger_{-2\uparrow}c^\dagger_{-1\uparrow}c^\dagger_{0\uparrow}c^\dagger_{1\uparrow} - c^\dagger_{-1\downarrow}c^\dagger_{1\downarrow}c^\dagger_{-2\uparrow}c^\dagger_{-1\uparrow}c^\dagger_{0\uparrow}c^\dagger_{2\uparrow}\\ &+c^\dagger_{-1\downarrow}c^\dagger_{0\downarrow}c^\dagger_{-2\uparrow}c^\dagger_{-1\uparrow}c^\dagger_{1\uparrow}c^\dagger_{2\uparrow} - c^\dagger_{-2\downarrow}c^\dagger_{-1\downarrow}c^\dagger_{-1\uparrow}c^\dagger_{0\uparrow}c^\dagger_{1\uparrow}c^\dagger_{2\uparrow}\Big)|0\rangle\end{aligned} \tag{E.16}$$

$$\begin{aligned}|\quad 0,-1\rangle = \frac{1}{\sqrt{6}}\Big(&c^\dagger_{-1\downarrow}c^\dagger_{1\downarrow}c^\dagger_{2\downarrow}c^\dagger_{-2\uparrow}c^\dagger_{-1\uparrow}c^\dagger_{0\uparrow} - c^\dagger_{-1\downarrow}c^\dagger_{0\downarrow}c^\dagger_{2\downarrow}c^\dagger_{-2\uparrow}c^\dagger_{-1\uparrow}c^\dagger_{1\uparrow}\\ &+c^\dagger_{-2\downarrow}c^\dagger_{-1\downarrow}c^\dagger_{2\downarrow}c^\dagger_{-1\uparrow}c^\dagger_{0\uparrow}c^\dagger_{1\uparrow} + c^\dagger_{-1\downarrow}c^\dagger_{0\downarrow}c^\dagger_{1\downarrow}c^\dagger_{-2\uparrow}c^\dagger_{-1\uparrow}c^\dagger_{2\uparrow}\\ &-c^\dagger_{-2\downarrow}c^\dagger_{-1\downarrow}c^\dagger_{1\downarrow}c^\dagger_{-1\uparrow}c^\dagger_{0\uparrow}c^\dagger_{2\uparrow} + c^\dagger_{-2\downarrow}c^\dagger_{-1\downarrow}c^\dagger_{0\downarrow}c^\dagger_{-1\uparrow}c^\dagger_{1\uparrow}c^\dagger_{2\uparrow}\Big)|0\rangle\end{aligned} \tag{E.17}$$

$$\begin{aligned}|-1,-1\rangle = \frac{1}{\sqrt{4}}\Big(&c^\dagger_{-1\downarrow}c^\dagger_{0\downarrow}c^\dagger_{1\downarrow}c^\dagger_{2\downarrow}c^\dagger_{-2\uparrow}c^\dagger_{-1\uparrow} - c^\dagger_{-2\downarrow}c^\dagger_{-1\downarrow}c^\dagger_{1\downarrow}c^\dagger_{2\downarrow}c^\dagger_{-1\uparrow}c^\dagger_{0\uparrow}\\ &+c^\dagger_{-2\downarrow}c^\dagger_{-1\downarrow}c^\dagger_{0\downarrow}c^\dagger_{2\downarrow}c^\dagger_{-1\uparrow}c^\dagger_{1\uparrow} - c^\dagger_{-2\downarrow}c^\dagger_{-1\downarrow}c^\dagger_{0\downarrow}c^\dagger_{1\downarrow}c^\dagger_{-1\uparrow}c^\dagger_{2\uparrow}\Big)|0\rangle\end{aligned} \tag{E.18}$$

$$|-2,-1\rangle = c^\dagger_{-2\downarrow}c^\dagger_{-1\downarrow}c^\dagger_{0\downarrow}c^\dagger_{1\downarrow}c^\dagger_{2\downarrow}c^\dagger_{-1\uparrow}|0\rangle \tag{E.19}$$

$$|-2,\quad 2\rangle = c^\dagger_{-2\downarrow}c^\dagger_{-2\uparrow}c^\dagger_{-1\uparrow}c^\dagger_{0\uparrow}c^\dagger_{1\uparrow}c^\dagger_{2\uparrow}|0\rangle$$

$$\begin{aligned}|\quad 1,-2\rangle = \frac{1}{\sqrt{4}}\Big(&c^\dagger_{-2\downarrow}c^\dagger_{2\downarrow}c^\dagger_{-2\uparrow}c^\dagger_{-1\uparrow}c^\dagger_{0\uparrow}c^\dagger_{1\uparrow} - c^\dagger_{-2\downarrow}c^\dagger_{1\downarrow}c^\dagger_{-2\uparrow}c^\dagger_{-1\uparrow}c^\dagger_{0\uparrow}c^\dagger_{2\uparrow}\\ &+c^\dagger_{-2\downarrow}c^\dagger_{0\downarrow}c^\dagger_{-2\uparrow}c^\dagger_{-1\uparrow}c^\dagger_{1\uparrow}c^\dagger_{2\uparrow} - c^\dagger_{-2\downarrow}c^\dagger_{-1\downarrow}c^\dagger_{-2\uparrow}c^\dagger_{0\uparrow}c^\dagger_{1\uparrow}c^\dagger_{2\uparrow}\Big)|0\rangle\end{aligned} \tag{E.20}$$

$$\begin{aligned}|\quad 0,-2\rangle = \frac{1}{\sqrt{6}}\Big(&c^\dagger_{-2\downarrow}c^\dagger_{1\downarrow}c^\dagger_{2\downarrow}c^\dagger_{-2\uparrow}c^\dagger_{-1\uparrow}c^\dagger_{0\uparrow} - c^\dagger_{-2\downarrow}c^\dagger_{0\downarrow}c^\dagger_{2\downarrow}c^\dagger_{-2\uparrow}c^\dagger_{-1\uparrow}c^\dagger_{1\uparrow}\\ &+c^\dagger_{-2\downarrow}c^\dagger_{-1\downarrow}c^\dagger_{2\downarrow}c^\dagger_{-2\uparrow}c^\dagger_{0\uparrow}c^\dagger_{1\uparrow} + c^\dagger_{-2\downarrow}c^\dagger_{0\downarrow}c^\dagger_{1\downarrow}c^\dagger_{-2\uparrow}c^\dagger_{-1\uparrow}c^\dagger_{2\uparrow}\\ &-c^\dagger_{-2\downarrow}c^\dagger_{-1\downarrow}c^\dagger_{1\downarrow}c^\dagger_{-2\uparrow}c^\dagger_{0\uparrow}c^\dagger_{2\uparrow} + c^\dagger_{-2\downarrow}c^\dagger_{-1\downarrow}c^\dagger_{0\downarrow}c^\dagger_{-2\uparrow}c^\dagger_{1\uparrow}c^\dagger_{2\uparrow}\Big)|0\rangle\end{aligned} \tag{E.21}$$

$$\begin{aligned}|-1,-2\rangle = \frac{1}{\sqrt{4}}\Big(&c^\dagger_{-2\downarrow}c^\dagger_{0\downarrow}c^\dagger_{1\downarrow}c^\dagger_{2\downarrow}c^\dagger_{-2\uparrow}c^\dagger_{-1\uparrow} - c^\dagger_{-2\downarrow}c^\dagger_{-1\downarrow}c^\dagger_{1\downarrow}c^\dagger_{2\downarrow}c^\dagger_{-2\uparrow}c^\dagger_{0\uparrow}\\ &+c^\dagger_{-2\downarrow}c^\dagger_{-1\downarrow}c^\dagger_{0\downarrow}c^\dagger_{2\downarrow}c^\dagger_{-2\uparrow}c^\dagger_{1\uparrow} - c^\dagger_{-2\downarrow}c^\dagger_{-1\downarrow}c^\dagger_{0\downarrow}c^\dagger_{1\downarrow}c^\dagger_{-2\uparrow}c^\dagger_{2\uparrow}\Big)|0\rangle\end{aligned} \tag{E.22}$$

$$|-2,-2\rangle = c^\dagger_{-2\downarrow}c^\dagger_{-1\downarrow}c^\dagger_{0\downarrow}c^\dagger_{1\downarrow}c^\dagger_{2\downarrow}c^\dagger_{-2\uparrow}|0\rangle \tag{E.23}$$

Laburpena

Gero eta teknologikoagoa den gizarte batak oinarrizko ikerketa bultzatu du gaur egun dugun datuak gordetzeko eta prozesatzeko teknologia murrizte aldera. Bilaketa honek eskala nanometrikoa lortu du azken hamarkadetan fabrikazio tekniken aurrerapenari esker. Hala ere, egungo teknologiaren muga fisikoak direla eta, azken urteotan moteldu egin da Moore-ren legeak aurreikusitako eskalatzea. Bitartean, ikerketa zientifikoaren funtsezko eginkizuna alternatibak aztertzea da, gaur egun ezarritako erdieroaleen teknologiatik at, datuen tratamenduaren arloan paradigma berri bat eskainiko dutela espero delarik. Testuinguru honetan, eskala atomikoko egiturek informazioa gordetzeko eta prozesatzeko materia-unitate txikiena adierazten dute. Hala ere, etorkizun handiko teknologiak, hala nola konputazio kuantikoa, mekanika kuantikoaren printzipioetan oinarritzen diren arren, fenomeno kuantikoak agertzeak erronka handia suposatzen du eskala atomikoko egituren kontrol eta manipulaziorako.

Tamaina atomikoko egiturak, esate baterako kate atomikoak edo atomo magnetiko bakarrak, hautagai itxaropentsuak dira besteak beste datuak gordetzeko gailuak eta bit kuantikoak egiteko, hauek dituzten bizi-itxaropen luzeko egoera kuantiko magnetikoak direla etas [1–12]. Alderdi honetan, atomo bakar magnetikoek aparteko eszenatokia eskaintzen dute hainbat fenomeno interesgarri aztertzeko, hala nola, kitzikapen magnetikoak [13–16], elkarrekintza magnetikoak [17–19] edo espin erlaxazioa eta dekoherentzia [6, 8, 12]. Ildo horretan, aurrerapen nabarmenak lortu dira nanoegiturak manipulatzeko eta aztertzeko puntako teknika esperimentalen garapenari esker. Bereziki, espin-polarizatutako tunel-efektuko mikroskopiaren eta espektroskopiaren [6, 8, 13, 16, 18, 20–30], X izpien dikroismo magnetiko zirkularren [4, 9, 27, 31–33] eta erresonantzia paramagnetiko elektronikoaren [3, 7, 10, 30, 34–41] gorakadak ikerketalan aitzindariak bultzatu ditu. Gainera, metodo teoriko berrien garapenak eta konputazio-ahalmenaren hobekuntzak arlo honetan azterketa teoriko

zehatzak egiteko aukera ere eman du [5, 42–55].

Arloko punta-puntako ikerketa atomo bakar magnetikoen sistemak karakterizatzera eta espin-dinamikan parte hartzen duten mekanismo fisikoak ulertzera bideratua dago, azken helburua atomo bakarren kontrola eta egonkortasuna lortzea delarik. Egonkortasun magnetikoa, funtsean, atomoaren egitura magnetikoak zehazten du, ingurunearekin duen elkarrekintzarekin batera [12]. Atomo bakarren sistemetako oinarrizko egoera eta egoera magnetiko kitzikatuak bereizten dituen energia handiak, anisotropia energia magnetikoa deritzona, magnetizazioaren alderantzikatzea fluktuazio termikoetatik babesten du [21, 26, 27, 56, 57]. Hala ere, nanoegitura hauen izaera kuantikoak berezko fluktuazio kuantikoak sortzen ditu [50] eta magnetizazioaren tunel efektu kuantikoa ahalbidetzen du [58, 59], egoera magnetikoak desegonkortu eta espin erlaxazioa eragin ohi dutenak.

Atomo bakarren sistemen momentu magnetiko txikiak direla eta, haien ingurunearekiko elkarrekintzak ere funtsezko zeregina dute beren espin-dinamikan. Substratu-eroaleko elektroiekiko elkarrekintzak momentu magnetiko lokalizatua apantailatu dezake eta haren egonkortasunean eragin, Kondo efektua bezala ezagutzen dena [17, 60, 61]. Substratuko elektroien eragina murrizteko, Cu_2N, MgO edo grafenoa bezalako geruza isolatzaileak arrakastaz erabili dira, atomo bakarren egoera magnetikoak egonkortuz eta espin erlaxazio denbora luzeak lortuz [4, 11, 14]. Neurketak egiteko erabiltzen diren tunel-elektroien eragina ere esperimentalki aztertua izan da [6], baita akoplamenduaren jatorri fisikoa teorikoki aztertu ere [43, 44]. Erresonantzia paramagnetiko elektronikoaren kasuan, hainbat eredu teoriko proposatu diren arren erresonantzia trantsizioen atzean dagoen funtsezko fisika ulertu nahian [38, 53], espin trantsizioen jatorria oraindik ezezaguna dugu [41]. Bestalde, interakzio elektronikoek atomo bakarren propietateetan duten eragina oso ikertua izan den arren, substratuko bibrazioen rolak askoz ere arreta gutxiago jaso du orain arte. Dena den, askotan espekulatu da elektroi-fonoi elkarrekintzak espin erlaxazio mekanismo gisa duen eginkizun erabakigarriari buruz, eta, hain zuzen ere, erlaxazio mekanismoan duten garrantziaren zantzu argiak ere aurkitu dira [62].

Elektroi-fonoi elkarrekintza deritzona, funtsean, fonoiek egitura elektronikoan duten eragina da. Funtsezko papera betetzen du hainbat fenomeno fisikotan, hala nola metalen eroankortasun elektrikoan eta erresistibitatean, garraiolarien mugikortasunaren tenperaturaren menpekotasunean, erdieroaleen propietate optikoetan edo baita ohiko supereroanko-

rtasunean ere. Ondorioz, egoera solidoaren fisikaren gai klasikoetako bat adierazten du eta teoria kuantikoaren lehen egunetatik sakon aztertua izan da [63–68]. Hala ere, elkarrekintza hau zehaztasunez modelatzeko beharrezkoak diren konputazio-kostu handiak direla eta, elektroi-fonoi elkarreraginaren lehen printzipioetako kalkulu kuantitatiboak duela gutxi baino ez dira eskuragarri izan [69].

Zentzu honetan, atomo bakar magnetikoen espin-bizitzaren eta trantsizio-tasen lehen printzipioetako kalkuluak egiteko zailtasunak neurketa esperimentaletan parte hartzen duten mekanismo fisikoen jatorria egiaztatzea zailtzen du. Izan ere, lehen printzipioetatik elektroi-fonoi akoplamenduaren ekarpena aztertzeko metodo teoriko sendorik ez da aurkitu orain arte, atomo bakarren gorputz anitzeko izaera eta gainazaleko simulazio batean atomo kopuru handia adierazten duen erronka konputazionala dela eta. Iman molekularren alorrean, espin-fonoi akoplamenduaren lehen printzipioetako hainbat kalkulu egin izan dira kimika kuantikoan garatutako egitura elektronikoko metodo konplexuak erabiliz [70–77]. Metodo hauek molekula magnetiko ez-periodikoen gorputz anitzeko izaeraren deskribapen zehatza ahalbidetzen dute, baina, kostu konputazionalak direla eta, atomo bakarren super-gelaxka sistemetan aplikatzea ez da bideragarria.

Tesi honetan, zenbait zenbakizko-metodo garatu eta aplikatu ditugu elektroi-fonoi elkarreraginak atomo bakar magnetikoetan dituen ondorioak lehen printzipioetatik kontuan hatzeko asmoz. Bereziki, bibrazioek MgO/Ag(100) gainean metatutako Fe atomo bakarrean duten eragina aztertzen dugu. Gure kalkuluek lehendik dauden emaitza esperimentalak ezagutzeko eta ikerkuntza lerro berriak irekitzeko aukera ematen dute atomo bakar magnetikoen espin-bizitzaren azterketan.

Elektroi-fonoi elkarrekintzaren eragina Fe/MgO/Ag(100) sistemaren egoera elektronikoetan

Atomo magnetiko bakarren egitura magnetikoa oso aztertua izan da teknika esperimentalak erabiliz, baita espin Hamiltondar eredu teorikoak edota lehen printzipioetako kalkuluak erabiliz ere [12, 42, 44, 45, 52, 54]. Ikerketa hauek atomo bakarren egitura magnetikoaren ulermena hobetzen lagundu dute. Horrez gain, atomo bakarrek ingurunearekin duten elkarrekintza aztertzeak azpian dagoen fisikaren ulermen sakonagoa

ere ahalbidetu du. Bereziki, substratuaren egoera elektronikoen eragina aztertzeak atomo bakarretan bizi-denbora luzeko egoera kuantiko magnetikoak aurkitzea ahalbidetu du. Horretarako, substratuaren kristaleremuak egitura elektronikoan duen eragina aztertu da, anisotropia energia magnetikoa handituz [2, 27, 88], eta substratuko elektroiekiko elkarrekintza murriztu da, MgO bezalako geruza isolatzaileak erabiliz [4, 21].

Atomo bakar magnetikoetan elkarrekintza elektronikoak duen eragina sakonki aztertu den arren [9, 17, 21, 26, 27, 31, 42, 46, 47, 54, 56, 88–92], elektroi-fonoi elkarrekintzak propietate magnetikoetan duen eraginari buruzko ikerketak askoz arreta gutxiago erakarri du. Ezberdintasun horren arrazoia atomo kopuru handia duen super-gelaxka sistema batean elektroi-fonoi elkarrekintzaren kalkuluak aurkezten duen erronka izan delarik.

Egoera honi aurre egiteko, Fe/MgO/Ag(100) atomo bakar magnetiko sisteman elektroi-fonoi elkarrekintzak egitura elektronikoan duen eragina aztertu dugu. Horretarako, sistemaren egitura elektronikoa eta bibrazionala kalkulatu ditugu lehen printzipioetatik, zilar substratuak elektroien sakabanatze prozesuan duen garrantzia azpimarratuz. Ondoren, elektroi-fonoi akoplamenduaren indarra kalkulatu dugu. Eliashberg funtzioa erabiliz frogatu dugu burdin atomoaren planoko oszilazioak direla sistemako bibrazio-modu garrantzitsuenak, aurretik Ho atomo bakarreko sisteman aurkitutakoarekin bat datorrelarik [62]. Gainera, kalkulatutako λ parametroak eta kuasipartikulen bizi-denborak elektroi-fonoi elkarrekintzak MgO geruzen kopuru bikoitientzat eta bakoitientzat desberdintasun kualitatiboak dituela erakusten du. MgO estaldura bikoitien eta bakoitien arteko ezberdintasun hau substratuak duen gainazal-egoera batek eragiten du, MgO-ren estaldura bakoitietarako sakabanaketa kanal garrantzitsuena dena; bere ekarpena sakabanaketa-tasa osoaren % 70 da 3 ML estalduraren kasuan, MgO geruza kopuru bikoitientzat, berriz, bere ekarpena asko murrizten delarik. Azkenik, emaitza nagusi gisa, gure kalkuluek MgO geruza bakarraren kasuan burdin atomoak pairatzen duen elektroi-fonoi elkarrekintza ohiko materialen artean aurkitutako elektroi-fonoi elkarrekintza indartsuenaren parekoa dela erakusten dute, MgO estaldura handiagoen kasuan elektroi-fonoi sakabanaketa sakonki ezabatzen delarik. Hori dela eta, MgO geruza bakarra ez dela elektroi-fonoi elkarrekintza modu eraginkorrean bahetzeko gai ondorioztatu dezakegu.

Fe/MgO/Ag(100) sisteman bibrazioek eragindako espin-erlaxazioa

Nanoegiturak manipulatzeko eta aztertzeko teknika esperimentalen garapenarekin, atomo bakar magnetikoek espin dinamika eta erlaxazioa eskala atomikoan aztertzeko aparteko eszenatokia eskaintzen dute [6, 8, 12]. Testuinguru horretan, ezinbestekoa da atomo bakarrek beren ingurunearekin duten elkarrekintza ulertzea haien kontrol eta manipulazio teknikak hobetu, eta konputazio kuantikoa bezalako aplikazioetan erabili ahal izateko.

Tunel-efektuko espektroskopiaren hazkuntzarekin [13], eredu teoriko arrakastatsuak proposatu izan dira atzean dagoen funtsezko fisika atzemateko [43, 44]. Geroago erresonantzia paramagnetiko elektronikoaren agerpenak emaitza nabarmenak ahalbidetu ditu bereizmen energian eta espazialean jauzi bat emanez [3, 7, 10, 34–37]. Hala ere, hainbat eredu teoriko proposatu diren arren [38, 41, 53], trantsizioen jatorri fisikoa oraindik ez dago argi. Atomo bakar magnetikoetan aurkitu diren bizi denbora luzeko egoeren kasuan [4, 6, 8], ingurunearekiko elkarrekintzak momentu magnetikoak desegonkortzen dituela jakina den arren, esperimentuetan behatzen diren trantsizio-mekanismoen jatorria egiaztatzea ez da erraza espin-bizitzen eta trantsizio-tasen lehen printzipioen kalkuluak egiteko zailtasuna dela eta.

Elkarrekintza elektronikoek atomo bakarretan duten eragina sakon aztertu izan da lehen printzipioetako kalkuluen laguntzarekin [5, 25, 44–52, 54], baina askoz ere arreta gutxiago jarri zaio substratuaren bibrazioek, hots, fonoiek, duten eraginari. Hala eta guztiz ere, askotan aipatu izan da espin-fonoi akoplamenduaren papera atomo bakarren espin-erlaxazio mekanismo gisa. Iman molekularren alorrean, espin-fonoi akoplamenduaren lehen printzipioetako kalkuluek ibilbide luzea dute [70–77]. Hala ere, gainazaletan jalkitako atomo bakarren kasuan, atomoaren gorputz anitzeko izaerarengatik eta gainazaleko simulazio batean atomo kopuru handiak dakarren erronka konputazionalarengatik, ez da horrelako kalkulurik aurrera eraman gaur arte.

Tesi honetan, lehen printzipioetako dentsitate funtzionalaren teoria kalkuluak multiplete atomiko-eredu batekin konbinatzen dituen metodo bat aurkezten dugu elektroi-fonoi espin erlaxazio denbora aztertzeko. Espin erlaxazio denbora deskribatzeko ekuazio nagusiaren deribazioa aurkeztu dugu, formalismoa Fe/MgO/Ag(100) atomo bakarreko sisteman aplikatuz. Horretarako, burdin atomoaren egitura elektronikoa eta

bibrazionala aztertu ditugu, Stevens Hamiltondar baten bitartez atomo bakarraren multiplete egitura kontuan hartuz. Ondoren, burdin atomoaren espin bizitza aztertu dugu. Gure kalkuluek sistema berean egindako neurketa esperimentalekin adostasun ona erakusten dute bizi denboraren magnitude ordenan, aurkeztutako metodoak arazoaren deskribapen egoki baterako beharrezkoak diren ezaugarri guztiak arrakastaz jasotzen dituela erakutsiz. Horrez gain, gure ereduak espin-fonoi erlaxazio mekanismorako multiplete-egoeren osagai garrantzitsuenak identifikatzea ahalbidetu digu, sistema jakin honetako orbital elektroniko garrantzitsuak zein diren agerian utziz. Gainera, kristal-eremuak espin bizitzan duen eragina aztertu dugu, etorkizunean espin erlaxazio denbora luzeagoak dituzten sistemak diseinatzen lagundu dezakeena. Azkenik, esperimentuetan aplikatutako kanpoko eremu magnetikoak espin-bizitzan duen eragina aztertu dugu. Esperimentuetan kontuan hartutako eremu magnetikoetarako, burdinaren bibrazio modu lokalizatuek zein MgO substratuko fonoiek espin-bizitzan eragin antzekoa dutela erakutsiz, eta beraz, substratuaren deskribapen zuzena ere ezinbestekoa dela erakutsiz. Gure kalkuluek espin-bizitzaren saturazioa ere erakusten du Zeeman banaketak burdin atomoaren planoko modu lokalen energiarekin bat egiten duenean. Azken hau hatz-marka argia izan daiteke erlaxazio-prozesuan espin-fonoi elkarrekintzaren ekarpen nagusi bat dagoela esperimentalki identifikatu ahal izateko.

Azken ondorio gisa, tesi honetan atomo bakar magnetikoen alorrean ikerketa berri bat aurkeztu dugu, lehen printzipioetako metodoak garatuz eta aplikatuz, elektroi-fonoi akoplamenduak espin erlaxazio mekanismoan duen eginkizuna aztertzeko.

Publications

- *Electron-phonon coupling of Fe-adatom electron states on MgO/Ag(100)*,
  Haritz Garai-Marin, Julen Ibañez-Azpiroz, Peio Garcia-Goiricelaya, Idoia G. Gurtubay and Asier Eiguren,
  Physical Review B **104**, 195422 (2021).

- *Microscopic theory of spin-relaxation of a single Fe adatom coupled to substrate vibrations*,
  Haritz Garai-Marin, Manuel dos Santos Dias, Samir Lounis, Julen Ibañez-Azpiroz and Asier Eiguren,
  Submitted: arXiv:2212.09653

Bibliography

[1] S. Loth, S. Baumann, C. P. Lutz, D. M. Eigler, and A. J. Heinrich, Science **335**, 196 (2012).

[2] T. Miyamachi, T. Schuh, T. Märkl, C. Bresch, T. Balashov, A. Stöhr, C. Karlewski, S. André, M. Marthaler, M. Hoffmann, M. Geilhufe, S. Ostanin, W. Hergert, I. Mertig, G. Schön, A. Ernst, and W. Wulfhekel, Nature **503**, 242 (2013).

[3] S. Baumann, W. Paul, T. Choi, C. P. Lutz, A. Ardavan, and A. J. Heinrich, Science **350**, 417 (2015).

[4] F. Donati, S. Rusponi, S. Stepanow, C. Wäckerlin, A. Singha, L. Persichetti, R. Baltic, K. Diller, F. Patthey, E. Fernandes, J. Dreiser, Šljivančanin, K. Kummer, C. Nistor, P. Gambardella, and H. Brune, Science **352**, 318 (2016).

[5] J. Hermenau, J. Ibañez-Azpiroz, C. Hübner, A. Sonntag, B. Baxevanis, K. T. Ton, M. Steinbrecher, A. A. Khajetoorians, M. dos Santos Dias, S. Blügel, R. Wiesendanger, S. Lounis, and J. Wiebe, Nature Communications **8**, 642 (2017).

[6] W. Paul, K. Yang, S. Baumann, N. Romming, T. Choi, C. P. Lutz, and A. J. Heinrich, Nature Physics **13**, 403 (2017).

[7] F. D. Natterer, K. Yang, W. Paul, P. Willke, T. Choi, T. Greber, A. J. Heinrich, and C. P. Lutz, Nature **543**, 226 (2017), arXiv:1607.03977 .

[8] F. D. Natterer, F. Donati, F. Patthey, and H. Brune, Physical Review Letters **121**, 027201 (2018), arXiv:1712.07871 .

[9] R. Baltic, F. Donati, A. Singha, C. Wäckerlin, J. Dreiser, B. Delley, M. Pivetta, S. Rusponi, and H. Brune, Physical Review B **98**, 024412 (2018).

[10] K. Yang, W. Paul, S. H. Phark, P. Willke, Y. Bae, T. Choi, T. Esat, A. Ardavan, A. J. Heinrich, and C. P. Lutz, Science **366**, 509 (2019).

[11] V. Bellini, S. Rusponi, J. Kolorenč, S. K. Mahatha, M. A. Valbuena, L. Persichetti, M. Pivetta, B. V. Sorokin, D. Merk, S. Reynaud, D. Sblendorio, S. Stepanow, C. Nistor, P. Gargiani, D. Betto, A. Mugarza, P. Gambardella, H. Brune, C. Carbone, and A. Barla, ACS Nano **16**, 11182 (2022).

[12] F. Delgado and J. Fernández-Rossier, Progress in Surface Science **92**, 40 (2017).

[13] A. J. Heinrich, J. A. Gupta, C. P. Lutz, and D. M. Eigler, Science **306**, 466 (2004).

[14] S. Loth, C. P. Lutz, and A. J. Heinrich, New Journal of Physics **12**, 125021 (2010).

[15] M. Ternes, New Journal of Physics **17**, 063016 (2015), arXiv:1505.04430 .

[16] M. Ternes, C. P. Lutz, A. J. Heinrich, and W.-D. Schneider, Physical Review Letters **124**, 167202 (2020).

[17] A. F. Otte, M. Ternes, K. von Bergmann, S. Loth, H. Brune, C. P. Lutz, C. F. Hirjibehedin, and A. J. Heinrich, Nature Physics **4**, 847 (2008).

[18] F. Meier, L. Zhou, J. Wiebe, and R. Wiesendanger, Science **320**, 82 (2008).

[19] J. Bouaziz, J. Ibañez-Azpiroz, F. S. Guimarães, and S. Lounis, Physical Review Research **2**, 043357 (2020).

[20] C. F. Hirjibehedin, C. P. Lutz, and A. J. Heinrich, Science **312**, 1021 (2006).

[21] C. F. Hirjibehedin, C.-Y. Lin, A. F. Otte, M. Ternes, C. P. Lutz, B. A. Jones, and A. J. Heinrich, Science **317**, 1199 (2007).

[22] R. Wiesendanger, Reviews of Modern Physics **81**, 1495 (2009).

[23] S. Loth, K. von Bergmann, M. Ternes, A. F. Otte, C. P. Lutz, and A. J. Heinrich, Nature Physics **6**, 340 (2010).

[24] S. Loth, M. Etzkorn, C. P. Lutz, D. M. Eigler, and A. J. Heinrich, Science **329**, 1628 (2010).

[25] A. A. Khajetoorians, S. Lounis, B. Chilian, A. T. Costa, L. Zhou, D. L. Mills, J. Wiebe, and R. Wiesendanger, Physical Review Letters **106**, 037205 (2011).

[26] F. Donati, Q. Dubout, G. Autès, F. Patthey, F. Calleja, P. Gambardella, O. V. Yazyev, and H. Brune, Physical Review Letters **111**, 236801 (2013).

[27] I. G. Rau, S. Baumann, S. Rusponi, F. Donati, S. Stepanow, L. Gragnaniello, J. Dreiser, C. Piamonteze, F. Nolting, S. Gangopadhyay, O. R. Albertini, R. M. Macfarlane, C. P. Lutz, B. A. Jones, P. Gambardella, A. J. Heinrich, and H. Brune, Science **344**, 988 (2014).

[28] J. Hermenau, M. Ternes, M. Steinbrecher, R. Wiesendanger, and J. Wiebe, Nano Letters **18**, 1978 (2018), arXiv:1712.05350 .

[29] D. Coffey, C. de la Fuente, M. Ciria, D. Serrate, S. Loth, and J. I. Arnaudas, Physical Chemistry Chemical Physics **22**, 196 (2020).

[30] W. M. J. van Weerdenburg, M. Steinbrecher, N. P. E. van Mullekom, J. W. Gerritsen, H. von Allwörden, F. D. Natterer, and A. A. Khajetoorians, Review of Scientific Instruments **92**, 033906 (2021).

[31] F. Donati, L. Gragnaniello, A. Cavallin, F. D. Natterer, Q. Dubout, M. Pivetta, F. Patthey, J. Dreiser, C. Piamonteze, S. Rusponi, and H. Brune, Physical Review Letters **113**, 177201 (2014).

[32] F. Donati, A. Singha, S. Stepanow, C. Wäckerlin, J. Dreiser, P. Gambardella, S. Rusponi, and H. Brune, Physical Review Letters **113**, 237201 (2014).

[33] A. Singha, D. Sostina, C. Wolf, S. L. Ahmed, D. Krylov, L. Colazzo, P. Gargiani, S. Agrestini, W.-S. Noh, J.-H. Park, M. Pivetta, S. Rusponi, H. Brune, A. J. Heinrich, A. Barla, and F. Donati, ACS Nano **15**, 16162 (2021).

[34] P. Willke, Y. Bae, K. Yang, J. L. Lado, A. Ferrón, T. Choi, A. Ardavan, J. Fernández-Rossier, A. J. Heinrich, and C. P. Lutz, Science **362**, 336 (2018).

[35] K. Yang, P. Willke, Y. Bae, A. Ferrón, J. L. Lado, A. Ardavan, J. Fernández-Rossier, A. J. Heinrich, and C. P. Lutz, Nature Nanotechnology **13**, 1120 (2018).

[36] K. Yang, W. Paul, F. D. Natterer, J. L. Lado, Y. Bae, P. Willke, T. Choi, A. Ferrón, J. Fernández-Rossier, A. J. Heinrich, and C. P. Lutz, Physical Review Letters **122**, 227203 (2019).

[37] P. Willke, K. Yang, Y. Bae, A. J. Heinrich, and C. P. Lutz, Nature Physics **15**, 1005 (2019).

[38] T. S. Seifert, S. Kovarik, D. M. Juraschek, N. A. Spaldin, P. Gambardella, and S. Stepanow, Science Advances **6**, 10.1126/SCIADV.ABC5511 (2020), arXiv:2005.07455 .

[39] J. Kim, W.-J. Jang, T. H. Bui, D.-J. Choi, C. Wolf, F. Delgado, Y. Chen, D. Krylov, S. Lee, S. Yoon, C. P. Lutz, A. J. Heinrich, and Y. Bae, Physical Review B **104**, 174408 (2021).

[40] S. Kovarik, R. Robles, R. Schlitz, T. S. Seifert, N. Lorente, P. Gambardella, and S. Stepanow, Nano Letters **22**, 4176 (2022).

[41] F. Delgado and N. Lorente, Progress in Surface Science **96**, 100625 (2021).

[42] P. Lang, V. S. Stepanyuk, K. Wildberger, R. Zeller, and P. H. Dederichs, Solid State Communications **92**, 755 (1994).

[43] J. Fernández-Rossier, Physical Review Letters **102**, 256802 (2009), arXiv:0901.4839 .

[44] N. Lorente and J.-P. Gauyacq, Physical Review Letters **103**, 176601 (2009).

[45] S. Lounis, A. T. Costa, R. B. Muniz, and D. L. Mills, Physical Review Letters **105**, 187205 (2010).

[46] H. X. Yang, M. Chshiev, B. Dieny, J. H. Lee, A. Manchon, and K. H. Shin, Physical Review B **84**, 054401 (2011).

[47] S. Lounis, M. Dos Santos Dias, and B. Schweflinghaus, Physical Review B - Condensed Matter and Materials Physics **91**, 104420 (2015).

[48] A. Ferrón, J. L. Lado, and J. Fernández-Rossier, Physical Review B - Condensed Matter and Materials Physics **92**, 174407 (2015), arXiv:1506.04941 .

[49] A. A. Khajetoorians, M. Steinbrecher, M. Ternes, M. Bouhassoune, M. dos Santos Dias, S. Lounis, J. Wiebe, and R. Wiesendanger, Nature Communications **7**, 10620 (2016).

[50] J. Ibañez-Azpiroz, M. dos Santos Dias, S. Blügel, and S. Lounis, Nano Letters **16**, 4305 (2016).

[51] J. Ibañez-Azpiroz, M. D. S. Dias, B. Schweflinghaus, S. Blügel, and S. Lounis, Physical Review Letters **119**, 017203 (2017), arXiv:1706.02085 .

[52] J. Ibañez-Azpiroz, M. D. S. Dias, S. Blügel, and S. Lounis, Physical Review B **96**, 144410 (2017), arXiv:1708.00280 .

[53] J. Reina Gálvez, C. Wolf, F. Delgado, and N. Lorente, Physical Review B **100**, 035411 (2019), arXiv:1904.08183 .

[54] C. Wolf, F. Delgado, J. Reina, and N. Lorente, Journal of Physical Chemistry A **124**, 2318 (2020), arXiv:1912.09793 .

[55] S. Shehada, M. dos Santos Dias, F. S. M. Guimarães, M. Abusaa, and S. Lounis, npj Computational Materials **7**, 87 (2021), arXiv:2012.11639 .

[56] P. Gambardella, S. Rusponi, M. Veronese, S. S. Dhesi, C. Grazioli, A. Dallmeyer, I. Cabria, R. Zeller, P. H. Dederichs, K. Kern, C. Carbone, and H. Brune, Science **300**, 1130 (2003).

[57] C. Chappert, A. Fert, and F. N. Van Dau, Nature Materials **6**, 813 (2007).

[58] D. Gatteschi and R. Sessoli, Angewandte Chemie - International Edition **42**, 268 (2003).

[59] D. Gatteschi, R. Sessoli, and J. Villain, *Molecular Nanomagnets* (Oxford University Press, New York, 2006) arXiv:arXiv:1011.1669v3 .

[60] V. Madhavan, W. Chen, T. Jamneala, M. F. Crommie, and N. S. Wingreen, Science **280**, 567 (1998).

[61] F. Delgado, C. F. Hirjibehedin, and J. Fernández-Rossier, Surface Science **630**, 337 (2014), arXiv:1401.7272 .

[62] F. Donati, S. Rusponi, S. Stepanow, L. Persichetti, A. Singha, D. M. Juraschek, C. Wäckerlin, R. Baltic, M. Pivetta, K. Diller, C. Nistor, J. Dreiser, K. Kummer, E. Velez-Fort, N. A. Spaldin, H. Brune, and P. Gambardella, Physical Review Letters **124**, 077204 (2020).

[63] A. B. Migdal, J. Exptl. Theoret. Phys. (U.S.S.R.) **34**, 1438 (1958).

[64] S. Engelsberg and J. R. Schrieffer, Physical Review **131**, 993 (1963).

[65] L. Hedin and S. Lundqvist, in *Solid State Physics*, Vol. 23, edited by F. Seitz, D. Turnbull, and H. Ehrenreich (Academic Press, 1970) pp. 1–181.

[66] M. S. Rogalski and S. B. Palmer, *Solid State Physics* (Harcourt College Publishers, New York, 2014) pp. 1–467.

[67] G. Grimvall, *The Electron-Phonon Interaction in Metals* (North Holland Publishing Company, Amsterdam, New York, Oxford, 1981).

[68] G. D. Mahan, *Many-Particle Physics*, 3rd ed. (Springer New York, NY, 2000).

[69] F. Giustino, Reviews of Modern Physics **89**, 015003 (2017).

[70] A. Lunghi, F. Totti, R. Sessoli, and S. Sanvito, Nature Communications **8**, 14620 (2017).

[71] A. Lunghi, F. Totti, S. Sanvito, and R. Sessoli, Chemical Science **8**, 6051 (2017).

[72] L. Escalera-Moreno, N. Suaud, A. Gaita-Ariño, and E. Coronado, Journal of Physical Chemistry Letters **8**, 1695 (2017).

[73] L. Escalera-Moreno, J. J. Baldoví, A. Gaita-Ariño, and E. Coronado, Chemical Science **9**, 3265 (2018).

[74] A. Albino, S. Benci, L. Tesi, M. Atzori, R. Torre, S. Sanvito, R. Sessoli, and A. Lunghi, Inorganic Chemistry **58**, 10260 (2019), arXiv:1904.04922 .

[75] A. Lunghi and S. Sanvito, Science Advances **5**, eaax7163 (2019).

[76] A. Lunghi and S. Sanvito, Journal of Chemical Physics **153**, 174113 (2020), arXiv:2005.12429 .

[77] M. Briganti, F. Santanni, L. Tesi, F. Totti, R. Sessoli, and A. Lunghi, Journal of the American Chemical Society **143**, 13633 (2021), arXiv:2105.06953 .

[78] P. Hohenberg and W. Kohn, Physical Review **136**, B864 (1964).

[79] W. Kohn and L. J. Sham, Physical Review **140**, A1133 (1965).

[80] R. M. Martin, *Electronic Structure: Basic Theory and Practical Methods* (Cambridge University Press, 2004).

[81] J. Kohanoff, *Electronic Structure Calculations for Solids and Molecules: Theory and Computational Methods*, Vol. 9780521815 (Cambridge University Press, Cambridge, 2006) pp. 1–348.

[82] O. Eriksson, B. Johansson, R. C. Albers, A. M. Boring, and M. S. S. Brooks, Physical Review B **42**, 2707 (1990).

[83] D. I. Khomskii, *Transition Metal Compounds* (Cambridge University Press, 2014).

[84] R. Rejali, D. Coffey, J. Gobeil, J. W. González, F. Delgado, and A. F. Otte, npj Quantum Materials **5**, 60 (2020), arXiv:1910.00325 .

[85] A. Ferrón, F. Delgado, and J. Fernández-Rossier, New Journal of Physics **17**, 033020 (2015), arXiv:1412.7956 .

[86] S. Baumann, *Investigation of the unusual magnetic properties of Fe and Co on MgO with high spatial , energy and temporal resolution*, Ph.D. thesis, University of Basel (2015).

[87] H.-P. Breuer and F. Petruccione, *The Theory of Open Quantum Systems* (Oxford University Press, 2007).

[88] S. Baumann, F. Donati, S. Stepanow, S. Rusponi, W. Paul, S. Gangopadhyay, I. G. Rau, G. E. Pacchioni, L. Gragnaniello, M. Pivetta, J. Dreiser, C. Piamonteze, C. P. Lutz, R. M. Macfarlane, B. A. Jones, P. Gambardella, A. J. Heinrich, and H. Brune, Physical Review Letters **115**, 237202 (2015).

[89] A. Oswald, R. Zeller, and P. H. Dederichs, Physical Review Letters **56**, 1419 (1986).

[90] K. Wildberger, V. S. Stepanyuk, P. Lang, R. Zeller, and P. H. Dederichs, Physical Review Letters **75**, 509 (1995).

[91] G. E. Pacchioni, L. Gragnaniello, F. Donati, M. Pivetta, G. Autès, O. V. Yazyev, S. Rusponi, and H. Brune, Physical Review B **91**, 235426 (2015).

[92] F. Von Oppen and K. J. Franke, Physical Review B **103**, 205424 (2021), arXiv:2105.06651 .

[93] J. Fabian and S. Das Sarma, Physical Review Letters **83**, 1211 (1999).

[94] J. M. Soler, E. Artacho, J. D. Gale, A. García, J. Junquera, P. Ordejón, and D. Sánchez-Portal, Journal of Physics: Condensed Matter **14**, 2745 (2002).

[95] W. E. Pickett, Computer Physics Reports **9**, 115 (1989).

[96] L. Kleinman and D. M. Bylander, Physical Review Letters **48**, 1425 (1982).

[97] D. R. Hamann, M. Schlüter, and C. Chiang, Physical Review Letters **43**, 1494 (1979).

[98] J. P. Perdew, K. Burke, and M. Ernzerhof, Physical Review Letters **77**, 3865 (1996).

[99] H. J. Monkhorst and J. D. Pack, Physical Review B **13**, 5188 (1976).

[100] P. Garcia-Goiricelaya, I. G. Gurtubay, and A. Eiguren, Physical Review B **97**, 201405(R) (2018).

[101] P. Garcia-Goiricelaya, J. Lafuente-Bartolome, I. G. Gurtubay, and A. Eiguren, Communications Physics **2**, 81 (2019), arXiv:1905.05168 .

[102] D. M. Kolb, W. Boeck, K.-M. Ho, and S. H. Liu, Physical Review Letters **47**, 1921 (1981).

[103] B. Reihl, K. H. Frank, and R. R. Schlittler, Physical Review B **30**, 7328 (1984).

[104] W. Altmann, V. Dose, and A. Goldmann, Zeitschrift für Physik B Condensed Matter **65**, 171 (1986).

[105] B. Reihl and J. M. Nicholls, Zeitschrift für Physik B Condensed Matter **67**, 221 (1987).

[106] H. Erschbaumer, A. J. Freeman, C. L. Fu, and R. Podloucky, Surface Science **243**, 317 (1991).

[107] L. Savio, L. Vattuone, M. Rocca, V. De Renzi, S. Gardonio, C. Mariani, U. Del Pennino, G. Cipriani, A. Dal Corso, and S. Baroni, Surface Science **486**, 65 (2001).

[108] R. Heid and K. P. Bohnen, Physics Reports **387**, 151 (2003).

[109] I. Y. Sklyadneva, R. Heid, P. M. Echenique, K. B. Bohnen, and E. V. Chulkov, Physical Review B - Condensed Matter and Materials Physics **85**, 155115 (2012).

[110] P. Hofmann, I. Y. Sklyadneva, E. D. Rienks, and E. V. Chulkov, New Journal of Physics **11**, 125005 (2009).

[111] R. Cuadrado and J. I. Cerdá, Journal of Physics Condensed Matter **24**, 086005 (2012).

Acknowledgments

I would not like to end this work without giving the place they deserve to the people who made it possible. I still remember perfectly the day I received an e-mail from Asier and Idoia proposing to do a PhD with them, and, looking back, I remember many other great moments that I will always keep with me from this journey. Moments that I owe to the people around me.

First of all, I would like to thank my supervisors Asier and Julen. Thanks to Asier for his many crazy scientific ideas, which sometimes end in a bunch of handwritten notes, but I can say that without them, finishing this thesis would not be possible. Thanks a lot also to Julen, who, despite being his first PhD thesis, has shown the great supervisor he is, always bringing a practical point of view to address problems. And of course, many thanks to Idoia, because, although in the end you have not officially been my supervisor, for me you have always been my third supervisor.

Regarding to my scientific family, I have to say that it has been a pleasure to be part of the "Computational theory in Condensed Matter Physics" group. Of the whole group I would like to especially mention Jon and Peio for the time spent in the office and for all their support in the early days of my PhD. I also want to wish the best to the young scientists of the group, Aitor and Malen.

For making lunchtime the best hour of the day, Gose Naiz Taldea (GNT) deserves a special place: Joanes, Asier, Iraultza, Iagoba, Julen, Iñigo, Mattin, Peio, Jon, Xabi, Telmo and Oscar. Thank you for all those great moments, and the ones that are yet to come.

I would also like to acknowledge the people of the Physics department at UPV/EHU, specially all my PhD colleagues, who all have made the office a most pleasant workplace: Peio, Jon Lafuente, Xabi, Jon Lopez, Aitor

Calvo, Oscar, Malen, Jon Gabilondo, Mireia, Jon Otegi, Aitor Erkoreka, Telmo, Santos, Iñigo, Paul and Leire.

Outside Leioa, I would like to thank Samir for kindly welcoming me in Jülich and Manuel for all his knowledge that has shared with me. I sincerely believe that without the boost you have given me this past year, this thesis would not be possible.

Apart from UPV/EHU, I would like to acknowledge the Donostia International Physics Center (DIPC) for financial support at the initial and final stages of my PhD, and for the computational resources.

Finally, I would like to acknowledge my closest and most important ones. To my parents, who proudly tell the strange things that their son does, thanks for all your unquestionable support. And Aroa, because you are always able to make me forget problems, even on the most difficult days, without you next to me I wouldn't be able to finish this thesis. Thanks for all the moments spent together.